Title

Device Engineering and Bioinstrumentation for Chemical Analysis of Human Exhaled Breath Condensate

Author

Schmidt, Alexander James

Publication Date

2022

Peer reviewed|Thesis/dissertation

Device Engineering and Bioinstrumentation for Chemical Analysis of Human Exhaled Breath Condensate

By

ALEXANDER J. SCHMIDT
DISSERTATION

Submitted in partial satisfaction of the requirements for the degree of

DOCTOR OF PHILOSOPHY

in

Mechanical and Aerospace Engineering

in the

OFFICE OF GRADUATE STUDIES

of the

UNIVERSITY OF CALIFORNIA

DAVIS

Approved:

Cristina E. Davis, Chair

Nicholas J. Kenyon

Erkin Şeker

Committee in Charge

2022

Device Engineering and Bioinstrumentation for Chemical Analysis of Human Exhaled Breath Condensate

Abstract

Portable methods for measurement and quantification of biological analytes have tremendous promise to advance non-invasive personal health monitoring devices. Exhaled breath metabolomics shares this promise and has been gaining popularity as a non-invasive technique amenable to a vast range of medical uses. Novel sampling technologies, rapid portable breath chemical analysis platforms, and miniaturized manufacturing methods have the potential to be scaled up for wide use in basic medical practice. This work presents design and implementation for collection and chemical analysis of human exhaled breath condensate. Exhaled breath condensate (EBC) samples were collected with a novel miniaturized sampler. Breath metabolite abundances were compared in healthy control subjects and asthmatic subjects. This work also investigates the relationship between breath aerosol size and EBC metabolomic content. Additionally, this work contributes to the fundamental performance of electrospray with a microfluidic chip, a technique used for liquid biochemical detection in analytical chemistry.

Acknowledgments

I deeply appreciate and acknowledge the love, care, and support I received from the people in my life. This dissertation would not have been completed without them.

I would like to thank my advisor, Dr. Cristina Davis for guiding me through the challenges of graduate school and for helping me become a better decision-maker. Thank you for providing me with the numerous opportunities to become successful academically. Your leniency, understanding, and sympathy during personal and obstructive life situations have meant so much to me. Your leadership, courage, and care during a global pandemic will always be something I am grateful for.

To my mentors, thank you for your guidance and support. I am grateful for Dr. Nicholas Kenyon for the valuable advice I have received throughout the years. Your dedicated feedback and support towards my grant applications, IRB paperwork, publications, and projects were deeply impactful. Thank you, Dr. Erkin Şeker, for meeting with me impromptu when I visited UC Davis as a prospective PhD student. Your classes at UC Davis have provided me with helpful knowledge to carry out my research and I appreciate the feedback you gave for my qualifying examination. Thank you, Dr. Tom Turpen, for the technical conversations and collaboration we had for my projects. I am thankful for Dr. Valeria La Saponara for her uplifting encouragement during my preliminary and qualifying examinations.

I thank the current and former members of the Bioinstrumentation and BioMEMS Laboratory at UC Davis, who all contributed towards an extraordinary working environment filled with talent and intellect. I am especially grateful for Dr. Konstantin Zamuruyev. Without your unwavering work ethic, attentiveness, care, and support, my work and research progress would not have been possible. Thank you, Dr. Eva Borras, Bradley Chew, Dr. Alexander Fung, Stephanie Fung, Patrick Gibson, Katherine Hamera, Michael LeVasseur, Mitchell McCartney, Dr. Maneeshin

(Yasas) Rajapakse, Leslie Simms, Cai Thompson, and Nhi Trinh for all of the laughs, shared stories, friendships, contributions, support, understanding, patience, and technical feedback.

I would like to thank Dr. Sumita Pennathur for her inspiration, motivation, and encouragement for me to pursue a PhD. Thank you for graciously providing me the opportunities and mentorship to learn and hone my engineering skills while attending your classes and working in your laboratory at UC Santa Barbara. Thank you, Dr. David Bothman, for your advice and guidance that helped me prepare for graduate school. Dr. Dino Di Carlo, I appreciate the opportunities and understanding you provided me while working in your laboratory at UC Los Angeles, which helped me prepare for graduate school. Thank you, Seth Boden, and Dr. Ming Li, for your guidance, supervision, and expertise that helped me succeed later in graduate school.

I deeply appreciate my martial arts instructors, Louman Cheung and Pedro Silva for teaching me the dedication, trust, discipline, and awareness I needed to enhance all aspects of my life. Thank you, Gianluca Bacci, Julie He, Constante Limcolioc, and Ceili (Kitty) Wasson for your friendship and martial arts training sessions with me. It is a great pleasure to know all of you.

I would like to thank my friends, Mike Carri, Summeke (Sum) Chan, Jessica (Jess) Dill, Joe Graff, Dana Iltis, Riley Kibbee, Taeyoung (Tammy) Kim-Lee, Leslie Leung, Dr. Chris Nilsen, Dr. Mike Reitman, Dr. Lindsay Rondot, Dr. Ramuel Safarkoolan, Megan Shyr, Roy (RJ) Taggueg, Kathleen Tang, Zach Trowbridge, Michael Walters, and Sara Willman. Thank you all for your friendship, laughs, stories, support, generosity, and kindness. You all helped me to learn and grow into an augmented version of myself. I will always appreciate the connections I have made with you and your abilities to uplift me during challenging periods of graduate school. You are wonderful people and I wish for the very best in life for you.

With all my heart, I thank my family. I deeply thank my sister, Eva Dayananthan, for her love, care, and support. You are a brilliant light of my life. Your understanding, patience,

determination, and acceptance has been a bedrock to my wellbeing and upbringing. I could not have gone this far without you. I love you, sis. I thank my brother-in-law, Dr. Ashok (Josh) Dayananthan. Thank you for your consistent support, understanding, and acceptance over so many years of my life. I thank my nieces, Annabelle Dayananthan, Eleanor Dayananthan, and Audrey Dayananthan. You each bring so much joy into my life and I learn so much from each of you. Thank you for making me feel like a kid again. I thank my uncle, Ed Leo, for the support, advice, generosity, and understanding you have given me. I thank my cousins, Sammie Leo, and David Leo for your kindness and understanding. I am proud of both of you. I thank my father, Douglas Schmidt, for inspirations to become an engineer and for teaching me computer software and hardware skills at an early age. I thank Karla and Tim McCann for their acceptance, advice, and support. In loving memory, I thank my grandfather, Joseph (Joe) Leo, for creating a strong and stable foundation for our family. In loving memory, I thank my grandmother, Annabelle Leo. Thank you so much for your care, upbringing, guidance, and wisdom. In loving memory, I thank my mother, Joanne Schmidt. Your unconditional love, patience, guidance, care, understanding, and support has allowed me to flourish, to be successful, and to be happy. The moral compass you have instilled in me is the most valuable tool I have to develop my character. You understood me better than anyone else ever could or ever will. I will learn to live with the love you left behind. I wish that you were here and able to witness the completion of my PhD. I love you all so much.

Partial financial support was provided by NIH awards: U01 EB0220003-01 (CED, NJK); National Center for Advancing Translational Sciences (NCATS) through grant UL1 TR000002 (CED, NJK); UL1 TR001860 (CED, NJK); 1P30ES023513-01A1 (CED, NJK); UG3-OD023365 (CED); 1U18TR003795-01 (CED, NJK), 4U18TR003795-02 (CED, NJK); and 1U01TR004083-01 (CED, NJK). Student support was provided by the National Center for Advancing Translational Sciences, National Institutes of Health, through grant number UL1 TR001860 and linked award TL1 TR001861. Partial support was also provided by the Department of Veterans

Affairs award I01 BX004965-01A1 (CED, NJK); the University of California Tobacco-Related Disease Research Program award T31IR1614 (CED, NJK); and University of California CITRIS and the Banatao Institute award 19-0092 (CED, NJK). Trainee support was provided by NIH TL1 TR001861 (AJS) and T32 HL07013 (KOZ). The contents of this dissertation are solely the responsibility of all contributing authors and do not necessarily represent the official views of the funding agencies. I gratefully acknowledge access and use of the Food Safety and Measurement Facility in the Department of Viticulture and Enology at UCD for sample analysis. I gratefully acknowledge access and use of the UC Davis Center for Nano and Micro Manufacturing (CNM2). I gratefully acknowledge Dr. Konstantin Zamuruyev, Mitchell McCartney, Patrick Gibson, Bradley Chew, and Dr. Jean-Pierre Delplanque (University of California, Davis) for technical discussions. I also thank Carolyn Doyle for lyophilization of EBC samples. I am grateful for all the participating children and their families who devoted their time and samples for the sake of conducting the research.

Table of Contents

List of Figures

List of Tables

Chapter 1: Introduction

Introduction

Portable methods for measurement and quantification of biological analytes have tremendous promise to advance non-invasive personal health monitoring devices. Exhaled breath metabolomics shares this promise and has been gaining popularity as a non-invasive technique amenable to a vast range of medical uses. Novel sampling technologies, rapid portable breath chemical analysis platforms, and miniaturized manufacturing methods have the potential to be scaled up for wide use in basic medical practice.

Exhaled breath is a complex mixture containing basic respiratory gases, hundreds of volatile organic compounds (VOCs) of exogenous and endogenous origin, and aerosolized droplets of non-volatile compounds from the liquid lining of the lung. Depending on the sampling method, there are two fractions of breath: exhaled breath vapor (EBV) and exhaled breath condensate (EBC). EBV mainly contains the gaseous fraction of the breath with VOCs. EBC is obtained when the exhaled breath is cooled and converted into a liquid phase comprising soluble exhaled gases and non-volatile metabolites of the extracellular lining fluid.[1]

In Chapter 2, a proof-of-principle pilot study describes altered metabolites in a small cohort of healthy control subjects and mild asthmatic subjects. For this, breath samples were collected as condensates with a novel miniaturized sampler. The EBC obtained was analyzed with liquid chromatography-mass spectrometry (LC-MS) to discriminate asthma phenotypes or even define specific metabolite differences between subjects. This work compares breath metabolite abundances in six healthy control subjects and five asthmatic subjects. Exhaled breath condensate (EBC) samples were collected with a novel miniaturized sampler. This device enables breath sample collection in multiple environments, including intensive care units, outpatient clinics, workplaces, and at home. A total of 293 breath samples were collected and analyzed longitudinally, including about 28 samples per subject. EBC was analyzed with liquid chromatography-mass spectrometry (LC-MS) to define specific metabolite differences between

subjects. Untargeted and targeted metabolomic analyses were performed simultaneously, but with separate data analysis procedures.

The pilot study described in Chapter 3 uses a previously described hand-held human breath sampler device with varying notch filter geometries to redirect the trajectory of breath aerosols based on size.[2] Curved flow profiles have greater inertial effects on larger breath aerosols which cause them to strike the interior walls before they can arrive at a collection site. In this present work, we investigate metabolite content of various aerosol fractions. The non-volatile fraction of breath condensate was analyzed with high performance liquid chromatography mass spectrometry (LC-MS) for broad metabolite coverage.[3] Additionally, the trajectories of these aerosols were simulated with varying notch filter lengths using COMSOL Multiphysics® software. It is hypothesized that: (1) increasing the length of the notch filter in this device will prevent larger aerosols from reaching the collection tube thus altering the breath aerosol size distribution sampled in EBC; and (2) there is not a systematic large-scale difference in EBC metabolomic content that correlates with breath aerosol size.

Chapter 4 presents the microfabrication and performance of a novel three-dimensional electrospray ionization (ESI) emitter tip made from glass. Electrospray Ionization (ESI) is a prevalent technique for liquid chemical detection in analytical chemistry.[4] ESI generates a fine liquid aerosol through electrostatic charging. A high electric potential (typically ± 2–5 kV) is applied between the end of a capillary and a counter electrode installed in proximity (typically 1–2 mm). Tiny micro–droplets tear away from the surface of a liquid Taylor cone searching for a surface to land. These ions land on a counter electrode plate which can then be detected amperometrically. Our fabrication method involves the novel application of two layers of positive and negative photoresists in addition to Parafilm® wax tape. We also use isotropic wet etching of glass in hydrofluoric acid (HF) solution and chromium (Cr) deposition. This approach creates a three-dimensional ESI tip with accurate and high quality small-scaled geometric features. This allows for higher charge densities leading to increased ionization efficiency for better signal

stability and repeatability. Open edge and tiered depth details were successfully created from a multilayer planar mask. This is a benefit for integrated microfluidic systems that often require micro features for their functionality but large millimeter size features for their physical periphery. The fundamental performance of electrospray was demonstrated with our glass microfluidic chip. The electrospray signal was measured in response to varying the distance between the electrospray emitter tip and a metal counter electrode plate in addition to the varying concentration of a background electrolyte.

Chapter 2: Portable exhaled breath condensate metabolomics for daily monitoring of adolescent asthma

Alexander J. Schmidt, Eva Borras, Anh P. Nguyen, Danny Yeap, Nicholas J. Kenyon, Cristina E. Davis

Journal of Breath Research (2020) 14: 026001
DOI: 10.1088/1752-7163/ab35b5

Authorship Contributions

Alexander J. Schmidt: Conceptualization, device design and testing, clinical study design and analysis, clinical study participant recruitment, experiment planning, experimental data, review of data and results, writing original draft, writing review, and editing. **Eva Borras:** Conceptualization, clinical study design and analysis, experiment planning, experimental data, review of data and results, writing review, and editing. **Anh P. Nguyen:** Clinical study participant recruitment, experimental data, review of data and results, and editing. **Danny Yeap:** experimental data, review of data and results. **Nicholas J. Kenyon:** Conceptualization, funding, mentoring, supervision, writing review and editing. **Cristina E. Davis:** Conceptualization, experiment planning, review of data and results, funding, mentoring, supervision, writing original draft, writing review and editing.

Definitions of Abbreviations

8-OH-2dG, 8-Oxo-2'-deoxyguanosine; a.u., arbitrary units; avg., average; COX, cyclooxygenase; DiHOME, dihydroxy octadecenoic acid; emergency department, ED; EIC, Extracted Ion Chromatogram; EpOME, epoxy octadecenoic acid; HETE, hydroxyl eicosatetraenoic acid; HHTre, heptadecatrienoic acid; HODE, hydroxyoctadecadienoic acid; LX, lipoxin; LOX, lypooxygenase; LT, leukotriene; oxoODE, oxo octadecadienoic acid; P450, cytrochrome P450 (CYPs); PC, principal component; PCA, principal component analysis; PG, prostaglandin; PLS-DA, partial least squares discriminant analysis; qTOF, quadrupole time of flight; S, subject; std, standard deviation; TX, thromboxane.

Abstract

Portable methods for measurement and quantification of biological analytes have tremendous promise to advance non-invasive personal health monitoring. Exhaled breath metabolomics shares this promise and has been gaining popularity as a non-invasive technique amenable to a vast range of medical uses.

This work compares breath metabolite abundances in six healthy control subjects and five asthmatic subjects. Exhaled breath condensate (EBC) samples were collected with a novel miniaturized sampler. This device enables breath sample collection in multiple environments, including intensive care units, outpatient clinics, workplaces, and at home. A total of 293 breath samples were collected and analyzed longitudinally, including about 28 samples per subject. EBC was analyzed with liquid chromatography-mass spectrometry (LC-MS) to define specific metabolite differences between subjects. Untargeted and targeted metabolomic analyses were performed simultaneously, but with separate data analysis procedures.

Individual differences among subjects were found longitudinally. When presented by health condition, group differences were enhanced with a clear separation between subjects belonging to either the control or asthmatic group. Unexpectedly, targeted compounds consistently had lower intensities in asthmatics. There is a distinct pattern of a day/night cycle with elevations of peak area values in evening samples. These differences were presented mainly in asthmatic subjects, which can be explained by asthma being a representation of exaggerated amplitudes compared to healthy circadian patterns.

Untargeted and targeted analysis of EBC using this device allows the discovery of novel endogenous metabolic signals in a biological sample and the daily monitoring of selected metabolites related to diseases and medical conditions.

Introduction

Portable methods for measurement and quantification of biological analytes have tremendous promise to advance non-invasive personal health monitoring devices. Exhaled breath

metabolomics shares this promise and has been gaining popularity as a non-invasive technique amenable to a vast range of medical uses. Novel sampling technologies, rapid portable breath chemical analysis platforms, and miniaturized manufacturing methods have the potential to be scaled up for wide use in basic medical practice.

Exhaled breath is a complex mixture containing basic respiratory gases, hundreds of volatile organic compounds (VOCs) of exogenous and endogenous origin, and aerosolized droplets of non-volatile compounds from the liquid lining of the lung. Depending on the sampling method, there are two fractions of breath: exhaled breath vapor (EBV) and exhaled breath condensate (EBC). EBV mainly contains the gaseous fraction of the breath with VOCs. EBC is obtained when the exhaled breath is cooled and converted into a liquid phase comprising soluble exhaled gases and non-volatile metabolites of the extracellular lining fluid.[1] EBC is considered a simplified metabolite signature that only contains water soluble volatiles and non-volatile compounds.[5] EBC can be a valuable matrix for biomarker discovery, providing vital information about lung health.

EBC has been used to diagnose diseases, to monitor status of medical conditions using physiologic markers, and to identify presence of exogenous compounds that could be etiologic or exacerbating factors in specific diseases.[6,7] Several publications have reported the application of EBC sampling as a quick screening tool for respiratory conditions focused on inflammatory markers. EBC is considered a filtrate of blood, reflects the lung epithelia,[1] and has been used for diseases such as asthma,[8] chronic obstructive pulmonary disease (COPD),[9] pneumonia,[10] or cystic fibrosis.[11] EBC collection devices can be used in several locations, including intensive care units (ICUs), outpatient clinics, workplaces, and at home.

This current study conducts a simultaneous targeted and untargeted analysis of inflammatory and oxidative stress markers reported in studies of asthma.[12–15] Common inflammatory markers are formed by the lipid oxidation (oxylipins), mainly involving eicosanoids that are metabolites of arachidonic acid (C20:4n6). We analyze a balance between pro- and

anti-inflammatory oxylipins commonly examined in EBC. A pro-inflammatory profile has been shown in patients with a pathophysiology of bronchial obstruction,[16] that presented higher concentrations in EBC of leukotrienes (LTB4) and cysteinyl-leukotrienes (LTC4, LTD4, LTE4),[17–20] and thromboxanes (TXA2, TXB2 and 11-dehydro-TXB2).[21,22] Anti-inflammatory activity can be promoted in numerous diseases like asthma[23] by the presence in the airways of hydroxyeicosatetraenoic acid (5-, 12- and 15-HETE), its derivatives such as lipoxin A4 (LXA4),[22,24] and resolvin E1 (RvE1),[25] an EPA metabolite.

The oxidative stress markers can be linked to DNA damage, lipid peroxidation, redox enzyme activity and decreased antioxidant defense levels.[26] Some studies have determined in EBC that 8-hydroxy-2'-deoxyguanosine (8-OHdG) is generated by DNA degradation,[27] prostaglandins (PGD2, PGE2, PGF2 and 8-iso-PGF2) are induced by lipid peroxidation,[19,28] and o-tyrosine modifies proteins.[29] These metabolites will serve as our targeted measure of inflammatory responses and oxidative stress markers. However, there are two main challenges in detecting these specific compounds using a single methodology. One problem is the low concentrations presented in EBC, which makes the detection of some of the compounds very difficult, and another issue is the difference in chemical structures of these compounds, which usually require specific sample treatments.

In order to overcome these limitations, parallel-untargeted metabolite analysis can offer a more general measure of the biological status in health, and has the potential to discover novel biomarkers, which can also be up- or down-regulated in diseased cells. Untargeted analysis allows a better comprehension of the specific breath compounds related to certain conditions, offering additional information that cannot be considered in an initial hypothesis. Additionally, untargeted analysis allows putative identification of potential metabolites related to both exogenous factors of potential etiologic interest and endogenous chemicals of possible mechanistic significance.

In this proof-of-principle pilot study, we describe the altered metabolites in a small cohort of healthy control subjects and mild asthmatic subjects. For this, breath samples were collected as condensates with a novel miniaturized sampler. The EBC obtained was analyzed with liquid chromatography-mass spectrometry (LC-MS) to discriminate asthma phenotypes or even define specific metabolite differences between subjects.

Materials and Methods

Human Subject Pilot Study

This research adhered to clinical practices and protocols as approved by the University of California, Davis Institutional Review Board (IRB Protocol #1055441). Informed consent was obtained from all subjects or their parents when subjects were under 18 years of age. Twelve adolescents were recruited in total, including subjects who had physician diagnosed and treated asthma and healthy control subjects with no history of lung disease. The age range from all subjects was between 14 and 18 years of age, and all EBC samples were collected longitudinally by the subjects in their homes. All subjects followed the same protocol and instructions for breath collection.

Briefly, all subjects underwent a training visit, in which they were instructed on the use of the handheld EBC collector. All subjects completed an intake questionnaire about their overall health, symptoms including fatigue, shortness of breath, weekly physical activities, medication use, as well as healthcare utilization including clinics and emergency department (ED) visits in the last 6 months. They were instructed to complete a daily diary about respiratory symptoms, medication use, time of collection, humidity, temperature, and any comments about ease of use.

Exhaled Breath Condensate Collection

Breath sample collection is achieved using a condenser surface in a miniature breath collector that has been previously published.[30] Briefly, the condenser surface is installed in a flow chamber and cooled with a thermoelectric element. The vapor in exhaled breath is condensed

on the cooled surface as it passes. The conversion of exhaled breath to liquid phase facilitates sample manipulation and chemical analysis when metabolite concentrations are very low. The EBC sampler has a disposable mouthpiece, a set of inhale and exhale one-way flap valves to allow condensation of exhaled breath only, and a saliva filter.[2] The sampling time is 15-20 minutes, and the miniature EBC sampler collects between 200-500 µL of EBC during normal tidal breathing. EBC samples were stored at -15 °C in personal household freezers, until they were returned to the lab for analysis. Subjects collected breath samples twice per day, (morning and night, approximately 8 AM / 8 PM) for 2 weeks. No nose clip was worn during collection. Subjects performed normal tidal breathing. In order to reduce the effect of food related confounders, the subjects restrained from food consumption or brushing their teeth one hour before the EBC collection procedure and rinsed their mouth with water prior to sampling.

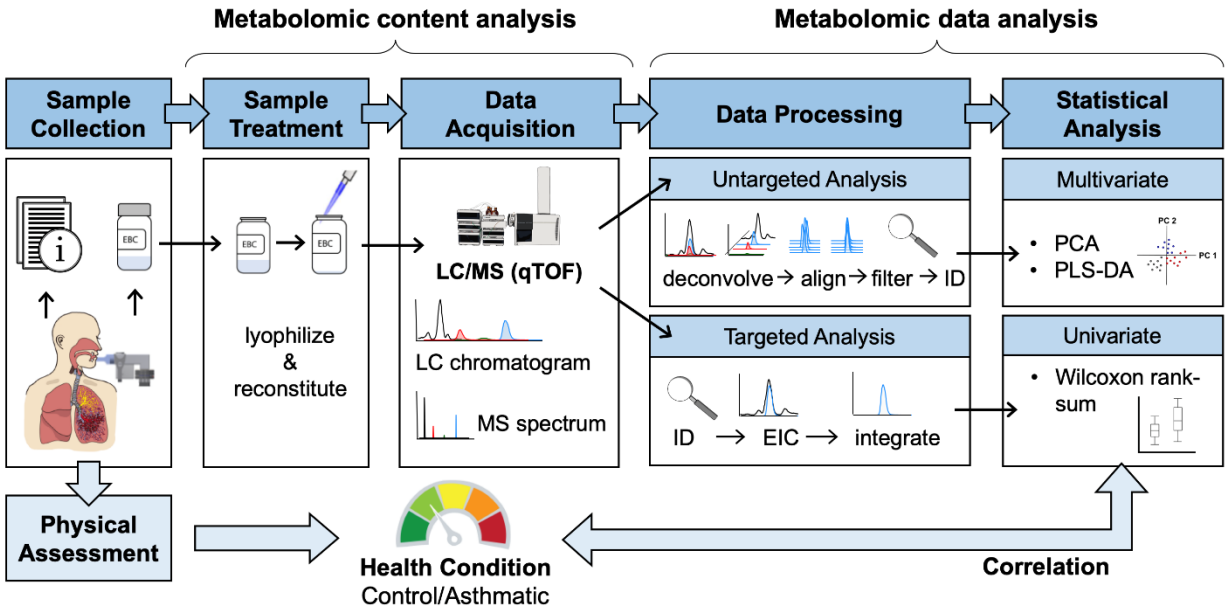

Figure 1. Metabolomics workflow for the human breath study.

Prior to subject enrollment, the surfaces were immersed in a 'Piranha' bath (4:1, H_2O_2 (30%):H_2SO_4 (98%)) for one hour to clean the surface. The surfaces were thoroughly rinsed with deionized (DI) water, dried with nitrogen gas, and stored in a clean environment. The miniature EBC sampling device was reused by each subject. All parts of the device, including

the glass pipettes, were thoroughly cleaned once per day by subjects. The cleaning protocol included: 70% ethanol disinfectant spray followed by a deionized (DI) water spray and air-dried. After breathing into the device, subjects collected the EBC sample into a clean borosilicate glass vial with a reusable glass pipette. The 28 EBC samples obtained for each subject were kept frozen during transport and then stored in a laboratory freezer at -80 °C until analysis. The analytical procedure workflow followed in this study is shown (**Figure 1**).

Although the EBC sample volume is small, the sampling rate of this miniature EBC sampler is higher than commercial samplers, when compared by surface area of the condenser element.[2] We also note that EBC sampling for a shorter period would be more practical for portable self-diagnostic platforms. The time duration was required due to the size-scale mismatch between a miniature collection element and the large bench-top instruments used for chemical analysis of the collected EBC sample. The minimum sample volume for bench-top mass spectrometers exceeds that of microfluidic platforms. The amount of sample collection could be reduced to a few microliters and sampling time to a few minutes when collection and analysis are coupled with near-real-time detection micro-scaled systems.[31]

Sample Preparation

Frozen EBC (250 µL) was directly lyophilized inside the glass vials. The obtained dried extract was reconstituted using 25 µL of mobile phase (95% water in acetonitrile). Afterwards, samples were shortly vortexed, sonicated for 10 min at 4°C and centrifuged at 13,000 rpm for 10 min at 4 °C. The supernatant was transferred to a glass vial and stored at -80 °C until analysis. A pooled quality control (QC) sample was also prepared with each batch of samples by mixing healthy EBC and spiking it with a known concentration of eicosanoid standard mix. QCs, and non-spiked EBC samples (QC blank) were prepared following the sample preparation process for all samples. Blanks (mobile phase) were injected repeatedly during the analysis.

Instrumental Analysis

A simultaneous untargeted and targeted metabolomics analysis was performed on an Agilent 1290 series HPLC system coupled with an Agilent 6530 quadrupole-time of flight (qTOF) mass spectrometer (Agilent Technologies, Santa Clara, CA, USA). 20 μL of each sample was injected through an InfinityLab Poroshell 120 EC-C18 column (2.7 μm, 3.0 mm × 50 mm; Agilent Technologies, Palo Alto, CA, USA). The mobile phases consisted of water (A) and acetonitrile (B), both with 0.1% formic acid. The solvent flow rate was set to 0.6 ml min^{-1}, the column temperature to 35 °C and the autosampler to 5 °C to increase sample stability. An electrospray ionization (ESI) source with an Agilent Jet Stream nebulizer was used in negative mode with the following operating parameters: capillary voltage, 4000 V; nebulizer pressure, 25 psi; drying gas, 10 L min^{-1}; gas temperature, 250 °C; fragment voltage, 130 V. The qTOF calibration was performed daily with the manufacturer's solution. Mass measurements were recalibrated using the reference mass *m/z* 112.9856 (deprotonated trifluoroacetic acid (TFA)) in negative ion mode. Mass spectra were acquired at MS resolution level at a scan rate of 2 spectra/s in the over a range of *m/z* 100–950, and for MS/MS over at a scan rate of 5 spectra/s in the over a range of *m/z* 50–750. Collision energies for precursor ions were set within the range 5–20 eV, after a preliminary optimization by injecting eicosanoid standard mix. The targeted compounds detected by LC-MS/MS are reported in **Supplemental Table S1**. Molecular formula and exact masses are provided together with LC-MS retention times and preferred precursor ions used for AutoMS/MS analysis. Confirmation qualifier masses and optimal collision energies used are also listed.

Data Processing and Statistical Analysis

The metabolomic data analysis procedure workflow is shown in **Figure 1**. Untargeted and targeted information were acquired simultaneously in a single chemical analysis, but the treatment of the obtained data was performed separately. However, in both cases, LC-MS data

were initially checked for qualitative purposes with Agilent's Mass Hunter Qualitative Analysis B.06.00 software. For untargeted analysis, data mining was performed using an automated algorithm for peak finding, alignment and integration in Agilent's Mass Hunter Profinder B.08.00 software. Because of the huge amount of data, raw data was treated by batches using Bach Recursive Feature Extraction with the following parameters: mass tolerance and window of 20 ppm and 0.025 Da, retention time (RT) range 0.2–16.5 min and window of 0.3 min, with minimum absolute abundance of 1000 counts. The obtained dataset was exported into a *.cef* format and imported to Agilent's Mass Profiler Professional (MPP, V13.0) software for re-alignment, identification and initial statistical analysis. Same mass and retention time windows were set to compile all data into a single dataset. Afterwards, the identification of the obtained molecular features (markers), described as *mass@retention time*, was performed using ID browser, an integrated software in MPP. ID browser used the accurate mass information of the aligned spectra to calculate the proposed molecular formula and tentative compound name of each compound or marker. Based on matching experimental and theoretical isotope pattern of the markers, the software proposed formulas and names with scores above 70%. Compounds were identified by using the METLIN database. The dataset was filtered by removing compounds that appear in blank samples with signals higher than 10 (peak sample/blank ratio). Final data was normalized using probabilistic quotient normalization with median values per sample to correct the bias between sample collection and preparation.[32]

Due to the low amount of signal detected for the targeted analysis, quantification was not possible. For that, we worked with the intensity of the peak detected corresponding to the listed compounds in **Supplemental Table S1**. Data was treated with Agilent's Mass Hunter Quantitative (qTOF) Analysis B.07.00 software, where the peaks were compared and constrained into a MassHunter quantification method on the accurate mass precursor ion level, using the MS/MS information to confirm the compounds identification manually with adducts and

spectral scoring accuracy. The targeted dataset containing integrated peak area values was corrected by batch analysis using prepared QCs.

Datasets were analyzed using univariate and chemometric data compression techniques. Both analyses were performed with MATLAB R2017a and PLS Toolbox V8.6.2 software. Tables were constructed using Excel software (Microsoft, Redmond, WA, USA). These techniques identified similarities and differences between analyzed samples. Univariate statistical analysis was performed using a two-sided Wilcoxon rank sum test (MATLAB command ranksum), which is a non-parametric statistical method testing the null hypothesis that data from two sets are samples from continuous distributions with equal medians, against the alternative that they are not. The test assumes that two samples are independent. Having a p value less than 0.05 indicates the rejection of the null hypothesis of equal medians at the 5% significance level. For untargeted analysis, Principal Components Analysis (PCA) was applied as an unsupervised method that explores the intrinsic variation of the data detecting potential patterns. PCA simplifies the complexity of high-dimensional data by transforming the data into fewer dimensions with a "best-fitting" straight line or plane.[33] Partial Least-Squares Discriminant Analysis (PLS-DA), however, is a supervised classification technique that uses a response category and allows the filtering of the discriminant compounds or markers.[34] All techniques provided a list of potential markers related to the health condition and other relevant biological information of the study.

Results and Discussion

Demographic and Clinical Characteristics Data from Participants at Baseline

From February 2018 to December 2018, six asthmatic patients and six healthy participants from the northern Central Valley California region were recruited. A total of 293 breath samples were collected and analyzed longitudinally in the study, with about 28 samples for each of the 11 subjects. One hundred sixty samples were collected from the six control subjects and 133 from

five asthmatic subjects. Of these, samples from one asthmatic participant were excluded as contaminated. All samples from the subject who was excluded from the study contained a white solid powder that was only observed when the sample was lyophilized. This precipitate consisted of fibrin or mucous substances soluble with mobile phase, which clogged the LC system making the instrumental analysis not feasible. All control subjects were in good health and had no history of smoking. Health symptoms and medicinal use as reported by participants while collecting breath samples are represented in **Supplemental Figure S1**. Asthmatic subjects were 16.7 ± 1.3 years of age and healthy control subjects were 17.2 ± 1.5 years of age. For the control group there were three male and three female subjects, and for the asthmatic group three male and two female subjects. All asthmatic participants were prescribed daily inhaled corticosteroid. Mean prescribed inhaled corticosteroid dose range was 440 µg/day. Three of the five asthmatic participants were also on a leukotriene antagonist.

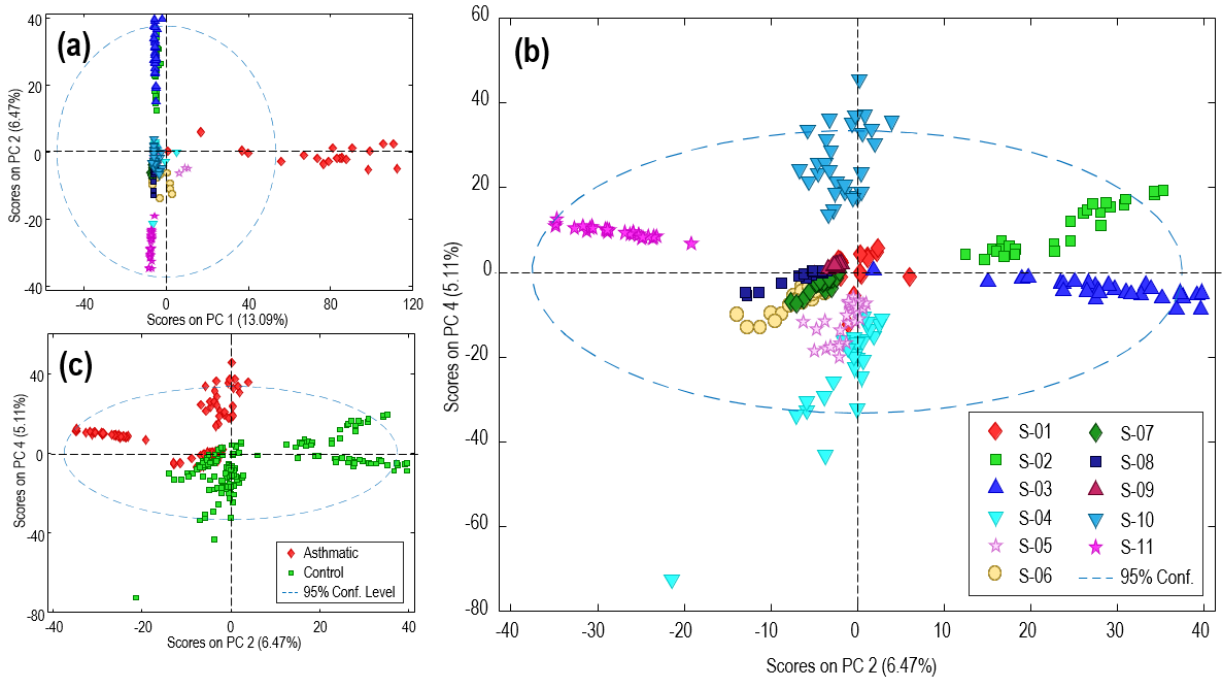

Figure 2. Scores plot from the Principal Components Analysis (PCA) obtained with untargeted LC-MS data. All samples were distributed in two-dimensional score plots represented by PC1 and PC2 (a), as well as PC2 and PC4 (b and c). Samples were colored by subject batches (a and c) and by health condition (b).

Untargeted Metabolomics Analysis

A total of 3,583 metabolite features were obtained from the LC-MS chromatograms in negative mode. Data was previously aligned and filtered, as described in section 2.5. The resulting data were autoscaled before building the multivariate models.

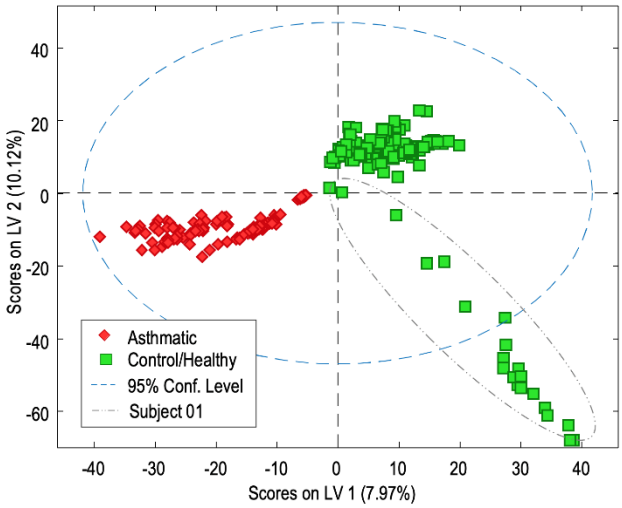

Figure 3. PLS-DA scores plot obtained with untargeted LC-MS data. Sample discrimination by health condition using 2 components (LV1 versus LV2). Control/healthy samples are colored in green and asthmatic samples are colored in red.

PCA was first established based on these features to discover the presence of inherent similarities in mass spectral profiles between groups of samples (**Figure 2**). Individual differences between subject batch of samples were studied (**Figure 2a and 2b**), as well as main differences between health conditions (**Figure 2c**), defined by control/healthy versus asthmatic. Although PCA shows low explained variance, the highest variability (13% in first principal component, PC1) is due to one of the subjects (S-01) front the rest of participants (**Figure 2a**). These results corresponded to the signal obtained by the Total Ion Chromatogram (TIC) from the samples (**Supplemental Figure S2**) and S-01 already presented higher LC-MS intensities on the TIC profile through all the samples. No parameters (ambient humidity, temperature, dryness of mouth, shortness of breath) from S-01 were significantly different from other subjects during time of sampling, except reports of high fatigue. S-01 was part of the control group and

these differences among other controls could be explained by either an unknown health condition, an incorrect sample collection procedure, or sample contamination during the experimental process.

When PC 2 and PC 4 were studied, even explaining only around 10% of the total variance, differences could be distinguished between most of the subjects (**Figure 2b**). That information can be used to define specific metabolites per subject by reaching the loadings or variables that describe those sample distributions in the PCA score plot. When the same data was presented by health conditions (**Figure 2c**); then, group differences were enhanced with a clear separation between subjects belonging to the control group and the ones belonging to asthmatic group.

Based on the preliminary PCA results, a PLS−DA model was constructed to discriminate the difference under the already established separation between health conditions. As shown in **Figure 3**, the subjects from the asthmatic and control groups were appreciably separated from each other using two latent variables (LV). The model was validated by applying cross-validation with random subsets, and a test validation using 66% of the samples randomly to build the PLS-DA model and the rest as external test samples. In both cases, all the samples were correctly classified by the health condition. The clear sample separation by PLS-DA score plots indicates which loadings define the model components. Loadings are described by the data variables or features, which include the potential asthmatic marker metabolites that distinguish the sample groups. For example (**Figure 3**), positive values for LV1 allow the identification of characteristic features for control/healthy subjects. In the same way, negative LV1 and LV2 describe specific features from subjects from the asthmatic group. Although LV loadings provide useful asthmatic- versus control-regulated features, Variable Importance for the Projection (VIP) score values are principally used to select potential features. The contribution of VIPs from the PLS-DA allows a reliable selection of differential metabolites when selecting VIP values that exceed 1.0. Based on these criteria the number of relevant variables

was reduced to 1338. From those, the 30 compounds with highest VIPs were selected and presented in **Table 1**.

Potential Metabolite Identification

Metabolite identification of untargeted data was performed based on the MS and MS/MS spectra and the accurate masses obtained using METLIN database. In **Table 1**, potential biomarkers are listed with their exact molecular mass and retention time. Molecular formula and compound identification are described together with their identification (ID) score, calculated with the average values from molecular formula extraction and database ID scores. PLS-DA values from VIP scores, LV1 and LV2 loadings are also presented. Those values allow the health condition regulation. Once the features were identified, we listed them as eicosanoid or compound related to inflammation process.

Six metabolites (bolded in **Table 1**) were identified as eicosanoid related, four of them specific from asthmatic subjects: 9-deoxy-9-methylene-16,16-dimethyl-prostaglandin E2, unoprostone isopropyl ester, 17,20-dimethyl prostaglandin F1a and 2,3-dinor-TXB1. All of them are prostaglandin related compounds, except the last one, which is a metabolite from thromboxane B2. Also, 8R,11S-DiHOME and 5S, 12S-DiHETE were identified as regulated by control group. The first one is formed by bacterial oxidation of oleic acid; and the latter, is an epimer of leukotriene B4. Although, no asthma pro- or -anti-inflammatory studies are related to these compounds, this pilot study is presenting preliminary data from potential metabolites that can be related to asthmatic conditions. Further studies can provide more information and confirmation of these promising results.

Table 1. The list of potential metabolites identified by untargeted liquid chromatography-mass spectrometry (LC-MS) analysis of all exhaled breath condensate samples.

Variable number	Mass	RT (min)	Formula	Compound Name	ID Scores	VIP Scores	LV 1 (7.97%)	LV 2 (10.12%)	Eicosanoid related	C/A regulated	Description
1	414.309	13.29	C23 H42 O6	Not identified	99.73	3.73	-0.04	-0.03	-	A	-
2	392.292	14.57	C24 H40 O4	7b,12a-Dihydroxycholanoic acid	79.67*	3.52	-0.04	-0.01	No	A	Steroids and steroid derivatives (bile acid)
3	322.211	10.03	C19 H30 O4	Clovanediol diacetate	83.58	3.48	-0.04	-0.01	No	A	Sesquiterpenoids
4	378.275	13.47	C23 H38 O4	**9-deoxy-9-methylene-16,16-dimethyl-PGE2**	80.69	3.34	-0.03	-0.04	Yes	A	Potent analog of prostaglandin E2
5	424.316	15.42	C25 H44 O5	**Unoprostone isopropyl ester**	78.69*	3.24	-0.04	-0.01	Yes	A	Prodrug form, free acid analog of PGF2α
6	442.331	14.86	C32 H42 O	(all-E)-6'-Apo-y-caroten-6'-al	73.81*	3.21	-0.04	-0.01	No	A	Triterpenoids
7	284.015	3.75	C21 H2 N O	Not identified	83.15	3.21	-0.04	-0.01	-	A	-
8	292.018	4.31	C14 H12 O3 S2	RITA	51.22*	3.15	-0.04	-0.01	No	A	Thiophenes (Sos Bismethanol)
9	384.287	11.94	C22 H40 O5	**17,20-dimethyl Prostaglandin F1a**	83.46	3.08	-0.04	-0.01	Yes	A	Prostaglandins and related
10	285.226	11.00	C15 H31 N3 S	Not identified	93.64	3.07	-0.04	-0.01	-	A	-
11	447.249	3.74	C20 H37 N3 O6 S	S-Decyl GSH	68.18*	3.04	-0.04	-0.02	No	A	Peptide
12	484.378	17.08	C27 H54 N3 S2	Not identified	92.15	3.02	-0.03	-0.01	-	A	-
13	314.246	15.66	C18 H34 O4	**8R,11S-DiHOME**	85.64	2.94	0.04	0.01	Yes	C	Bacterial oxidation product of oleic acid
14	456.346	15.77	C33 H44 O	Citranaxanthin	78.96*	2.93	-0.04	-0.01	No	A	Triterpenoids, carotenoid pigment
15	342.241	9.39	C19 H34 O5	**2,3-Dinor-TXB1**	84.92	2.89	-0.04	-0.01	Yes	A	Thromboxane B2 metabolite
16	470.365	16.66	C27 H50 O6	TG(8:0/8:0/8:0)	84.65	2.79	-0.04	-0.01	No	A	Triacylglycerols
17	416.348	13.13	C30 H40 O	Apo-8'-lycopenal	65.22*	2.78	-0.04	-0.01	No	A	-
18	358.270	9.04	C20 H38 O5	9,12-dimethoxy-13-hydroxy-10-octadecenoic acid	81.58	2.77	-0.04	-0.02	No	A	Methoxy fatty acids
19	276.156	3.72	C14 H20 N4 O2	p-Coumaroylagmatine	85.37	2.67	-0.03	-0.01	No	A	Plant related
20	935.507	0.53	C32 H61 N27 O7	Not identified	68.29*	2.63	-0.03	-0.01	-	A	-
21	396.324	15.53	C22 H42 N3 O3	Not identified	83.53	2.60	-0.04	-0.01	-	A	-
22	450.202	8.17	C27 H30 O6	sofalcone	76.99*	2.60	-0.04	-0.01	No	A	-
23	144.116	7.01	C8 H16 O2	1-Hydroxy-3-octanone	87.70	2.56	-0.03	-0.01	No	A	Flavouring ingredient
24	357.086	11.89	C22 H9 N6	Not identified	79.08*	2.51	-0.02	-0.01	-	A	-
25	745.961	11.78	C24 H12 N O27	Not identified	79.2*	2.50	0.03	0.02	-	C	-
26	320.128	7.66	C17 H20 O6	PR-toxin	77.9*	2.48	0.02	0.03	No	C	Micotoxin
27	656.451	16.94	C36 H64 O10	3-O-(2-O-(2E-decenoyl)-a-L-rhamno-pyranosyl)-3-hydroxydecanoic acid	90.15	2.46	0.03	0.02	No	C	Fatty acyl glycosides, Rhamnolipids
28	260.162	7.21	C13 H22 O4	(3S,5R,6R,7E)-3,5,6-Trihydroxy-7-megastigmen-9-one	86.73	2.45	-0.03	-0.01	No	A	Found in herbs and spices
29	474.356	15.83	C28 H46 N2 O4	Dehydrocarpaine II	70.95*	2.42	-0.04	-0.01	No	A	Found in fruits
30	335.934	3.19	C20 H32 O4	**5S,12S-DiHETE**	84.77	1.99	0.02	0.01	Yes	C	Epimer of leukotriene B4

* ID score below 80%; C: control/healthy samples; A: asthmatic samples

Table 2. Normalized average peak areas for targeted inflammatory biomarkers found in exhaled breath condensate from control and asthmatic subjects.

Pathway	Compound	Times Detected		% total	Norm. Control Peak Area (mean)						Norm. Asthmatic Peak Area (mean)					Norm. Peak Area (mean ± std.)		p value
		Control	Asthmatic	detected	S-01	S-02	S-03	S-04	S-05	S-06	S-07	S-08	S-09	S-10	S-11	Control	Asthmatic	
COX	**PGE2**	46	32	53	0.022	0.955	0.104	0.118	0.023	0.019	0.090	0.217	0.008	0.004	0.021	0.040 ± 0.085	0.003 ± 0.003	**<0.001**
	TXB2	28	18	31	0.016	0.398	0.081	0.049	0.019	0.028	0.120	0.083	0.007	0.005	0.085	0.026 ± 0.037	0.012 ± 0.020	**0.001**
	6-keto-PGF1a	26	14	27	0.005	0.000	0.020	0.159	0.061	0.013	0.298	0.899	0.007	0.004	0.010	0.083 ± 0.269	0.011 ± 0.027	**0.002**
	PGB2	42	39	56	0.156	0.232	0.135	0.173	0.018	0.020	0.160	0.170	0.011	0.011	0.024	0.059 ± 0.192	0.007 ± 0.005	**0.010**
	PGF2a	17	4	14	0.005	0.668	0.034	0.000	0.017	0.007	0.000	0.055	0.000	0.002	0.000	0.035 ± 0.067	0.000 ± 0.000	**0.018**
	PGJ2	32	19	34	0.001	0.068	0.049	0.051	0.011	0.010	0.086	0.081	0.008	0.004	0.018	0.012 ± 0.026	0.001 ± 0.000	0.098
	12(S)-HHTre	8	7	10	0.000	0.000	0.000	0.000	0.006	0.007	0.000	0.061	0.000	0.000	0.037	0.002 ± 0.002	0.007 ± 0.006	0.091
	PGA2	30	16	31	0.001	0.212	0.091	0.055	0.015	0.016	0.059	0.047	0.017	0.004	0.018	0.019 ± 0.038	0.002 ± 0.001	**0.008**
	8-iso-PGF2a	18	2	13	0.004	0.000	0.174	0.000	0.043	0.007	0.000	0.000	0.000	0.004	0.000	0.033 ± 0.077	0.001 ± 0.000	0.208
	15-deoxy-d12,14-PGJ2	19	28	33	0.025	0.000	0.057	0.108	0.016	0.009	0.090	0.000	0.022	0.005	0.030	0.028 ± 0.048	0.004 ± 0.002	0.229
	11-dehydro-TXB2	17	16	23	0.009	0.029	0.069	0.014	0.018	0.018	0.153	0.362	0.055	0.004	0.018	0.018 ± 0.039	0.008 ± 0.007	0.523
	PGD2	11	13	17	0.003	0.000	0.064	0.019	0.010	0.012	0.090	0.268	0.014	0.027	0.014	0.014 ± 0.017	0.012 ± 0.024	0.497
P450	**9(10)-EpOME**	58	53	76	0.015	0.085	0.530	0.143	0.012	0.065	0.341	0.495	0.134	0.109	0.180	0.037 ± 0.045	0.067 ± 0.069	**0.032**
	9(10)-DiHOME	38	47	59	0.090	0.037	0.143	0.179	0.052	0.881	0.825	0.424	0.233	0.243	0.147	0.253 ± 0.573	0.133 ± 0.365	0.136
	12(13)-DiHOME	48	50	68	0.165	0.083	0.219	0.177	0.035	0.326	0.487	0.618	0.129	0.262	0.121	0.115 ± 0.271	0.118 ± 0.400	0.436
	12(13)-EpOME	52	42	64	0.080	0.112	1.000	0.123	0.012	0.031	0.237	0.237	0.204	0.131	0.089	0.065 ± 0.099	0.077 ± 0.100	0.925
5-LOX	**LTD4**	21	19	28	0.009	0.127	0.197	0.079	0.008	0.045	0.175	0.132	0.016	0.003	0.000	0.020 ± 0.010	0.004 ± 0.003	**<0.001**
	5(S)-HETE	34	13	31	0.006	0.197	0.097	0.086	0.015	0.026	0.073	0.043	0.017	0.007	0.042	0.020 ± 0.034	0.004 ± 0.004	**0.001**
	LTC4	15	9	16	0.005	0.040	0.093	0.033	0.004	0.000	0.078	0.063	0.008	0.003	0.031	0.007 ± 0.004	0.002 ± 0.001	**0.029**
	N-acetyl-LTE4	11	14	17	0.004	0.079	0.062	0.029	0.000	0.014	0.080	0.080	0.000	0.002	0.029	0.005 ± 0.003	0.002 ± 0.002	0.054
	LTF4	11	17	20	0.019	0.087	0.161	0.000	0.003	0.000	0.151	0.104	0.000	0.008	0.062	0.021 ± 0.022	0.008 ± 0.005	0.106
	LTE4	17	13	20	0.004	0.073	0.064	0.023	0.012	0.012	0.049	0.000	0.012	0.003	0.022	0.012 ± 0.023	0.002 ± 0.001	0.133
12-LOX	**LXA4**	24	18	29	0.008	0.712	0.072	0.056	0.014	0.018	0.088	0.058	0.021	0.003	0.023	0.016 ± 0.015	0.002 ± 0.001	**<0.001**
	9-oxoODE	7	13	14	0.470	0.000	0.000	0.000	0.000	0.185	0.000	0.000	0.101	0.000	0.053	0.636 ± 0.506	0.023 ± 0.021	**0.008**
15-LOX	**12(S)-HETE**	37	19	38	1.000	0.135	0.256	1.000	1.000	0.126	0.073	0.000	0.036	0.108	0.017	1.000 ± 2.333	0.076 ± 0.162	**0.007**
	13(S)-HODE, 9(S)-HODE	60	59	82	0.736	0.200	0.789	0.624	0.068	1.000	1.000	1.000	1.000	1.000	1.000	0.417 ± 0.777	0.466 ± 0.652	0.229
	15(S)-HETE	38	28	45	0.012	1.000	0.141	0.112	0.037	0.024	0.202	0.484	0.017	0.025	0.036	0.041 ± 0.086	0.021 ± 0.019	0.721
	13-oxoODE	11	13	17	0.533	0.000	0.000	0.000	0.019	0.061	0.224	0.000	0.000	0.062	0.108	0.479 ± 0.569	0.066 ± 0.048	0.532
Oxidation stress	**o-tyrosine**	22	5	18	0.051	0.000	0.520	0.039	0.004	0.061	0.000	0.047	0.000	0.007	0.012	0.045 ± 0.047	0.003 ± 0.002	**0.027**
	8-OH-2'-dG	9	1	6	0.034	0.000	0.000	0.018	0.005	0.014	0.000	0.000	0.000	0.003	0.000	0.027 ± 0.027	0.000 ± 0.000	0.182
Maximum value (mean, a.u.)					408059	26283	25526	78463	767149	155782	12325	19017	109186	316078	79101	237374		
Number of samples		160	133	293	20	28	28	28	28	28	28	28	21	28	28	160	132	**p < 0.05**

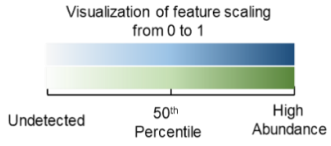

Targeted Eicosanoid Metabolite Analysis

The eicosanoid profile of the EBC samples was also characterized using targeted metabolomic analysis (**Table 2**). From the 30 compounds screened using the LC-MS method, seven were detected in more than half of the samples. We mainly detected in more than 80% of the total samples the sum of 9(S)- and 13(S)-hydroxyoctadecadienoic acids (HODE). These are oxidized derivatives of linoleic acid through 15-LOX pathway. All the compounds which formed through cytochrome P450 pathway (EpOMEs and DiOMEs) and prostaglandins B2 and E2 also appeared in most of the samples. The rest of compounds were detected in less samples, but found in more than 15% of the samples. Except for prostaglandin F2α and 8-isoPGF2α, 15(S)-HHTrE, 9-oxoODE and 8-OHdG that were rarely detected in overall the samples. **Table 2** excludes undetected (zero) values in the dataset, unless if the compound was not ever detected from a subject. In this case, the value was set to zero and visualized with a white color. We found that excluding or including undetected values in the dataset did not significantly alter the metabolomic differences and patterns among subjects and between the control and asthmatic groups (data not shown).

Table 2 shows the averaged peak signal obtained per each sample after normalization by mean and subsequently normalization by feature scaling per subject (blue-scaled columns). Here, we observe differences between individual sample batches. Maximum peak area values are listed in **Table 2**. When the maximum mean peak area values are multiplied by the feature scaled values (0 to 1) in its corresponding column, original average peak area (a.u.) values are obtained. While most of the compounds showed high variability, some of them appeared through all samples at high intensities, like 9(S)- and 13(S)-HODE. However, when peak areas are averaged and feature scaled by the control *and* asthmatic groups, these differences were enhanced (green-scaled columns). 12(S)-HETE presented high intensities for the control samples versus lower amounts for asthmatics. Surprisingly, this tendency occurs in several of

the compounds, by which compounds seem to have lower intensities in asthmatic subjects than the controls.

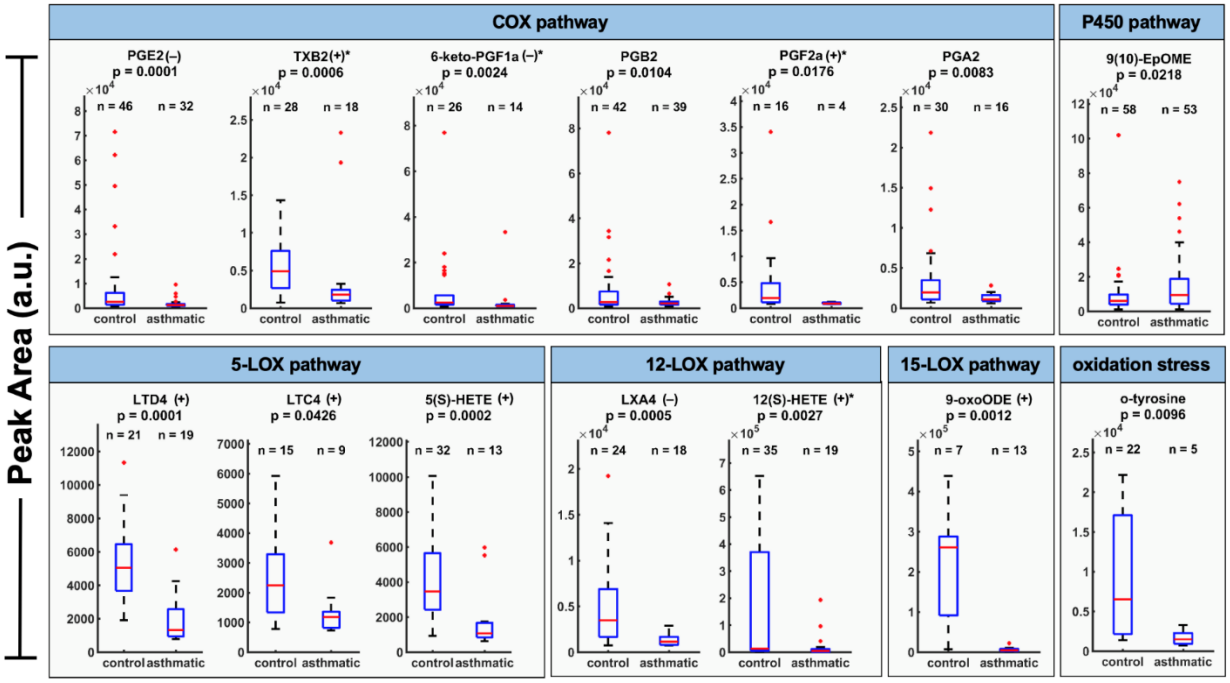

Figure 4. Exhaled breath condensate biomarker peak area distributions, which are significantly correlated between control and asthmatic subjects ($p<0.05$).

To confirm this trend, a Wilcoxon signed rank test was applied to compare medians between the two groups. Fourteen out of thirty targeted compounds showed levels in EBC with significant differences between asthmatics and healthy control subjects ($p<0.05$). The targeted inflammatory biomarkers are shown for control (n=6) and asthmatic (n=5) subjects. Vertical axes are scaled non-uniformly and vary for each biomarker. n values above box plots indicate number of times the compound was detected for the control group and the asthmatic group. Biomarkers are grouped by arachidonic acid cascade metabolomic pathways. Biomarkers labelled with (+) and (–) are known to be pro-inflammatory and anti-inflammatory, respectively. Biomarkers further labelled with an asterisk (*) are likely but inconclusive in literature. The thirty targeted compounds are listed along with their CAS ID, classification, and family in **Supplemental Table S3**. Functional descriptions of these targeted compounds are provided in **Supplemental Table S4**. Abundances of these fourteen compounds are summarized in **Figure**

4, where boxplots are also presented. Undetected (zero) values are excluded in this dataset. Boxplots allow a simple visualization of these differences between groups. We found six compounds that are formed by COX pathway: prostaglandins E2, B2, F2α and A2, thromboxane B2 and 6-keto PGF1α. All seem to be specific from the control subjects, with lower intensities in asthmatics. The same pattern appears with the metabolites generated by 5-, 12- and 15-LOX pathways, which include leukotrienes D4 and C4, lipoxin A4, 5- and 12-HETE and 9-oxoODE, as well as o-tyrosine that is formed by oxidation stress of proteins. 9(10)-EpOME presents an up-regulation towards asthmatics, although there are no studies proving the inflammatory effect of this metabolite. One plausible explanation for this pattern can be the inflammatory suppression caused by the medication prescribed for the asthmatic subjects. These medications can reduce the abundance of compounds, which are related to the asthmatic condition. Peak area distributions of the remaining sixteen compounds are summarized in **Supplemental Figure S3** ($p>0.05$). Responses to asthma medications vary considerably among patients. Additionally, asthma is unlikely to be a single disease, but rather a series of complex, overlapping individual diseases or phenotypes, each defined by unique interactions between genetic and environmental factors.[35] Further asthmatic studies with larger sample sizes and more frequent sampling are needed to verify the effects of medicinal dosage and time of use on metabolomic profiles during breath sampling.

Finally, detected targeted compounds were correlated and studied considering possible confounder parameters and information collected during the study. Temperature and relative humidity considering all samples (24.7 ± 2.7 °C, 45.2 ± 10.6 %RH) showed no significant changes to the abundance of these compounds (data not shown). However, data showed interesting patterns when it was presented longitudinally (**Figure 5**). During the 14 days of collection EBC was sampled morning (AM) and evening (PM), and these time points were clearly differentiated for some of the compounds, such as 12(S)-HETE, 9(S)- and 13(S)-HODE. Vertical axes are scaled non-uniformly and vary for each biomarker. There is a distinct pattern

of a day/night cycle with elevations of peak area values in the evening samples. Moreover, these differences were presented mainly in asthmatic subjects, which can be explained by asthma being a representation of exaggerated amplitudes in comparison to healthy circadian patterns. Average peak areas for all thirty targeted compounds separated into four groups (control/asthmatic, AM/PM) are summarized with boxplots in **Supplemental Figure S4**. This could help further understand the variation of asthmatic symptoms throughout the day with worsened symptoms during the night and early morning.

Conclusion

In future applications, this miniature breath collector may transport the collected sample from its collection surface unit into an interfaced analytical or storage unit with minimal power input. The amount of sample collection could be reduced to a few microliters and sampling time to a few minutes when collection and analysis are possible with novel microfluidic platforms. The miniaturized EBC collection device allows for minimal sample volumes needed for representative studies. This opens a non-invasive way to study metabolic effects of environmental exposure and medical interventions using measurable targets in many health conditions including asthma. Untargeted analysis measures all endogenous metabolic signals in a biological sample, which allows for the discovery of novel biomarkers that can explain differences in health conditions. Targeted analysis allows for quantifying a predefined set of selected metabolites, which are related to certain diseases and medical conditions. Further untargeted metabolite analysis may be explored, similarly done for targeted metabolites. This device is able to finely resolve time data sequence on the order of hours and can lead to a substantial amount of potential data to be collected for increasing the power of various studies. Currently, there are no other reports of EBC studies that allow for monitoring individuals longitudinally instead of cross-sectionally at study visits which can be a major advantage in personal health monitoring. Additionally, its portability is advantageous because it enables breath samples to be collected in multiple environments, including intensive care units (ICUs),

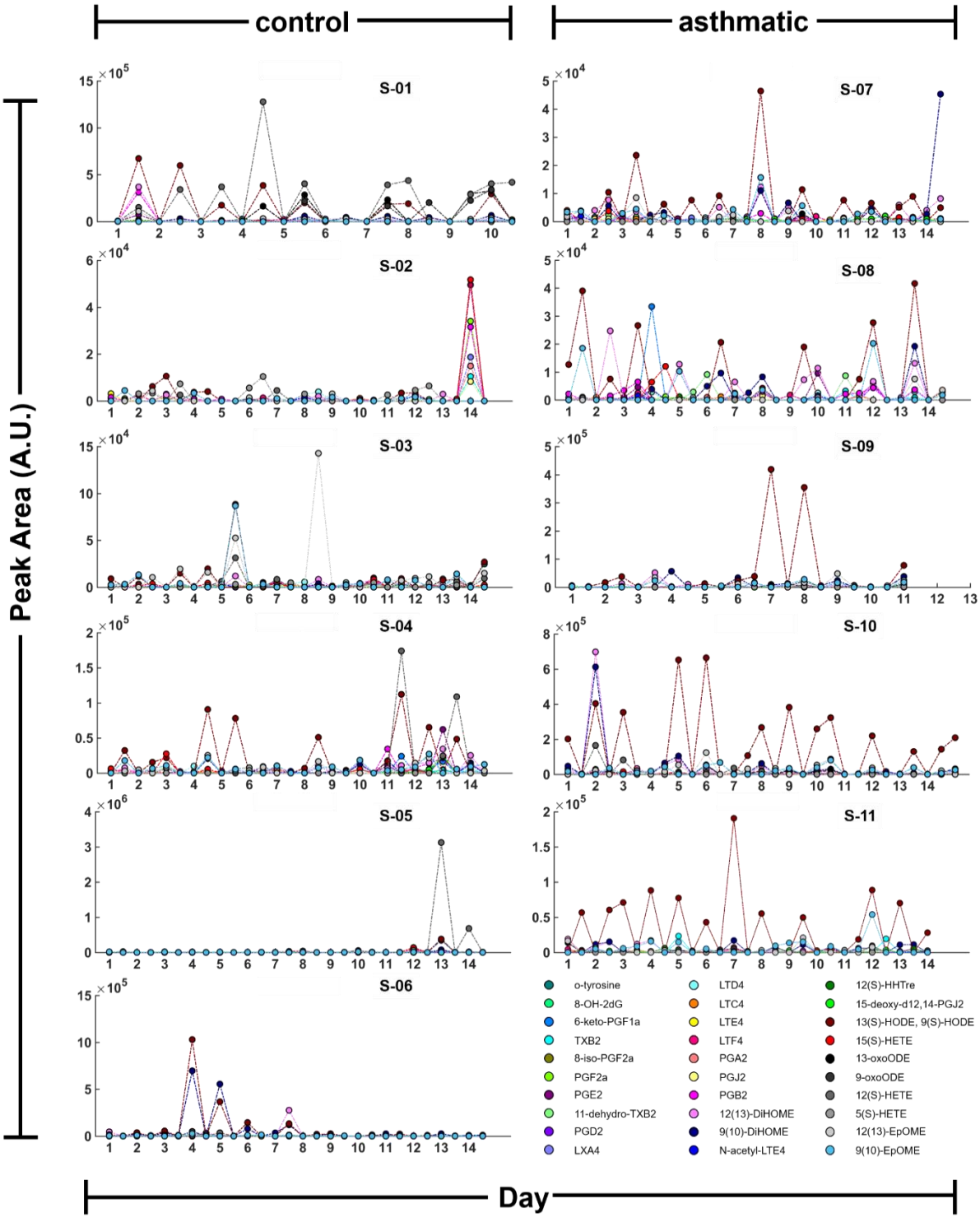

Figure 5. A time course of peak area values for targeted inflammatory biomarkers found in exhaled breath condensate from control and asthmatic subjects.

outpatient clinics, workplaces, and at home.

Inflammatory airway disease such as asthma causes exaggerated fluctuations and amplitudes in metabolomic profiles in comparison to normal circadian patterns. Health conditions of interest, ones that are mostly independent on circadian rhythms, would allow for the pooling of samples to obtain more amount of sample per analysis. This would achieve lower limits of detection to more accurately quantify known biomarkers and discover novel biomarkers. Studies with larger sample sizes would also allow for determining regional differences and dependencies for metabolomic profiles. The addition of positive ionization mode or other alternative separation and detection platforms would present further opportunities to discover more metabolites correlated with other respiratory diseases including asthma.

Conflict of Interest

The authors have a previously issued patents on a component part of the palm-sized breath sampler (US Patent #10,067,119 and US Patent #9,398,881), and one patent pending.

Acknowledgements

Partial support was provided by: NIH award U01 EB0220003-01 (CED, NJK); the NIH National Center for Advancing Translational Sciences (NCATS) through grant UL1 TR000002 (CED, NJK); NIH award 1P30ES023513-01A1 (CED, NJK); NIH award UG3-OD023365 [CED]. The contents of this manuscript are solely the responsibility of the authors and do not necessarily represent the official views of the funding agencies. The authors also gratefully acknowledge access and use of the Food Safety and Measurement Facility in the Department of Viticulture and Enology at UCD for sample analysis. The authors thank Dr. Konstantin Zamuruyev (NASA Jet Propulsion Laboratory, Caltech) for technical discussions. The authors also thank Carolyn Doyle for lyophilization of the samples. Finally, the authors are grateful for all the participating children and their families who devoted their time and samples for the sake of conducting the research.

Supplemental information

Supplemental Table S1. The list of targeted compounds detected by LC-MS/MS. Molecular formula and exact masses are provided together with LC-MS retention times (RT) in minutes and preferred precursor ions used for AutoMS/MS analysis. Confirmation qualifier masses and optimal collision energies are listed.

Compound	Formula	Exact mass	RT (min)	Precursor ion		Qualifier	CE (V)
o-tyrosine	C9 H11 N O3	181.074	0.5	180.1	>	136.1	10
8-OH-2'-dG	C10 H13 N5 O5	283.092	0.5	282.1	>	192.1	20
6-keto-PGF1a	C20 H34 O6	370.236	4.47	369.2	>	163.1	20
8-iso-PGF2a	C20 H34 O5	354.241	5.03	353.2	>	193.1	15
TXB2	C20 H34 O6	370.236	5.06	369.2	>	169.1	10
PGF2a	C20 H34 O5	354.241	5.43	353.2	>	193.1	15
PGE2	C20 H32 O5	352.225	5.68	351.2	>	271.2	5
11-dehydro-TXB2	C20H32O6	368.22	5.81	367.2	>	161.1	15
PGD2	C20 H32 O5	352.225	5.94	351.2	>	271.2	5
LXA4	C20 H32 O5	352.225	6.4	351.2	>	115.04	10
LTC4	C30 H47 N3 O9 S	625.303	6.93	624.3	>	272.7	10
LTD4	C25 H40 N2 O6 S	496.261	6.97	495.3	>	177.03	10
LTE4	C23 H37 N O5 S	439.239	7.09	438.2	>	333.2	10
LTF4	C28 H44 N2 O8 S	568.282	7.11	567.2	>	438.2	10
PGA2	C20 H30 O4	334.214	7.13	333.2	>	271.2	10
PGJ2	C20 H30 O4	334.214	7.29	333.2	>	233.1	5
12(13)-DiHOME	C18 H34 O4	314.246	8.28	313.2	>	183.1	15
9(10)-DiHOME	C18 H34 O4	314.246	8.49	313.2	>	201.1	15
PGB2	C20 H30 O4	334.214	8.63	333.2	>	265.2	5
N-acetyl-LTE4	C25 H39 N O6 S	481.25	8.76	480.2	>	351.2	10
12(S)-HHTre	C17 H28 O3	280.204	8.92	279.2	>	179.1	15
15-deoxy-d12,14-PGJ2	C20 H28 O3	316.204	9.74	315.2	>	271.2	5
13(S)-HODE, 9(S)-HODE	C18 H32 O3	296.235	10.31	295.2	>	195.1	15
15(S)-HETE	C20 H32 O3	320.235	10.6	319.2	>	175.1	10
13-oxoODE	C18 H30 O3	294.219	10.76	293.2	>	113.1	20
9-oxoODE	C18 H30 O3	294.219	11.02	293.2	>	185.1	20
12(S)-HETE	C20 H32 O3	320.235	11.02	319.2	>	179.1	10
5(S)-HETE	C20 H32 O3	320.235	11.27	319.2	>	115.04	10
12(13)-EpOME	C18 H32 O3	296.235	11.67	295.2	>	195.1	15
9(10)-EpOME	C18 H32 O3	296.235	11.81	295.2	>	171.1	15

Supplemental Table S2. Demographic and clinical characteristics of the patients at baseline.

	Asthmatic (n=5)	Healthy (n=6)
Age-year	16.7 ± 1.3	17.2 ± 1.5
Female sex no%	40%	66%
Mean prescribed inhaled corticosteroid dose range μg/day	440 (0-960)	0
Leukotriene-receptor antagonist	60%	N/a
Overall health score (1-5) *	2.5 (2-3)	1.5 (1-2)
Affected by fatigue (0-10)**	4.4 (0-7)	2.5 (0-5)
Affected by shortness of breath (0-10)++	4.2 (2-7)	0
Hours of physical activities/week +++	2.7 (1.5-4.5)	3.16 (1.5-7.5)
• Stretching/strengthening	1.1 (0.5-3.0)	0.42 (0-0.5)
• Other demanding exercise	1.6 (1.0-3.0)	2.75 (1-6.8)
Medical visits in the last 6 months		
• Office visit	3.8 (0-13)	1.3 (0-4)
• ED visit	1 (0-1)	0

*Overall health score with score of 1 indicates excellent health, 5 indicates poor health.
**Fatigue score in the last month with score of 0 indicates no fatigue, 10 indicates severe fatigue
++Shortness of breath in the last month with score of 0 indicates no shortness of breath, 10 indicates severe shortness of breath
+++Hours of physical activities performed weekly in the last month including stretching or other more demanding activities including walking, swimming, bicycling and other aerobic exercise

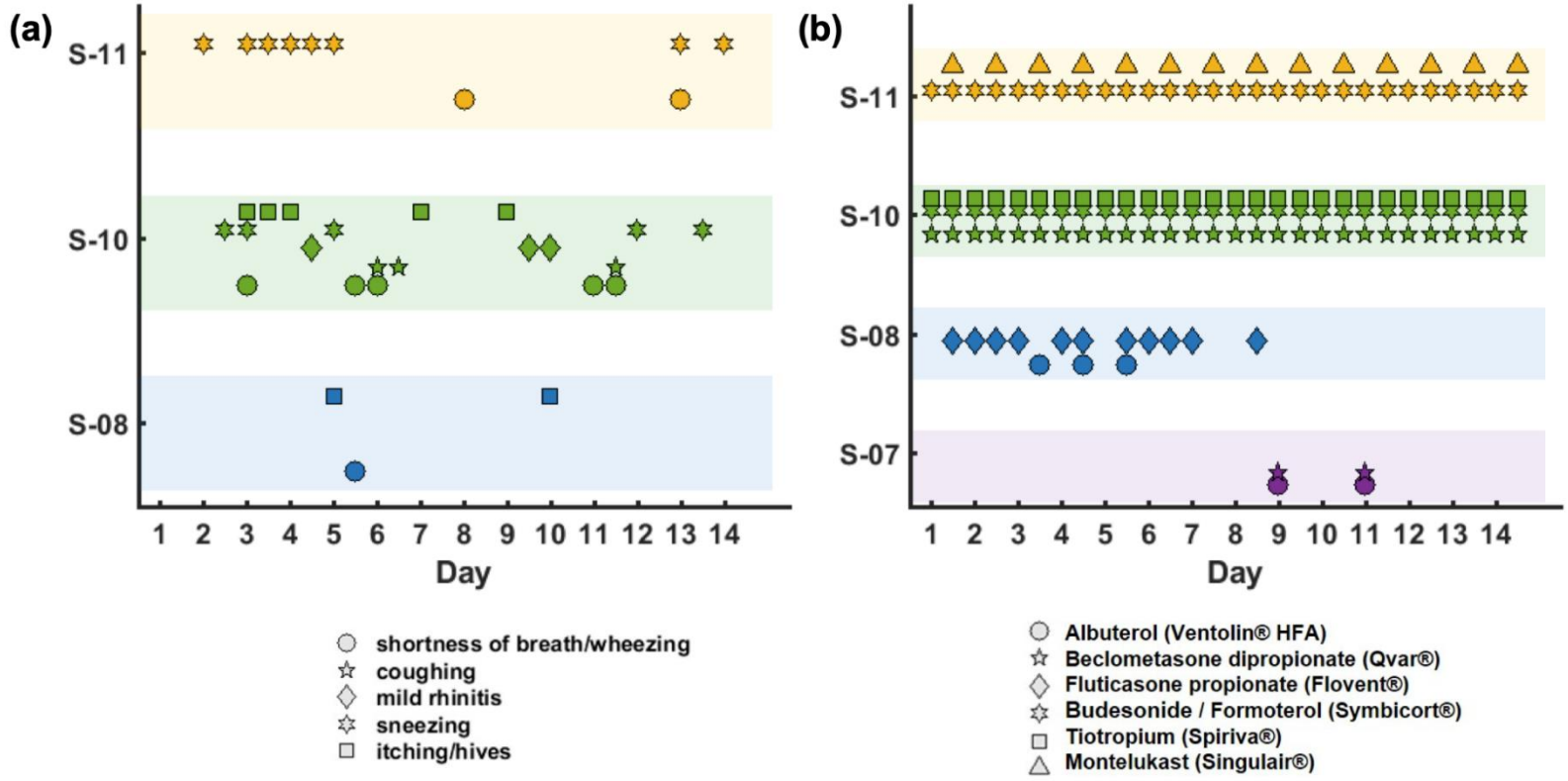

Supplemental Figure S1. Symptoms and medicinal use as reported by subjects during breath sampling in the clinical study. A time series for symptoms of asthmatic participants is presented (a) and medicinal use (b). Subjects not shown did not report any symptoms or report any medicinal use.

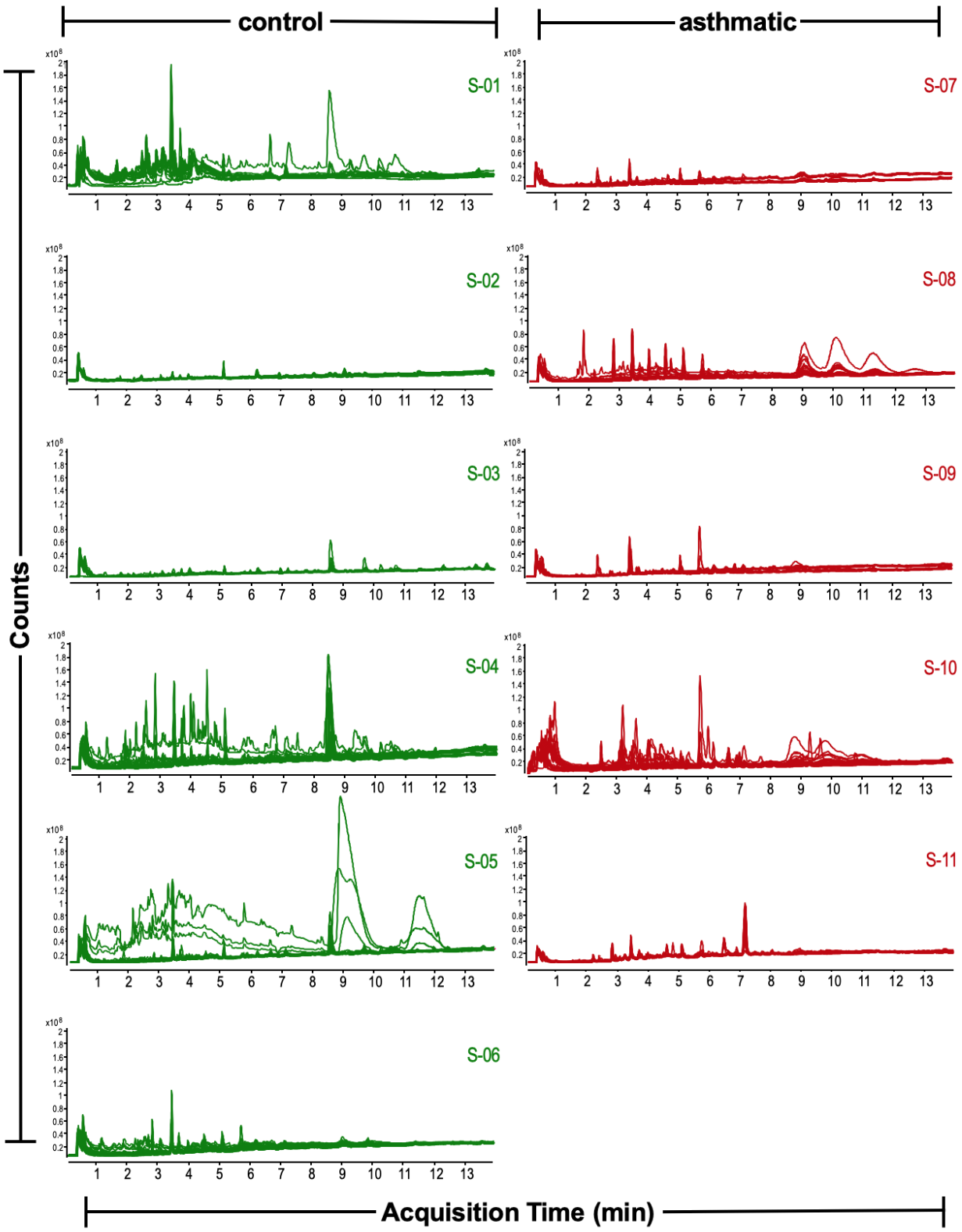

Supplemental Figure S2. Total Ion Chromatograms (TICs) from the exhaled breath condensate samples.

Supplemental Table S3. Targeted inflammatory biomarkers in exhaled breath condensate used in this study.

Compound	Common name	CAS ID	Classification	Family
o-tyrosine	o-tyrosine	709-16-0	Oxidation stress	phenylalanine and derivatives
8-OH-2dG	8-Hydroxy-2'-deoxyguanosine	88847-89-6	Oxidation stress	purine 2'-deoxyribonucleosides
6-keto-PGF1a	6-keto Prostaglandin F1α	58962-34-8	Anti-inflammatory	prostaglandins
TXB2	Thromboxane B2	54397-85-2	Pro-inflammatory	thromboxanes
8-iso-PGF2a	8-iso Prostaglandin F2α	27415-26-5	Pro-inflammatory	prostaglandins
PGF2a	Prostaglandin F2α	551-11-1	Pro-inflammatory	prostaglandins
PGE2	Prostaglandin E2	363-24-6	Anti-inflammatory	prostaglandins
11-dehydro-TXB2	11-dehydro Thromboxane B2	67910-12-7	Pro-inflammatory	thromboxanes
PGD2	Prostaglandin D2	41598-07-6	Pro-inflammatory	prostaglandins
LXA4	Lipoxin A4	89663-86-5	Anti-inflammatory	lipoxins
LTD4	Leukotriene D4	73836-78-9	Pro-inflammatory	leukotrienes
LTC4	Leukotriene C4	72025-60-6	Pro-inflammatory	leukotrienes
LTE4	Leukotriene E4	75715-89-8	Pro-inflammatory	leukotrienes
LTF4	Leukotriene F4	83851-42-7	-	leukotrienes
PGA2	Prostaglandin A2	13345-50-1	-	prostaglandins
PGJ2	Prostaglandin J2	60203-57-8	Anti-inflammatory	prostaglandins
PGB2	Prostaglandin B2	13367-85-6	-	prostaglandins
12(13)-DiHOME	(±)12(13)-DiHOME	263399-35-5	-	long-chain fatty acids
9(10)-DiHOME	(±)9(10)-DiHOME	263399-34-4	-	long-chain fatty acids
N-acetyl-LTE4	N-acetyl Leukotriene E4	80115-95-3	Pro-inflammatory	leukotrienes
12(S)-HHTre	12(S)-HHTrE	54397-84-1	-	-
15-deoxy-d12,14-PGJ2	15-deoxy-Δ12,14-Prostaglandin J2	87893-55-8	Anti-inflammatory	-
13(S)-HODE, 9(S)-HODE	13(S)-HODE, 9(S)-HODE	29623-28-7, 73543-67-6	-	-
15(S)-HETE	15(S)-HETE	54845-95-3	Pro-inflammatory	-
13-oxoODE	13-OxoODE	54739-30-9	Pro-inflammatory	-
9-oxoODE	9-oxoODE	54232-59-6	Pro-inflammatory	-
12(S)-HETE	12(S)-HETE	54397-83-0	Pro-inflammatory	-
5(S)-HETE	5(S)-HETE	70608-72-9	Pro-inflammatory	-
12(13)-EpOME	(±)12,13-Epoxyoctadecenoic acid	-	-	-
9(10)-EpOME	(±)9,10-Epoxyoctadecenoic acid	-	-	-

Compound	Functions	Supporting Sources
o-tyrosine	o-Tyrosine is a normal human metabolite. Its presence is possible due to the hydroxylation of l-phenylalanine by hydroxyl radical (*OH), and is proposed as an hydroxy radical biomarker of oxidative damage to proteins. o-Tyrosine might also be included in the diet and absorbed. It has been associated with disease such as Kwashiorkor, a severe form of protein-energy malnutrition. However, many publications mention that the results are inconclusive.	1. Human Metabolome Database (HMDB) URL: http://www.hmdb.ca/metabolites/HMDB0006050. 2. Manary MJ, Leeuwenburgh C, Heinecke JW: Increased oxidative stress in kwashiorkor. J Pediatr. 2000 Sep;137(3):421-4. 3. Leeuwenburgh C, Hansen PA, Holloszy JO, Heinecke JW: Oxidized amino acids in the urine of aging rats: potential markers for assessing oxidative stress in vivo. Am J Physiol. 1999 Jan;276(1 Pt 2):R128-35.
8-OH-2dG	Produced by oxidative damage of DNA by reactive oxygen and nitrogen species, including hydroxyl radical and peroxynitrite. It serves as a measure of oxidative stress in biological systems. DNA damage due to hydroxyl radical attack at the C8 of guanine, contributing to mutagenicity and cancer promotion.	1. Cayman Chemical URL: https://www.caymanchem.com/product/89320 2. Beckman, K.B., and Ames, B.N. Oxidative decay of DNA The Journal of Biological Chemisty 272, 19633-19636 (1997) 3. Spencer, J.P.E., Jenner, A., Chimel, K., et al. DNA strand breakage and base modification induced by hydrogen peroxide treatment of human respiratory tract epithelial cells FEBS Letters 374, 233-236 (1995).
6-keto-PGF1a	6-keto prostaglandin F1α (6-keto PGF1α) is the inactive, non-enzymatic hydrolysis product of PGI2. 6-keto PGF1α serves as a useful marker of PGI2 biosynthesis in vivo. When [3H]-PGI2 is injected into healthy human males, 6.6% of the radioactivity is recovered from urine as [3H]-6-keto PGF1α. From PGI2, a prostacyclin, inhibits platelet activation and is an effective vasodilator.	1. Cayman Chemical URL: https://www.caymanchem.com/product/15210 2. Pace-Asciak, C.R. Isolation, structure, and biosynthesis of 6-ketoprostaglandin F1α in the rat stomach J. Am. Chem. Soc. 98(8), 2348-2349 (1976). 3. Johnson, R.A., Morton, D.R., Kinner, J.H., et al. The chemical structure of prostaglandin X (prostacyclin) Prostaglandins 12(6), 915-928 (1976).
TXB2	Thromboxane B2 is an inactive metabolite/product of thromboxane A2. It is almost completely cleared in the urine. It itself is not involved in platelet activation and aggregation in case of a wound, but its precursor, thromboxane A2, is. Thromboxane A2 synthesis is the target of the drug aspirin, which inhibits the COX-1 enzyme (the source of thromboxane A2 in platelets). 2-(3,4-Di-hydroxyphenyl)-ethanol (DHPE) is a phenolic component of extra-virgin olive oil.	1. Chemical Entities of Biological Interest (ChEBI), URL: https://www.ebi.ac.uk/chebi/searchId.do?chebiId=CHEBI:28728 2. Good RI, McGarrity A, Sheehan R, James TE, Miller H, Stephens J, Watkins S, McConnachie A, Goodall AH, Oldroyd KG (2015) Variation in thromboxane B2 concentrations in serum and plasma in patients taking regular aspirin before and after clopidogrel therapy. Platelets 26, 17-24.
8-iso-PGF2a	Potent renal vasoconstrictor. 8-iso PGF2α is an isoprostane produced by the non-enzymatic peroxidation of arachidonic acid in membrane phospholipids.1,2,3 It is present in human plasma in two distinct forms - esterified in phospholipids and as the free acid. The ratio of these two forms is approximately 2:1, with a total plasma 8-iso PGF2α level of about 150 pg/ml in normal volunteers. In normal human urine, 8-iso PGF2α levels are about 180-200 pg/mg of creatinine.1,2 8-iso PGF2α is a weak TP receptor agonist in vascular smooth muscle.	1. Cayman Chemical, URL: https://www.caymanchem.com/product/16350 2. Morrow, J.D., Hill, K.E., Burk, R.F., et al. A series of prostaglandin F2-like compounds are produced in vivo in humans by a non-cyclooxygenase, free radical-catalyzed mechanism Proc. Natl. Acad. Sci. U.S.A. 87(23), 9383-9387 (1990). 3. Morrow, J.D., Harris, T.M., and Roberts, L.J., II Noncyclooxygenase oxidative formation of a series of novel prostaglandins: Analytical ramifications for measurement of eicosanoids Anal. Biochem. 184(1), 1-10 (1990).
PGF2a	PF2 bronchoconstriction so PFG2 and 8-iso PGF2α are likely pro-inflammatory in asthma. Prostaglandin F2α (PGF2α) is a widely distributed PG occurring in many species.1,2,3 It causes contraction of vascular, bronchial, intestinal, and myometrial smooth muscle, and also exhibits potent luteolytic activity.	1. Cayman Chemical, URL: https://www.caymanchem.com/product/16010 2. Speroff, L., and Ramwell, P.W. Prostaglandins in reproductive physiology Am. J. Obstet. Gynecol. 107(7), 1111-1130 (1970). 3. Samuelsson, B., Goldyne, M., Granström, E., et al. Prostaglandins and thromboxanes Annu. Rev. Biochem. 47, 997-1029 (1978).
PGE2	Anti-inflammatory, PGE2 has been labeled as proininflammatory because of its multiplicity of effects on the immune system, but in the respiratory system PGE2 has beneficial effects. PGE2 protects against bronchoconstriction, increases relaxation of airway smooth muscle, and has been shown to inhibit the release of mast cell mediators and the recruitment of inflammatory cell.	1. Cayman Chemical, URL: https://www.caymanchem.com/product/14010 2. Arvind, P., Papavassiliou, E.D., Tsioulias, G.J., et al. Prostaglandin E2 down-regulates the expression of HLA-DR antigen in human colon adenocarcinoma cell lines Biochemistry 34(16), 5604-5609 (1995). 3. Robert, A., Schultz, J.R., Nezamis, J.E., et al. Gastric antisecretory and antiulcer properties of PGE2, 15-methyl PGE2, and 16,16-dimethyl PGE2. Intravenous, oral and intrajejunal administration Gastroenterology 70(3), 359-370 (1976).
11-dehydro-TXB2	Stable thromboxane metabolite, is a full agonist of chemoattractant receptor-homologous molecule expressed on TH2 cells (CRTH2) in human eosinophils and basophils. Given its production in the allergic lung, antagonism of the 11-dehydro- thromboxane B2/CRTH2axis may be of therapeutic relevance.	1. Cayman Chemical, URL: https://www.caymanchem.com/product/19500 2. Fitzgerald, G.A., Lawson, J., Blair, I.A., et al. Analysis of urinary metabolites of thromboxane and prostacyclin by negative-ion chemical-ionization gas chromatography/mass spectrometry Advances in Prostaglandin, Thromboxane, and Leukotriene Research 15, 87-90 (1985). 3. Catella, F., Healy, D., Lawson, J.A., et al. 11-dehydro Thromboxane B2: A quantitative index of thromboxane A2 formation in the human circulation Proceedings of the National Academy of Sciences of the United States of America 83, 5861-5865 (1986).
PGD2	PGD2 acts through the thromboxane GPCR, the PGD2 receptor 1 (DP1), and the chemoattractant receptor–homologous molecule expressed on TH2 lymphocytes (CRTH2/DP2). The thromboxane GPCR promotes smooth muscle constriction that likely contributes to bronchoconstriction in asthmatic patients.	1. Cayman Chemical, URL: https://www.caymanchem.com/product/12010 2. Hayaishi, O. Sleep-wake regulation by prostaglandins D2 and E2 J. Biol. Chem. 263(29), 14593-14596 (1988). 3. Giles, H., and Leff, P. The biology and pharmacology of PGD2 Prostaglandins 35(2), 277-300 (1988).
LXA4	Anti-inflammatory, In asthma, LXA4 has been proved to suppress airway hyper-responsiveness and pulmonary inflammation. Lipoxin A4 (LXA4) is a trihydroxy fatty acid containing a conjugated tetraene, produced by the metabolism of (±)15-HETE or 15-HpETE with human leukocytes.1 LXA4 is equipotent to leukotriene B4 in inducing superoxide generation in human neutrophils at 0.1 μM.2 LXA4 is associated with several other biological functions including leukocyte activation, chemotaxis effects, natural killer cell inhibition, and monocyte migration and adhesion.	1. Cayman Chemical, URL: https://www.caymanchem.com/product/90410 2. Ramstedt, U., Serhan, C.N., Nicolaou, K.C., et al. Lipoxin A-induced inhibition of human natural killer cell cytotoxicity: Studies on stereospecificity of inhibition and mode of action J. Immunol. 138(1), 266-270 (1987). 3. Maddox, J.F., and Serhan, C.N. Lipoxin A4 and B4 are potent stimuli for human monocyte migration and adhesion: Selective inactivation by dehydrogenation and reduction J. Exp. Med. 183(1), 137-146 (1996).
LTD4	Pro-inflammatory in asthma, bronchoconstriction in humans. LTD4 is one of the constituents of slow-reacting substance of anaphylaxis (SRS-A) produced by the metabolism of LTC4 by γ-glutamyl transpeptidase. It is the first cysteinyl-leukotriene metabolite of LTC4. Like LTC4, LTD4-induced bronchoconstriction and enhanced vascular permeability contribute to the pathogenesis of asthma and acute hypersensitivity. LTD4 is equipotent to LTC4 in its biological activities, except that LTD4 is nearly 100-fold more effective in the contraction of peripheral airway smooth muscle.	1. Cayman Chemical, URL: https://www.caymanchem.com/product/20310 2. Örning, L., Hammarström, S., and Samuelsson, B. Leukotriene D: A slow reacting substance from rat basophilic leukemia cells Proceedings of the National Academy of Sciences of the United States of America 77, 2014-2017 (1980). 3. Hammarström, S., Örning, L., and Bernström, K. Metabolism of leukotrienes Molecular and Cellular Biochemistry 69, 7-16 (1985).

Supplemental Table S4. Function descriptions of the thirty targeted inflammatory biomarkers.

Compound	Functions	Supporting Sources
LTC4	Pro-inflammatory in asthma, bronchoconstriction in humans. Leukotriene C4 (LTC4) is the parent cysteinyl leukotriene produced by the LTC4 synthase catalyzed conjugation of glutathione to LTA4. LTC4 is produced by neutrophils, macrophages, mast cells, and by transcellular metabolism in platelets. It is one of the constituents of slow-reacting substance of anaphylaxis (SRS-A) and exhibits potent smooth muscle contracting activity. LTC4-induced bronchoconstriction and enhanced vascular permeability contribute to the pathogenesis of asthma and acute allergic hypersensitivity. The concentration of LTC4 required to produce marked contractions of lung parenchymal strips and isolated tracheal rings is about 1 nM.	1. Cayman Chemical, URL: https://www.caymanchem.com/product/20210 2. Maclouf, J.A., and Murphy, R.C. Transcellular metabolism of neutrophil-derived leukotriene A4 by human platelets. A potential cellular source of leukotriene C4 J. Biol. Chem. 263(1), 174-181 (1988). 3. Piper, P.J. Formation and actions of leukotrienes Physiol. Rev. 64(2), 744-761 (1984). 4. Samuelsson, B. Leukotrienes: Mediators of immediate hypersensitivity reactions and inflammation Science 220(4597), 568-575 (1983). 5. Lefer, A.M. Leukotrienes as mediators of ischemia and shock Biochem. Pharmacol. 35(2), 123-127 (1986).
LTE4	Pro-inflammatory in asthma, bronchoconstriction in humans. Leukotriene E4 (LTE4) is produced by the action of dipeptidase on LTD4, leaving only the cysteinyl group still attached to the fatty acid backbone. It is one of the constituents of slow-reacting substance of anaphylaxis (SRS-A). LTE4 is considerably less active (8 to 12-fold) than LTC4 in the biological activities characteristic of cysteinyl leukotrienes. Unlike LTC4 and LTD4, LTE4 accumulates in both plasma and urine. Therefore, urinary excretion of LTE4 is often used as an indicator of asthma. In humans, basal levels of LTE4 range from 1-100 pg/mg creatinine. In asthmatic patients, urinary LTE4 levels increase to 80-1,000 pg/mg creatinine.	1. Cayman Chemical, URL: https://www.caymanchem.com/product/20410 2. Bernström, K., and Hammarström, S. Metabolism of leukotriene D by porcine kidney J. Biol. Chem. 256(18), 9579-9582 (1981). 3. Samuelsson, B. Leukotrienes: Mediators of immediate hypersensitivity reactions and inflammation Science 220(4597), 568-575 (1983). 4. Lefer, A.M. Leukotrienes as mediators of ischemia and shock Biochem. Pharmacol. 35(2), 123-127 (1986).
LTF4	A weak agonist in its ability to contract vascular smooth muscle.	1. Cayman Chemical, URL: https://www.caymanchem.com/product/20520 2. Bernstrom, K., and Hammarström, S. A novel leukotriene formed by transpeptidation of leukotriene E4 Biochemical and Biophysical Research Communications 109, 800-804 (1982). 3. Lord, A., Charleson, S., and Letts, L.G. Leukotriene F4 and the release of arachidonic acid metabolites from perfused guinea pig lungs in vitro Prostaglandins 29, 651-660 (1985).
PGA2	Plays a vital role in the induction of apoptosis. Blocks the cell cycle progression of NIH 3T3 cells at the G1 and G2/M phase. Additionally acts as a vasodilator with natriuretic properties.	1. Cayman Chemical, URL: https://www.caymanchem.com/product/10210 2. Fukushima, M., Kato, T., Narumiya, S., et al. Prostaglandin A and J: Antitumor and antiviral prostaglandins Adv. Prostaglandin Thromboxane Leukot. Res. 19, 415-418 (1989). 3. Hitomi, M., Shu, J., Strom, D., et al. Prostaglandin A2 blocks the activation of G1 phase cyclin-dependent kinase without altering mitogen-activated protein kinase stimulation J. Biol. Chem. 271(16), 9376-9383 (1996).
PGJ2	Prostaglandin J2 (PGJ2) is formed from PGD2 by the elimination of the C-9 hydroxyl group, a process which is accelerated by the presence of albumin. PGJ2 inhibits platelet aggregation with an IC50 of about 5-10 nM. PGJ2 has antimitotic and antiproliferative effects on a variety of cultured normal cells and tumor cell lines.	1. Cayman Chemical, URL: https://www.caymanchem.com/product/18500 2. Fitzpatrick, F.A., and Wynalda, M.A. Albumin-catalyzed metabolism of prostaglandin D2. Identification of products formed in vitro The Journal of Biological Chemisty 258, 11713-11718 (1983). 3. Bundy, G.L., Morton, D.R., Peterson, D.C., et al. Synthesis and platelet aggregation inhibiting activity of prostaglandin D analogues Journal of Medicinal Chemistry 26, 790-799 (1983).
PGB2	Prostaglandin B2 (PGB2) is a non-enzymatic dehydration product resulting from the treatment of PGE2 or PGA2 with strong base. It has weak agonist activity on TP receptors and can increase pulmonary blood pressure in the rabbit at relatively high doses (5 µg/kg).	1. Cayman Chemical, URL: https://www.caymanchem.com/product/11210 2. Liu, F., Orr, J.A., and Wu, J.Y. Prostaglandin B2-induced pulmonary hypertension is mediated by TXA2/PGH2 receptor stimulation Journal of the American Physiological Society 1040, L602-L607 (1994).
12(13)-DiHOME	Lineloic acid metabolite, epoxide hydrolase metabolite of the leukotoxin12,13-EpOME. have neutrophil chemotactic activity. 12,13-DiHOME suppress the neutrophil respiratory burst by a mechanism distinct from that of respiratory burst inhibitors such as cyclosporin H or lipoxin A4,which inhibit multiple aspects of neutrophil activation. 12,13-DHOME is a derivative of linoleic acid diol that have been reported to be toxic in human's tissue preparations. 12,13-DHOME is a naturally occurring proliferator-activated receptor (PPAR) gamma2 ligand, which stimulates adipocytes and inhibits osteoblast differentiation.	1. Cayman Chemical, URL: https://www.caymanchem.com/product/10009832 2. Moran, J.H., Weise, R., Schnellmann, R.G., et al. Cytotoxicity of linoleic acid diols to renal proximal tubular cells Toxicology and Applied Pharmacology 146, 53-59 (1997). 3. Moran, J.H., Nowak, G., and Grant, D.F. Analysis of the toxic effects of linoleic acid, 12,13-cis-epoxyoctadecenoic acid, and 12,13-dihydroxyoctadecenoic acid in rabbit renal cortical mitochondria Toxicology and Applied Pharmacology 172, 150-161 (2001).
9(10)-DiHOME	Lineloic acid metabolite. Leukotoxin is the 9(10) epoxide of linoleic acid, generated by neutrophils during the oxidative burst. This unstable compound is rapidly degraded by epoxide hydrolases to form the diol, (±)9(10)-DiHOME.4 Mitochondrial dysfunction, vasodilation, and apoptosis are features of leukotoxin toxicity. In renal proximal tubular cells, the diol hydrolysis products of leukotoxin, such as (±)9(10)-DiHOME, have been directly implicated as the cytotoxic agent responsible for cell death.	1. Cayman Chemical, URL: https://www.caymanchem.com/product/53400 2. Hayakawa, M., Sugiyama, S., Takamura, T., et al. Neutrophils biosynthesize leukotoxin, 9,10-epoxy-12-octadecenoate Biochemical and Biophysical Research Communications 137, 424-430 (1986). 3. Ishizaki, T., Takahashi, H., Ozawa, T., et al. Leukotoxin, 9,10-epoxy-12-octadecenoate causes pulmonary vasodilation in rats Journal of the American Physiological Society 1040, L123-L128 (1995).
N-acetyl-LTE4	N-acetyl-LTE4 is the major inactive metabolite of LTE4 found in bile. This route of metabolism is prominent in the rat, but of minor importance in humans. N-acetyl LTE4 is 100 times less potent than LTC4 as a vasoconstricting agent. In healthy human subjects urinary excretion of N-acetyl LTE4 is about 1.5 nmol/mol creatinine, which is considerably less than that of LTE4 (12 nmol/mol creatinine).	1. Cayman Chemical, URL: https://www.caymanchem.com/product/20420 2. Denzlinger, C., Rapp, S., Hagmann, W., et al. Leukotrienes as mediators in tissue trauma Science 230, 330-332 (1985). 3. Foster, A., Fitzsimmons, B., and Letts, L.G. The synthesis of N-acetyl-leukotriene E4 and its effects on cardiovascular and respiratory function of the anesthetized pig Prostaglandins 31, 1077-1086 (1986).
12(S)-HHTre	12(S)-HHTrE is a product of the cyclooxygenase (COX) pathway and one of the primary arachidonic acid metabolites of human platelets. It is biosynthesized by thromboxane (TXA2) synthase from prostaglandin H2 (PGH2) concurrently with TXA2. 12(S)-HHTrE is a natural lipid agonist of the leukotriene B2 receptor BLT2 in vivo that induces chemotaxis of mast cells and accelerates wound closure.2,3 12(S)-HHTrE is avidly oxidized to 12-oxoHTrE by porcine 15-hydroxy PGDH.	1. Cayman Chemical, URL: https://www.caymanchem.com/product/34590 2. Diczfalusy, U., Falardeau, P., and Hammarström, S. Conversion of prostaglandin endoperoxides to C17-hydroxy acids catalyzed by human platelet thromboxane synthase FEBS Letters 84, 271-274 (1977). 3. Okuno, T., Iizuka, Y., Okazaki, H., et al. 12(S)-hydroxyheptadeca-5Z, 8E, 10E-trienoic acid is a natural ligand for leukotriene B4 receptor 2 Journal of Experimental Medicine 1-8 (2008).

Supplemental Table S4 (continued). Function descriptions of the thirty targeted inflammatory biomarkers.

Compound	Functions	Supporting Sources
15-deoxy-d12,14-PGJ2	A natural PPARgamma ligand which has potent anti-inflammatory properties. 15-deoxy-Δ12,14-Prostaglandin J2 (15-deoxy-Δ12,14-PGJ2) is formed from PGD2 by the elimination of two molecules of water. It binds selectively to PPARγ with an EC50 value of 2 μM in a murine chimera system. 15-deoxy-Δ12,14-PGJ2 is more potent than PGD2, Δ12-PGJ2, and PGJ2 in stimulating lipogenesis in C3H10T1/2 cells. The EC50 for induction of adipocyte differentiation in cultured fibroblasts is 7 μM.	1. Cayman Chemical, URL: https://www.caymanchem.com/product/18570 2. Kliewer, S.A., Lenhard, J.M., Willson, T.M., et al. A prostaglandin J2 metabolite binds peroxisome proliferator-activated receptor γ and promotes adipocyte differentiation Cell 83(5), 813-819 (1995). 3. Forman, B.M., Tontonoz, P., Chen, J., et al. 15-Deoxy-Δ12,14-prostaglandin J2 is a ligand for the adipocyte determination factor PPARγ Cell 83(5), 803-812 (1995).
13(S)-HODE, 9(S)-HODE	13(S)-hydroperoxy-9Z,11E-octadecadienoic acid (13(S)-HpODE is reduce by peroxidase to to 13 HODE (15 LOX-1 pathway using lineloic acid). In guinea pigs, 13(S)-HODE, when injected intravenously, causes a narrowing of lung airways and, when inhaled as an aerosol, mimics the asthmatic hypersensitivity to agents that cause bronchoconstriction by increasing airway narrowing responses to methacholine and histamine.	1. Cayman Chemical, URL: https://www.caymanchem.com/product/38610 2. Buchanan, M.R., Haas, T.A., Lagarde, M., et al. 13-Hydroxyoctadecadienoic acid is the vessel wall chemorepellant factor, LOX The Journal of Biological Chemisty 260, 16056-16059 (1985). 3. Honn, K.V., Nelson, K.K., Renaud, C., et al. Fatty acid modulation of tumor cell adhesion to microvessel endothelium and experimental metastasis Prostaglandins 44(5), 413-429 (1992).
15(S)-HETE	Metabolite of 15 LOX1. 15(S)-HETE is a major arachidonic acid metabolite from the 15-lipoxygenase pathway. In mammals, 15(S)-HETE is synthesized in the respiratory epithelium, leukocytes, and reticulocytes. 15(S)-HETE is present in μg/ml concentrations in the nasal secretions of allergic rhinitis.	1. Cayman Chemical, URL: https://www.caymanchem.com/product/34720 2. Nadel, J.A., Conrad, D.J., Ueki, I.F., et al. Immunocytochemical localization of arachidonate 15-lipoxygenase in erythrocyes, leukocytes, and airway cells Journal of Clinical Investigation 87, 1139-1145 (1991).
13-oxoODE	13-oxoODE is produced from 13-HODE by a NAD+-dependent dehydrogenase present in rat colonic mucosa. 13-OxoODE stimulates cell proliferation when instilled intrarectally in rats. 13-OxoODE has also been detected in preparations of rabbit reticulocyte plasma and mitochondrial membranes, mostly esterified to phospholipids. Production of 13-oxoODE is putatively linked to the maturation of reticulocytes to erythrocytes through the activity of 15-LO.	1. Cayman Chemical, URL: https://www.caymanchem.com/product/38620 2. Earles, S.M., Bronstein, J.C., Winner, D.L., et al. Metabolism of oxidized linoleic acid: Characterization of 13-hydroxyoctadecadienoic acid dehydrogenase activity from rat colonic tissue Biochimica et Biophysica Acta 1081, 174-180 (1991). 3. Bull, A.W., and Bronstein, J.C. Production of unsaturated carbonyl compounds during metabolism of hydroperoxy fatty acids by colonic homogenates Carcinogenesis 11, 1699-1704 (1990).
9-oxoODE	Occurs naturally and particularly under conditions of oxidative stress forms concurrently with 13-HODE. 9-OxoODE results from oxidation of the allylic hydroxyl of either 9(S)- or 9(R)-HODE. Rabbit reticulocyte plasma and mitochondrial membranes contain both 9- and 13-oxoODEs, representing about 2% of the total linoleate residues in the membranes. Most of these oxidized linoleate residues are esterified to membrane lipids.	1. Cayman Chemical, URL: https://www.caymanchem.com/product/38420 2. Kühn, H., Belkner, J., and Wiesner, R. Subcellular distribution of lipoxygenase products in rabbit reticulocyte membranes Eur. J. Biochem. 191(1), 221-227 (1990). 3. Kühn, H., Belkner, J., and Wiesner, R. Metabolism of polyenoic fatty acids by rabbit reticulocytes. Intracellular action of the erythroid lipoxygenase on membrane lipids Biomedica Biochimica Acta 49, S25-S30 (1990).
12(S)-HETE	12(S)-HETE is the predominant lipoxygenase product of mammalian platelets.1 It enhances tumor cell adhesion to endothelial cells, fibronectin, and the subendothelial matrix at 0.1 μM.	1. Cayman Chemical, URL: https://www.caymanchem.com/product/34570 2. Hamberg, M., and Samuelsson, B. Prostaglandin endoperoxides. Novel transformations of arachidonic acid in human platelets Proc. Natl. Acad. Sci. U.S.A. 71(9), 3400-3404 (1974). 3. Grossi, I.M., Fitzgerald, L.A., Umbarger, L.A., et al. Bidirectional control of membrane expression and/or activation of the tumor cell IRGpIIb/IIIa receptor and tumor cell adhesion by lipoxygenase products of arachidonic acid and linoleic acid Cancer Res. 49(4), 1029-1037 (1989).
5(S)-HETE	5(S)-HETE is produced by the action of 5-LO on arachidonic acid to give 5(S)-HpETE, followed by reduction of the hydroperoxide. 5(S)-HETE has proliferative and chemotactic effects on granulocytes. When further metabolized to 5-oxoETE, it is a more potent eosinophil chemoattractant than leukotriene B4.	1. Cayman Chemical, URL: https://www.caymanchem.com/product/34230 2. Dodge, W., and Thomas, M. The effect of 5-hydroxyeicosatetraenoic acid on the proliferation of granulocyte progenitors and embryonic fibroblasts of the chick Biochem. Biophys. Res. Commun. 131(2), 731-735 (1985). 3. Schwenk, U., and Schröder, J.M. 5-Oxo-eicosanoids are potent eosinophil chemotactic factors. Functional characterization and structural requirements J. Biol. Chem. 270(25), 15029-15036 (1994).
12(13)-EpOME	Lineloic acid metabolite. 12, 13-EpOME is the 12, 13-cis epoxide of linoleic acid, generated by neutrophils during the oxidative burst. The toxicity and biosynthesis of 12, 13-EpOME has not been well differentiated from 9, 10-EpOME, but has been presumed to be essentially the same.	1. Cayman Chemical, URL: https://www.caymanchem.com/product/52450 2. Hayakawa, M., Sugiyama, S., Takamura, T., et al. Neutrophils biosynthesize leukotoxin, 9,10-epoxy-12-octadecenoate Biochemical and Biophysical Research Communications 137, 424-430 (1986). 3. Ozawa, T., Hayakawa, M., Takamura, T., et al. Biosynthesis of leukotoxin, 9,10-epoxy-12 octadecenoate, by leukocytes in lung lavages of rat after exposure to hyperoxia Biochemical and Biophysical Research Communications 134, 1071-1078 (1986).
9(10)-EpOME	Lineloic acid metabolite. (±)9(10)-EpOME is the 9,10-cis epoxide of linoleic acid, generated by neutrophils during the oxidative burst. It has been recovered from the lungs of hyperoxic rats and from humans with acute respiratory distress syndrome. Mitochondrial dysfunction is the main feature of (±)9(10)-EpOME cytotoxicity, which may be due to the diol metabolites as well as the parent epoxide.	1. Cayman Chemical, URL: https://www.caymanchem.com/product/52400 2. Hayakawa, M., Sugiyama, S., Takamura, T., et al. Neutrophils biosynthesize leukotoxin, 9,10-epoxy-12-octadecenoate Biochemical and Biophysical Research Communications 137, 424-430 (1986). 3. Ozawa, T., Hayakawa, M., Takamura, T., et al. Biosynthesis of leukotoxin, 9,10-epoxy-12 octadecenoate, by leukocytes in lung lavages of rat after exposure to hyperoxia Biochemical and Biophysical Research Communications 134, 1071-1078 (1986).

Supplemental Table S4 (continued). Function descriptions of the thirty targeted inflammatory biomarkers.

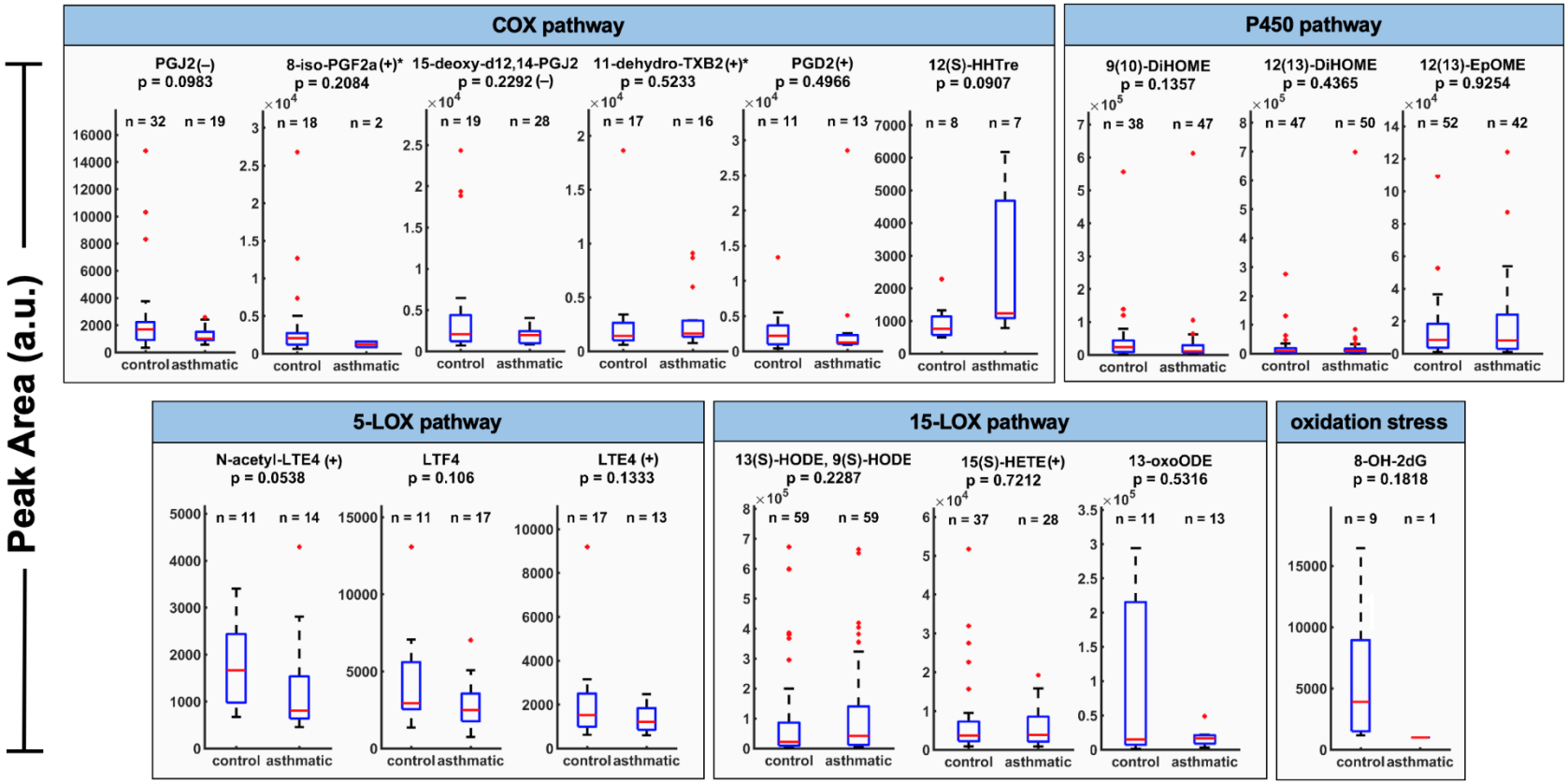

Supplemental Figure S3. Peak area distributions of the remaining sixteen inflammatory biomarkers (p>0.05).

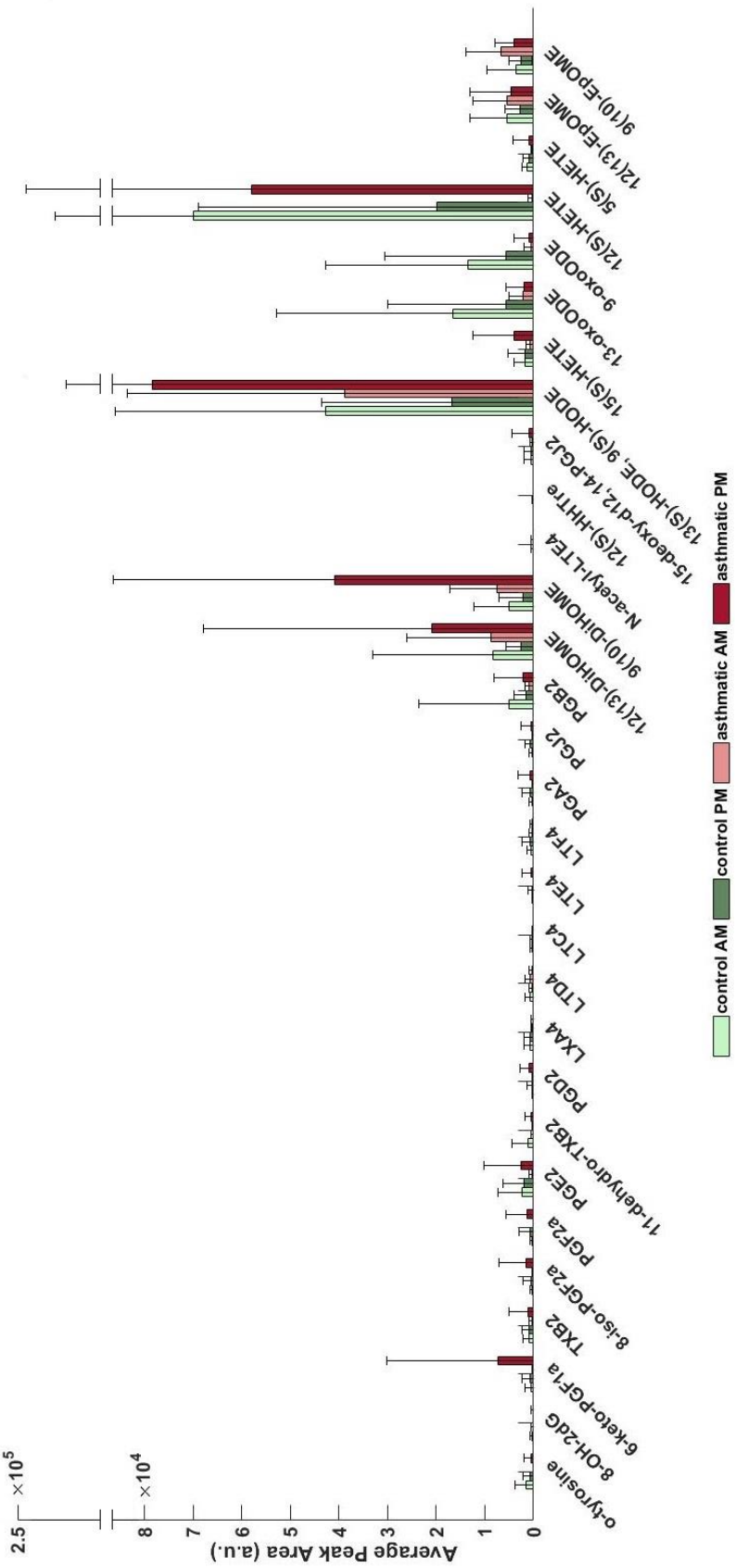

Supplemental Figure S4. Average peak areas for all thirty targeted compounds separated into four groups (control/asthmatic, AM/PM).

Chapter 3: Investigating the relationship between breath aerosol size and exhaled breath condensate (EBC) metabolomic content

Alexander J. Schmidt, Eva Borras, Nicholas J. Kenyon, Cristina E. Davis

Journal of Breath Research (2020) 14: 047104
DOI: 10.1088/1752-7163/abb764

Authorship contributions

Alexander J. Schmidt: Conceptualization, device design, simulation, and testing, experiment planning, experimental data, review of data and results, writing original draft, writing review, and editing. **Eva Borras:** Conceptualization, experiment planning, experimental data, review of data and results, writing review, and editing. **Nicholas J. Kenyon:** Conceptualization, funding, mentoring, supervision, writing review and editing. **Cristina E. Davis:** Conceptualization, experiment planning, review of data and results, funding, mentoring, supervision, writing original draft, writing review and editing.

Abstract

Exhaled breath aerosols contain valuable metabolomic content due to gas exchange with blood at the alveolar capillary interface in the lung. Passive and selective filtering of these aerosols and droplets may reduce the amount of saliva contaminants and serve as an aid to enhance targeted metabolomic content when sampled in EBC. It is currently unknown if breath aerosol size distribution affects the types or abundances of metabolites sampled through EBC. This pilot study uses a previously described hand-held human breath sampler device with varying notch filter geometries to redirect the trajectory of breath aerosols based on size. Ten notch filter lengths were simulated with the device to calculate the effect of filter length on the breath aerosol size distribution and the proportion of aerosols which make their way through to an EBC collection tube. From three notch filter lengths, we investigate metabolite content of various aerosol fractions. We analyzed the non-volatile fraction of breath condensate with high performance liquid chromatography mass spectrometry (LC-MS) for broad metabolite coverage.

We hypothesize that: (1) increasing the length of the notch filter in this device will prevent larger aerosols from reaching the collection tube thus altering the breath aerosol size distribution sampled in EBC; and (2) there is not a systematic large-scale difference in EBC metabolomic content that correlates with breath aerosol size. From simulation results, particles typically larger than 10 µm were filtered out. This indicates that a longer notch filter in this device prevents larger particles from reaching the collection tube thus altering the aerosol particle size distribution. Most compounds were commonly present in all three filter lengths tested, and we did not see strong statistical evidence of systematic metabolite differences between breath aerosol size distributions.

Introduction

Exhaled breath aerosols contain valuable metabolomic content due to gas exchange with blood at the alveolar capillary interface in the lung. Two possible mechanisms of breath aerosol generation in the lung are droplet formations at the air-liquid interface due to shear forces in the upper airways, as well as from a reopening of terminal airway structures. There is a tendency for airways to narrow upon expiration and expand during inhalation, which can create tiny aerosols.[36] Exhaled breath is a complex mixture that contains primary respiratory gases, volatile organic compounds (VOCs), and non-volatile compounds from the liquid lining of the lung.[37] Exhaled breath aerosol sampling is a simple and non-invasive medium for public health and occupational exposure biomonitoring.[38] Due to the COVID-19 pandemic, critical attention is warranted on infectious aerosols sourced from respiratory activities.[39–41] The use of respirator surfaces, hospital masks, and ventilators for trapping these aerosols has been discussed.[38,42] Here, we present novel technology for exhaled breath sampling, non-targeted metabolomic analysis, and sizing of exhaled aerosols.

Exhaled breath condensate (EBC) is a fraction of breath that contains water soluble volatiles and non-volatile compounds[1]. It is a biological matrix in which biomarkers may be identified, similar to saliva and blood and can allow for the discovery of new metabolites and can provide

additional health information. Passive and selective filtering of these aerosols and droplets may reduce the amount of saliva contaminants and serve as an aid to enhance targeted metabolomic content when sampled in EBC. The design of a breath sampling device will inevitably affect the particle size range of the collected sample. For instance, long tubing and sharp turns will contribute to losses of larger aerosols. A standardized collection method should thus consider sampling device geometry to account for different aerosol size distributions. Currently, no EBC collection methods count the number of aerosol particles or enable differentiation of their sizes.

It is currently unknown if breath aerosol size distribution affects the types or abundances of metabolites sampled through EBC. In the last few decades, multiple approaches have been carried out to determine the size distribution of exhaled aerosols. Early studies used glass slides and filters with subsequent microscopic analyses which often determined the sizes of droplets above the micron range.[43,44] In more recent studies, sensitive sampling-based optical particle counters measured aerosols from up to five individuals that were in the submicron size range.[45,46] An instrument limit of detection for breath aerosol sizes can inadvertently skew a measured size distribution if they are unable to detect smaller aerosol sizes. Another common issue in previous studies is that exhaled aerosol sizes were not measured immediately at the mouth or nose exits. These droplets may go through evaporation, dilution, sampling loss, and other influences from the environment before being measured, which causes error in estimating the original size distribution. Aerosol size distribution during normal tidal breathing has been observed to be similar among up to 16 individuals investigated with diameters primarily in the submicron range.[47–49] Particles expelled from other breathing activities (i.e. coughing and talking) may be much larger (> 10 µm).[43,50] These larger particles may also be present during tidal breathing, especially through longer sampling durations (5-15 mins) and when non-tidal episodes can occur.[46] Currently, a category of sampling devices are available to collect breath aerosols with specifically designed polymer filters, and are used for drug monitoring.[51]

This pilot study uses a previously described hand-held human breath sampler device with varying notch filter geometries to redirect the trajectory of breath aerosols based on size.[2] Curved flow profiles have greater inertial effects on larger breath aerosols which cause them to strike the interior walls before they can arrive at a collection site. Shorter notch filter lengths allow larger particles ($\gtrsim$ 10 µm diameter) to pass through while longer notch filter lengths restrict airflow and prevent larger particles from reaching the collection site. In this present work, we investigate metabolite content of various aerosol fractions. We analyzed the non-volatile fraction of breath condensate with high performance liquid chromatography mass spectrometry (LC-MS) for broad metabolite coverage.[3] Additionally, we simulate the trajectories of these aerosols with varying notch filter lengths using COMSOL Multiphysics® software. We hypothesize that: (1) increasing the length of the notch filter in this device will prevent larger aerosols from reaching the collection tube thus altering the breath aerosol size distribution sampled in EBC; and (2) there is not a systematic large-scale difference in EBC metabolomic content that correlates with breath aerosol size.

Materials and Methods

Exhaled Breath Condensate (EBC) Sampling Hardware

EBC sample collection was achieved using a hand-held human breath sampler described in previous work.[2] Briefly, the outer casing of the device was constructed from polycarbonate tubing and insulated with polyethylene foam. A borosilicate glass tube was used as a condenser surface. Hollow space between the glass condenser tube and insulated housing was filled with dry ice pellets. Computer-aided design (CAD) models of the human breath sampler illustrate these components (**Figure 6**). Three vertical notch filter lengths were experimentally tested with the device at 23, 28, and 33 mm (**Figure 6e)**. An airway chamber contains a pair of asynchronous valves designed to promote unidirectional breath flow and keep the condenser chamber closed for condensation from the ambient air. This device features a saliva trap to

allow selective filtering of breath aerosols by capturing heavy droplets (≳ 100 µm) and allowing small aerosols (≲ 20 µm) which originate in the deep lungs to pass through, and this was demonstrated earlier using an amylase assay.[2] The housing is constructed out of polytetrafluoroethylene (PTFE), a chemically inert material used to reduce chemical absorbance. The mouthpiece used has an inner diameter of 22 mm and is made of polystyrene butadiene (BE 120-22D; Instrument Industries, Inc. Pittsburg PA, USA). Further details on the inner dimensions of the device are annotated in **Supplemental Figure S5**.

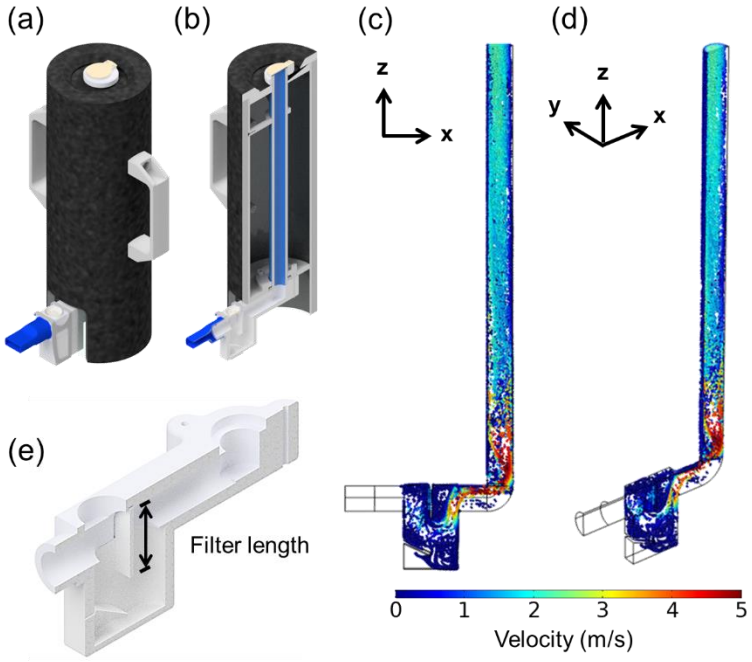

Figure 6. CAD models of the human exhaled breath condensate (EBC) sampler. **(a)** Model of the whole device and **(b)** Sectioned in half. **(c)** A simulation snapshot illustrating the velocity of exhaled aerosols. **(d)** Isometric view of simulation snapshot. **(e)** The vertical notch filter length variable for experiments in this study were 23, 28 and 33 mm.

Simulated Passive Droplet Filtering

Ten notch filter lengths were simulated with the device to calculate the effect of filter length on the breath aerosol size distribution and the proportion of aerosols which make their way through to the EBC collection tube. Additionally, three notch filter lengths were experimentally tested with the device to determine if there are variations of breath metabolomic profiles.

Aerosol particle flight paths inside the Teflon™ housing were estimated with a particle tracing application in COMSOL Multiphysics® simulation software with the assumption that particles were at thermal equilibrium with the carrier fluid and underwent no phase change (no evaporation or condensation) in flight. This is reconciled with a 'freeze' wall boundary condition, so when particles strike a wall they no longer move. Particles pass through the sampling device into a chilled glass tube (-30 ºC), the collection site, and are counted at t_{final} = 0.5 s. The fluid properties at the inlet were approximated with those of saturated moist air mixture at body core temperature (36.6 ºC), taken from previous work and literature. A set of simulations consisted of a uniform distribution of particles with 1000 evenly spaced diameter values in a range of 0.01 to 20 µm to demonstrate what may happen to larger particles that originate from tidal breathing and other breathing activities. Presumably, particles generated in situ and then exhaled are liquid spheres. The principal component of EBC is condensed water vapor which represents nearly all the volume (>99%) of fluid collected in EBC.[52,53] Nonvolatile and water-soluble molecules inside respiratory droplets may increase or decrease the density of these droplets. The density of the droplets also changes as a function of temperature. We assume these alterations are negligible and we assume that the average density of these exhaled breath aerosols to have the density of water (1 g/cm^3, at 4 ºC). The breath aerosols were modeled in these simulations as spheres and with a density of 1 g/cm^3.

The number of exhaled particles per exhalation has been found to vary among subjects by orders of magnitude, ranging widely from 10^2 to 10^5 particles per exhalation. Based on these results, the number of particles released from the inlet is set to an upper estimate of $N_{inlet} = 10^5$ for the simulations. All particles are released with a velocity of 2 m/s at time t = 0 s at 100 different locations the inlet surface. The inlet flow rate corresponds to an average tidal breathing rate (12-20 breaths min^{-1}, tidal volume 0.5 L, exhaled in 1s).[54,55] We assume an initial velocity of 2 m/s to be a generalized value of breath aerosol velocity from tidal breathing in healthy

adults.[56–58] Ten vertical notch filter sizes (0, 3, 8, 13, 18, 23, 28, 33, 38, and 43 mm) were iterated with the same uniform distribution.

EBC Sample Collection

Collection of EBC was performed with the device from one healthy volunteer to standardize the aerosol emission source (male, age 27, no history of smoking). The sampling was time controlled at 10 min with normal tidal breathing. To reduce the effect of food related confounders, the volunteer restrained from food consumption one hour before EBC collection and rinsed the mouth with water prior to sampling. All parts of the device were thoroughly cleaned with 70% ethanol disinfectant spray and deionized (DI) water and air-dried after each use. After sampling, the frozen EBC condensate was removed and transferred to a clean borosilicate glass vial (Sigma-Aldrich, SU860099 SUPELCO), immediately sealed with a stainless-steel threaded cap with PTFE fluorosilicone rubber septum (Sigma-Aldrich, SU860101 SUPELCO) and placed in a laboratory freezer at -80 °C until mass spectrometry analysis. A total of 6 EBC samples were collected, 2 replicates for each filter length tested (23, 28, and 33 mm).

EBC Sample Analysis

EBC samples were directly lyophilized and the obtained dried extract was reconstituted in mobile phase (5% acetonitrile in water) to obtain a concentration factor of 20. Samples were analyzed using an Agilent 1290 series HPLC system coupled with an Agilent 6530 quadrupole - time of flight (qTOF) mass spectrometer (Agilent Technologies, Santa Clara, CA, USA). 20 µL of each sample were injected through an InfinityLab Poroshell 120 EC-C18 column (2.7 µm, 3.0 mm × 50 mm; Agilent Technologies, Palo Alto, CA, USA). The mobile phases consisted of water (A) and acetonitrile (B), both with 0.1% formic acid. The solvent flow rate was set to 0.6 ml min^{-1}, the column temperature to 35 °C and the autosampler to 8 °C to increase sample stability. An electrospray ionization (ESI) source with an Agilent Jet Stream nebulizer was used in positive

and negative mode with the following operating parameters: capillary voltage, 4000(-)/3500(+) V; nebulizer pressure, 25 psi; drying gas, 10 L min^{-1}; gas temperature, 250 °C; fragment voltage, 130 V. Mass spectra were acquired at MS resolution level at a scan rate of 2 spectra/s over a range of m/z 100-950.

Data Processing

The LC-MS data were initially checked for qualitative purposes using Agilent's Mass Hunter Qualitative Analysis B.06.00 software. For the untargeted analysis, data mining was performed using an automated algorithm for peak finding, alignment, and integration in Agilent's Mass Hunter Profinder B.09.00 software. A Bach Recursive Feature Extraction method was used with mass tolerance and window of 20 ppm and 0.025 Da, RT window of 0.3 min, with minimum absolute abundance of 1000 counts. The obtained dataset was exported into a *.pfa* format and imported to Agilent's Mass Profiler Professional (MPP, V13.0) software for identification, and initial statistical analysis. Afterwards, a tentative identification of the obtained molecular features (markers), described as *mass@retention time*, was performed using ID browser, an integrated software in MPP. Based on matching experimental and theoretical isotope pattern of the markers, the software proposed formulas and names with scores above 70%, using the METLIN database. The dataset was filtered by removing compounds that appear in blank samples with signals higher than 10 (peak sample/blank ratio). Final data were normalized using probabilistic quotient normalization with median values per sample to correct the bias between sample collection and preparation.[32]

Results and Discussion

Simulated Passive Droplet Filtering

Figure 7 shows the numerical solutions for breath aerosols with different diameters passing through the device. The data were grouped into 25 evenly distributed bins. The absence of a notch filter (designated as length 0 mm) corresponds to nearly 5.5% of particles trapped which

are greater than 10 µm in diameter. The trapping of larger particles increases with a greater length of the notch filter, which supports our first hypothesis. Notch filter lengths of 18, 23, 28, 33, and 38 all appear to have the same effect on the particle size distribution, all correlating to an averaged 43.5% trapping of particles, mostly larger than 10 µm in diameter. Increasing the notch length from 13 to 18 mm as well as from 38 to 43 mm appear to have much greater changes on the resulting particle size distribution in the collection tube. A notch length of 43 mm corresponds to nearly 70.8% of particles trapped, mostly larger than 5 µm in diameter. The percentage of particles trapped is defined to be the number of breath aerosols which pass through to the chilled glass tube divided by the total particles in the device, multiplied by one hundred. These counts of particles which made it to the collection tube compared to the ones remaining at the trapping site are plotted (**Figure 7b**).

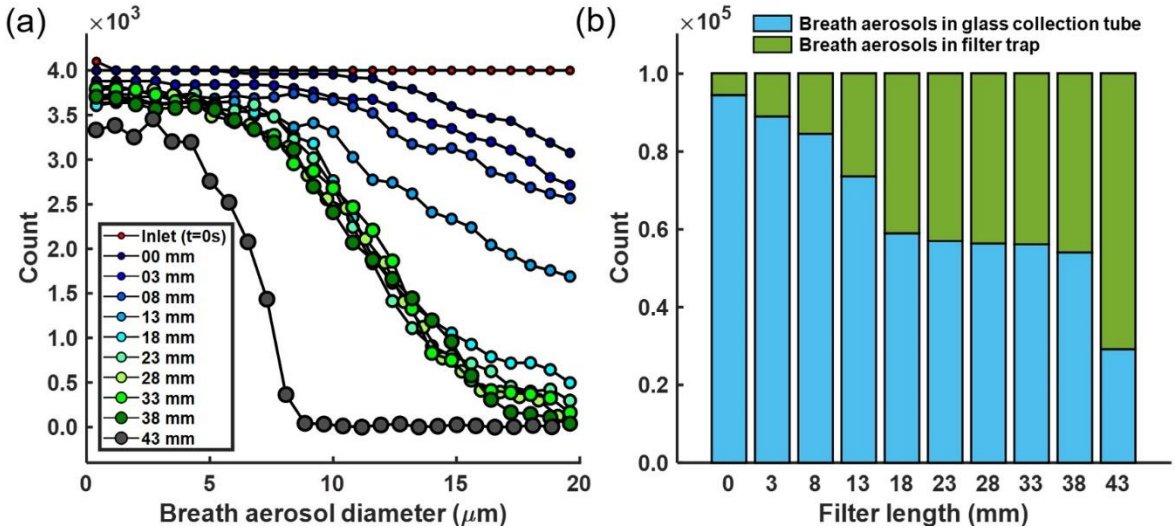

Figure 7. COMSOL Multiphysics® software simulations of breath aerosol particles which passed through the exhaled breath condensate (EBC) sampling device into a chilled glass tube, the collection site at time t_{final} = 0.5 s. Ten vertical notch filters were iterated. **(a)** A uniform diameter distribution of particulates enters the inlet with 1000 evenly spaced values in a range of 0.01 to 20 µm at 100 different locations. Data are grouped together into 25 evenly distributed bins. **(b)** Total count of breath aerosols which pass through to the chilled glass tube compared to the count of these aerosol particles trapped in a reservoir by the filter.

The velocity profiles are modeled in steady state of the sampling device (**Supplemental Figure S6**). It is evident the notch filter length has a direct impact on the velocity flow profile of

Table 3. The list of highest abundant metabolites (highest to lowest) putatively identified by untargeted liquid chromatography-mass spectrometry (LC-MS) analysis among all exhaled breath condensate (EBC) samples.

Variable number	Mass (m/z)	RT (min)	Formula	Compound Name	ID Scores	Description
1	199.200	4.11	C12 H24 O2	3-Methyl-undecanoic acid	73.35	Fatty acid
2	324.200	4.70	C18 H28 O5	Cibaric acid	80.21	Fatty acid
3	266.162	8.64	C12 H27 O4 P	Tributyl phosphate	94.70	Extractant and a plasticizer
4	326.200	2.31	C14 H28 N6 O4	Arg Gly Ile	94.34	Amino acid
5	282.200	2.09	C19 H28 N O3	Glycopyrrolate	94.92	Anticholinergic
6	238.100	1.80	C9 H18 O7	(x)-1,2-Propanediol 1-O-b-D-glucopyranoside	84.95	Found in herbs and spices
7	370.200	2.49	C20 H28 N4 O4	Ile Ala Trp	94.19	Amino acid
8	294.190	7.16	C16 H28 N2 O4	Oseltamivir	95.60	Antiviral
9	255.300	7.38	C17 H36 O	14-Methyl-1-hexadecanol	89.69	Fatty alcohol
10	206.200	3.74	C15 H28 O	7-Ethyl-4-tridecen-6-one	75.48	–
11	209.100	2.82	C13 H11 N3	Proflavine	74.70	Disinfectant
12	452.300	3.06	C29 H42 O5	(3beta,17alpha,23S)-17,23-Epoxy-3,29-dihydroxy-27-norlanosta-7,9(11)-diene-15,24-dione	91.75	Oxosteroid
13	154.100	3.00	C9 H14 O2	Allyl hexenoate	77.28	Flavouring ingredient
14	211.100	3.00	C14 H13 N O	2-Hydroxyiminodibenzyl	86.16	Aromatic compound
15	424.300	4.94	C21 H45 O6 P	1-Octadecyl Lysophosphatidic Acid	94.17	Glycerophospholipid
16	422.300	6.62	C25 H45 O4 P	Dolichyl phosphate	92.93	Lipid
17	310.200	4.34	C20 H26 N2 O	Astrocasine	82.05	Alkaloid
18	540.400	6.51	C30 H59 N O7 P	PC(22:2(13Z,16Z)/0:0)	95.73	Lecithin
19	193.100	3.00	C6 H15 N5 O2	NG-amino-L-Arginine	85.72	Inhibitor of nitric oxide synthase
20	286.100	2.53	C12 H17 N O7	3-Hydroxy-N-methylpyridinium glucuronide	87.09	O-glucuronide
21	546.300	3.02	C29 H59 N O7 P	PC(O-18:0/3:1(2E))[S]	94.04	–
22	557.400	6.51	C37 H48 O3	1?,25-dihydroxy-25,25-diphenyl-26,27-dinorvitamin D3 / 1?,25-dihydroxy-25,25-diphenyl-26,27-dinorcholecalciferol	95.82	Secosteroid
23	366.300	4.37	C26 H40 O2	26:6(8Z,11Z,14Z,17Z,20Z,23Z)	91.13	Omega-3 fatty acid
24	590.400	3.13	C31 H59 O8 P	PA(13:0/15:1(9Z))	88.52	–
25	222.100	2.63	C11 H14 N2 O3	Phe Gly	83.07	Dipeptide
26	138.000	0.59	C3 H8 O5 S	(R)-2,3-Dihydroxypropane-1-sulfonate	72.20	Alkanesulfonic acid
27	187.127	2.84	C9 H19 N O4	Dexpanthenol	95.19	Cholinergic agent
28	348.200	2.31	C18 H32 O6	2,3-dinor Thromboxane B1	74.19	Eicosanoid
29	108.100	2.99	C6 H14	hexane	77.14	Neutotoxin
30	229.200	4.53	C13 H27 N O2	2-amino-tridecanoic acid	91.43	–
31	288.100	8.64	C13 H21 O3 P S	Iprobenfos	91.66	Rice fungicide
32	298.170	8.63	C12 H24 N6 O4	Ala Arg Ala	71.12	Amino acid
33	148.000	6.91	C4 H7 O5 P	Deamino-?-keto-demethylphosphinothricin	80.02	–
34	90.033	0.57	C3 H8 O4	2,2-Dihydroperoxypropane	99.37	Added to foods as a bleaching agent
35	656.500	8.02	C36 H71 N2 O7 P	PE-Cer(d16:2(4E,6E)/18:0(2OH))	75.35	–
36	243.185	5.12	C13 H26 N O4	L-Hexanoylcarnitine	90.85	Human metabolite
37	250.200	3.95	C15 H26 N2 O	Retamine	88.54	Pain reliever
38	156.001	4.85	C7 H5 Cl O2	4-Chlorobenzoate	97.77	Bacterial xenobiotic metabolite
39	250.160	11.69	C14 H22 N2 O2	Rivastigmine	96.64	Acetylcholinesterase inhibitor
40	293.200	4.34	C17 H27 N O3	Pramoxine	87.47	Topical medication to relieve pain
41	651.400	3.22	C32 H62 N O10 P	PS(12:0/14:0)	82.23	–
42	517.400	5.04	C35 H53 N O3	dl-alpha-Tocopherol nicotinate	91.39	Ester of vitamin E
43	176.000	6.91	C5 H11 N3 O4	O-Ureidohomoserine	88.48	–
44	673.500	8.02	C38 H71 N O8	GlcCer(d14:2(4E,6E)/18:0)	91.92	–
45	208.100	2.03	C9 H14 N4 O3	Carnosine	87.13	Synthesized *in vivo*
46	731.500	8.77	C40 H81 N2 O7 P	PE-Cer(d14:1(4E)/24:0(2OH))	89.71	Lipid
47	310.185	9.73	C16 H31 Cl O	2-chloropalmitaldehyde	80.31	Lipid
48	222.200	2.50	C15 H28 O2	2,5-dimethyl-2E-tridecenoic acid	91.22	Fatty acid
49	340.200	3.76	C17 H28 N2 O5	Perindoprilat	72.99	ACE inhibitor
50	610.356	7.16	C31 H52 N2 O5 S	Valnemulin	92.42	Pleuomutilin antibiotic

the breath aerosols. The ambient pressure of the device was set to 1 atm and the resulting pressure profiles inside the device for each simulation (**Supplemental Figure S7**). Mols et al. concluded that a pressure drop of 950 Pa across an endotracheal tube resulted in excessive tidal volumes and airflow, which was perceived as discomfort.[59] A notch filter length of 43 mm could cause respiratory discomfort with a pressure difference of ~140 Pa which may depend upon one's health condition.

Table 4. The number of common compounds found from exhaled breath condensate samples using different vertical notch filter lengths. The table lists the number of compounds common for filter length combinations in liquid chromatography-mass spectrometry (LC-MS) negative and positive electrospray ionization modes.

	LC-MS ESI negative mode count	LC-MS ESI positive mode count	LC-MS ESI total count
Total	744	5481	6225
Common all filters	458	3439	3897
Common in 2 filters	148	1111	1259
Unique	68	575	643
23 and 28 mm	113	540	653
23 and 33 mm	35	336	371
28 and 33 mm	0	235	235
23 mm	29	179	208
28 mm	39	396	435
33 mm	0	0	0

Metabolomic Content of the EBC

A total of 6,225 metabolites were obtained from the LC-MS chromatograms in negative and positive ionization modes. Data were previously aligned and filtered, as described below. Metabolite identification of untargeted data were performed based on the MS and MS/MS spectra and the accurate masses obtained using METLIN database. The putatively identified biomarkers are listed with their exact molecular mass and retention time (**Table 3**). It lists the 50 highest abundant metabolites (highest to lowest) detected by untargeted LC-MS analysis among all six EBC samples. Molecular formula and compound identification are described together with their identification (ID) score, calculated with the average values from molecular formula extraction and database ID scores.

The number of common compounds found from exhaled breath condensate samples using different vertical notch filter lengths are listed (**Table 4**)**. Table 4** lists the number of compounds common for filter length combinations in LC-MS negative and positive electrospray ionization modes. Most compounds were present in all EBC samples collected from the device using each filter length. Compounds were considered unique to a filter length if they were present in at least one of the two replicate samples per filter length. Approximately 11% of compounds were unique to a filter length, both for negative and positive ionization modes. The notch filter with length 28 mm had a higher number of unique compounds in both negative and positive ionization modes in comparison to the 23 mm notch filter. The notch filter with length 33 mm had no unique compounds in either ionization mode. A higher number of compounds were present in both 23 and 28 mm filter lengths in comparison to the two other sets (23/33 and 28/33 mm). We do not believe these differences can be determined as statistically significant given the samples were from only one person and the extremely limited sample numbers involved (n=6 total). We do not observe striking data at this time that breath aerosol size affects metabolite profiles.

Conclusion

Our human exhaled breath condensate sampler described was modified with varying notch filter lengths to determine if breath aerosol size affects EBC metabolite content. From simulation results, particles typically larger than 10 µm were filtered out for notches longer than 18 mm. This indicates that a longer notch filter in this device prevents larger particles from reaching the collection tube thus altering the aerosol particle size distribution. Three notch lengths were experimentally tested with the sampling device. Most compounds were commonly present in all three filter lengths, and we did not see strong statistical evidence of systematic metabolite differences between breath aerosol size distributions. If there are differences in metabolomic content based on breath aerosol size, it is possible that they are not significant for practical

sampling if the sampling device design has already been optimized for proper saliva filtering, cooling temperature, and air flow rates.

Acknowledgements

This study was supported by: NIH award U01 EB0220003-01 [CED, NJK]; the NIH award UL1 TR000002 [CED, NJK]; NIH award 1P30ES023513-01A1 [CED, NJK]; and NIH award UG3-OD023365 [CED, NJK]. Student support was provided by the National Center for Advancing Translational Sciences, National Institutes of Health, through grant number UL1 TR001860 and linked award TL1 TR001861. The content is solely the responsibility of the authors and does not necessarily represent the official views of the funding agencies. The authors also gratefully acknowledge Dr. Konstantin Zamuruyev (NASA Jet Propulsion Laboratory) for technical discussions.

Supplemental Information

This pilot study simulates the trajectories of breath aerosols in a hand-held human exhaled breath condensate (EBC) sampler device. Ten notch filter lengths were simulated with the device to calculate the effect of a filter length on the breath aerosol size distribution and the proportion of aerosols which make their way through to the EBC collection tube. We used COMSOL Multiphysics® Particle Tracing Module software to simulate the trajectories of these aerosols. This document provides supplemental details of the simulation methods used in this study.

Mesh Generation

The 'Free Tetrahedral' feature was used to create a mostly tetrahedral mesh or in other words, to enable the discretization of the geometry into small units of simple shapes. The Delaunay tessellation method was used to modify the mesh in the boundary regions for simplification. The predefined mesh element size was set to 'Coarse'. The mesh has 1.48×10^5 number of elements with 4.88×10^4 vertices, consisting of the following proportions of element shapes: tetrahedra (55.9%), prisms (32.7%), triangles (9.39%), quadrilaterals (1.76%), hexahedra (0.18%) and pyramids (0.07%).

Particle Tracing for Fluid Flow

The COMSOL Multiphysics® Particle Tracing Module is used as a flexible tool to compute the trajectories of particles. The Particle Tracing Module uses a Lagrangian method to solve ordinary differential equations using Newton's law of motion. The default Newtonian formulation was used to solve second order equations for particle positions.

A Constant (Newton) nonlinear method was used to control the damping factor used in the damped Newton iterations. The damping factor was set to the default value 1. This time-dependent solver had a Jacobian update once per time step, which computes a new Jacobian on the first iteration of each time step. The 'Tolerance' termination technique was used to

terminate the Newton iterations when the estimated relative error is smaller than a specified tolerance. The absolute tolerance was set to 10^{-6}.

For COMSOL Multiphysics'® particle tracing approach to be valid, the volume fraction of the particles must be much smaller than the volume fraction of the continuous phase, generally less than 1%. When the volume fraction of particles is not small, the fluid system is categorized as a dense flow and a different modeling approach is required. The volume fraction of the particles (with an average diameter of 10 μm) in the device is estimated to be:

$$\frac{N_{particle}}{V_{device}} \cdot \bar{V}_{per\ particle} = \frac{10^5\ \text{particles}}{62.5\ \text{cm}^3} \cdot 5.236 \times 10^{-10}\ \frac{\text{cm}^3}{\text{particle}} = 8.38 \times 10^{-7} \ll 0.01$$

which is far less than 1% and thus the particle tracing approach is valid for particle deposition predictions. $N_{particle}$ is the total number of particles in the device. V_{device} is the volume of the device and $\bar{V}_{per\ particle}$ is the average volume of the particles.

The initial particle deposition setting was set to 'Density' which particles are positioned in at the inlet surface by sampling from a user-defined spatial distribution. This user-defined spatial distribution, 'Number of particles per release' N (dimensionless), was set to 100. In other words, particles were released at 100 different positions at the inlet at time t = 0s. The 'Release distribution accuracy order' was set to the default value 5, which determines the integration order that is used when computing the number of particles to release within each mesh element. The higher the order, the more accurately particles will be distributed among the mesh elements. The 'position refinement factor' was set to the default value 0, which assigns each particle with a unique position. The initial distribution of the particles' positions ranges from the center of the device's duct and can be as close as approximately 0.5 mm away from the wall of the device.

The generalized minimum residual (GMRES) iterative solver was used to solve the general linear system of the form $Ax = b$. COMSOL Multiphysics® estimates the error of the solution while solving. Once the error is small enough, as determined by the convergence criterion:

$$\rho|M^{-1}(b - Ax) < tol \cdot |M^{-1}b|$$

the software terminates the computations and returns a solution. Left-preconditioning was used with the GMRES solver and M is designated as the preconditioner matrix. The residual tolerance value was set to 0.01.

The 'Generalized alpha' time stepping implicit time-dependent solver algorithm was used for tracking particles in the simulation. Generalized alpha is an implicit, second-order accurate method with a parameter α to control the damping of high frequencies. With α = 1, the method has no numerical damping and α = 0 gives the maximum numerical damping. The amplification of high frequency α value was set to 0.75.

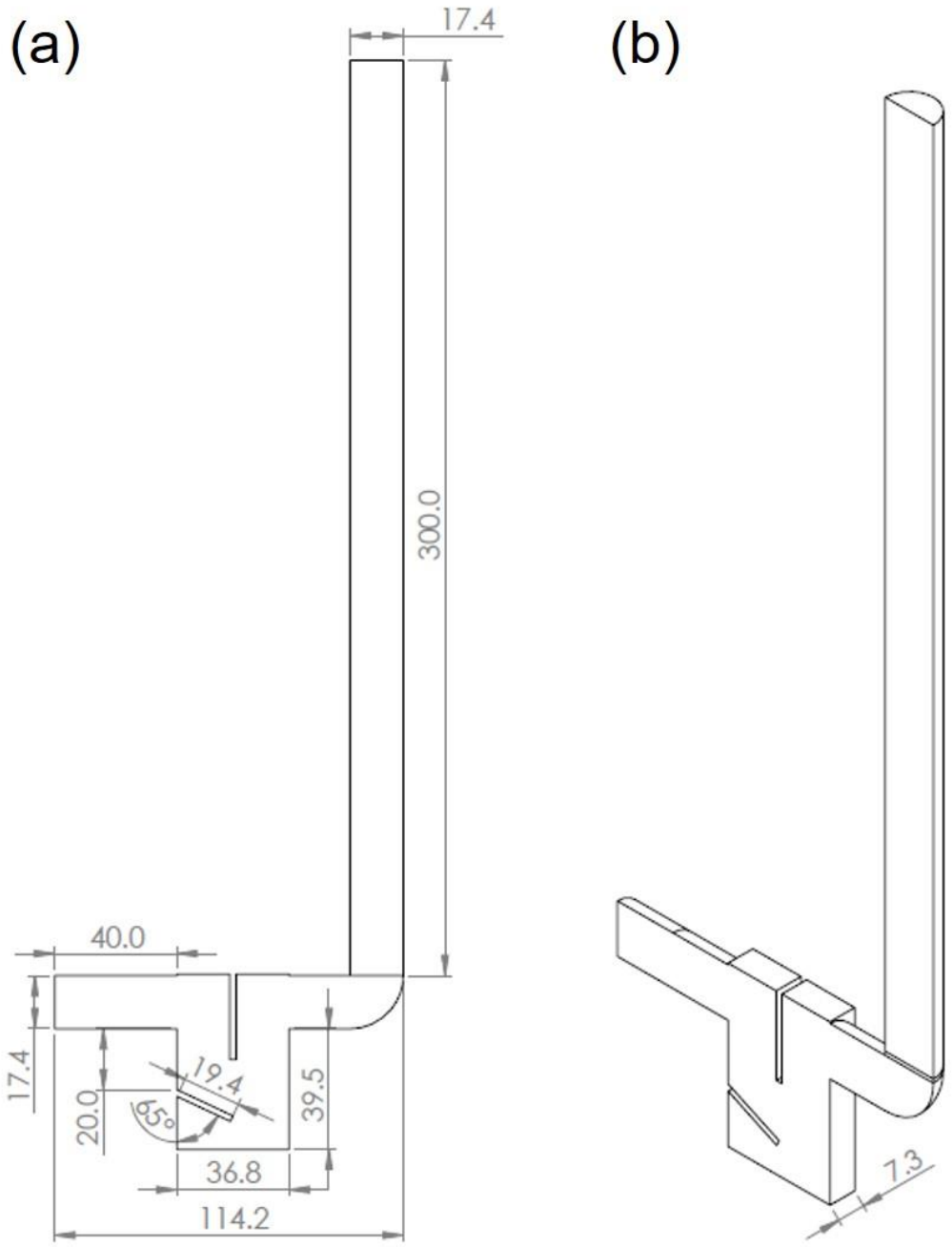

Supplemental Figure S5. CAD model and details of the inner dimensions of the human exhaled breath condensate (EBC) sampler used in passive droplet filtering COMSOL Multiphysics® simulations. All dimensions are in millimeters unless otherwise noted. (**a**) Model of the device, sectioned in half. (**b**) Isometric view of the model.

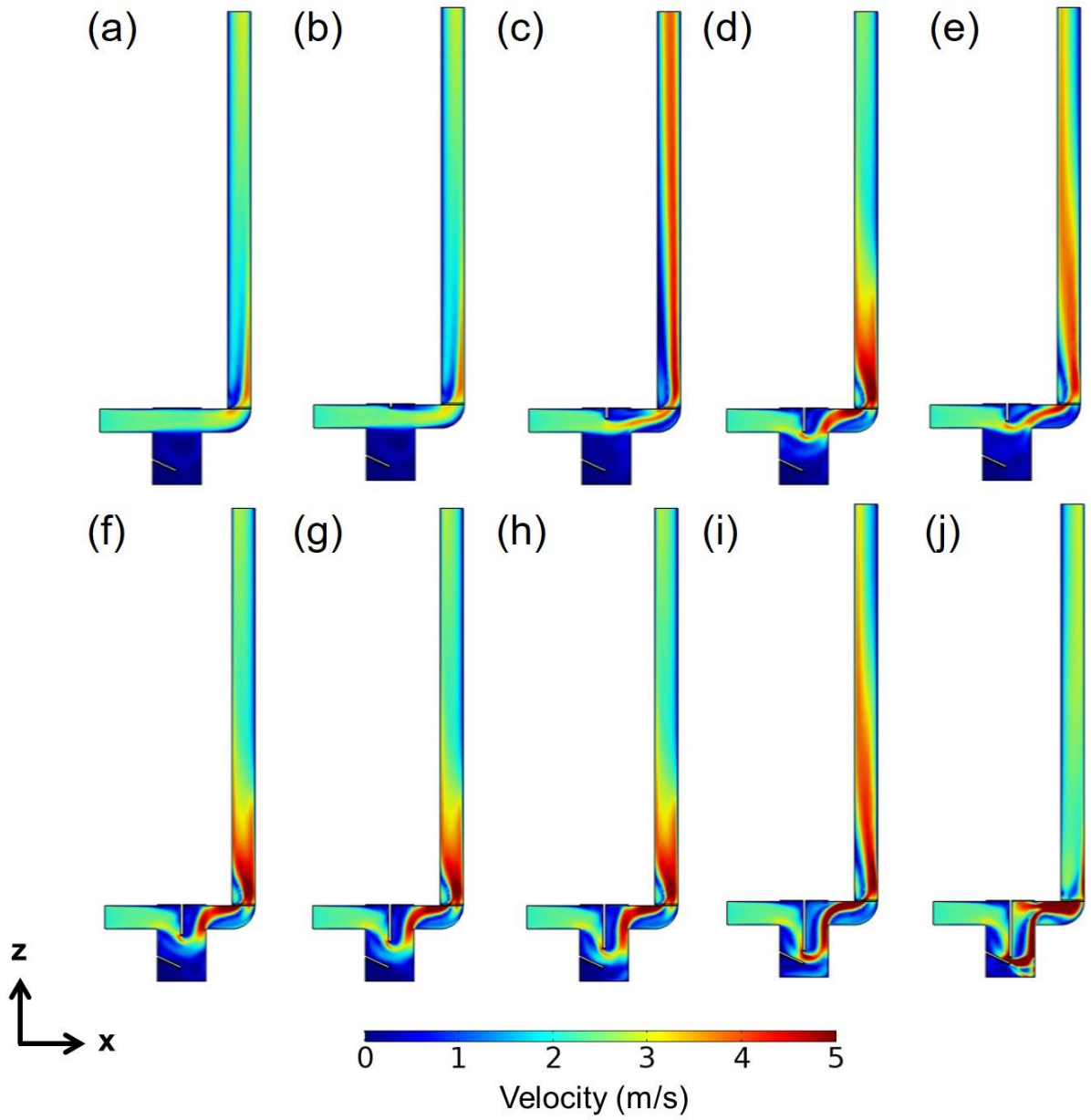

Supplemental Figure S6. Steady state velocity profiles of the exhaled breath condensate sampling device using COMSOL Multiphysics® simulation software. Ten filter lengths were simulated: **(a)** 0 mm **(b)** 3 mm **(c)** 8 mm **(d)** 13 mm **(e)** 18 mm **(f)** 23 mm **(g)** 28 mm **(h)** 33 mm **(i)** 38 mm **(j)** 43 mm.

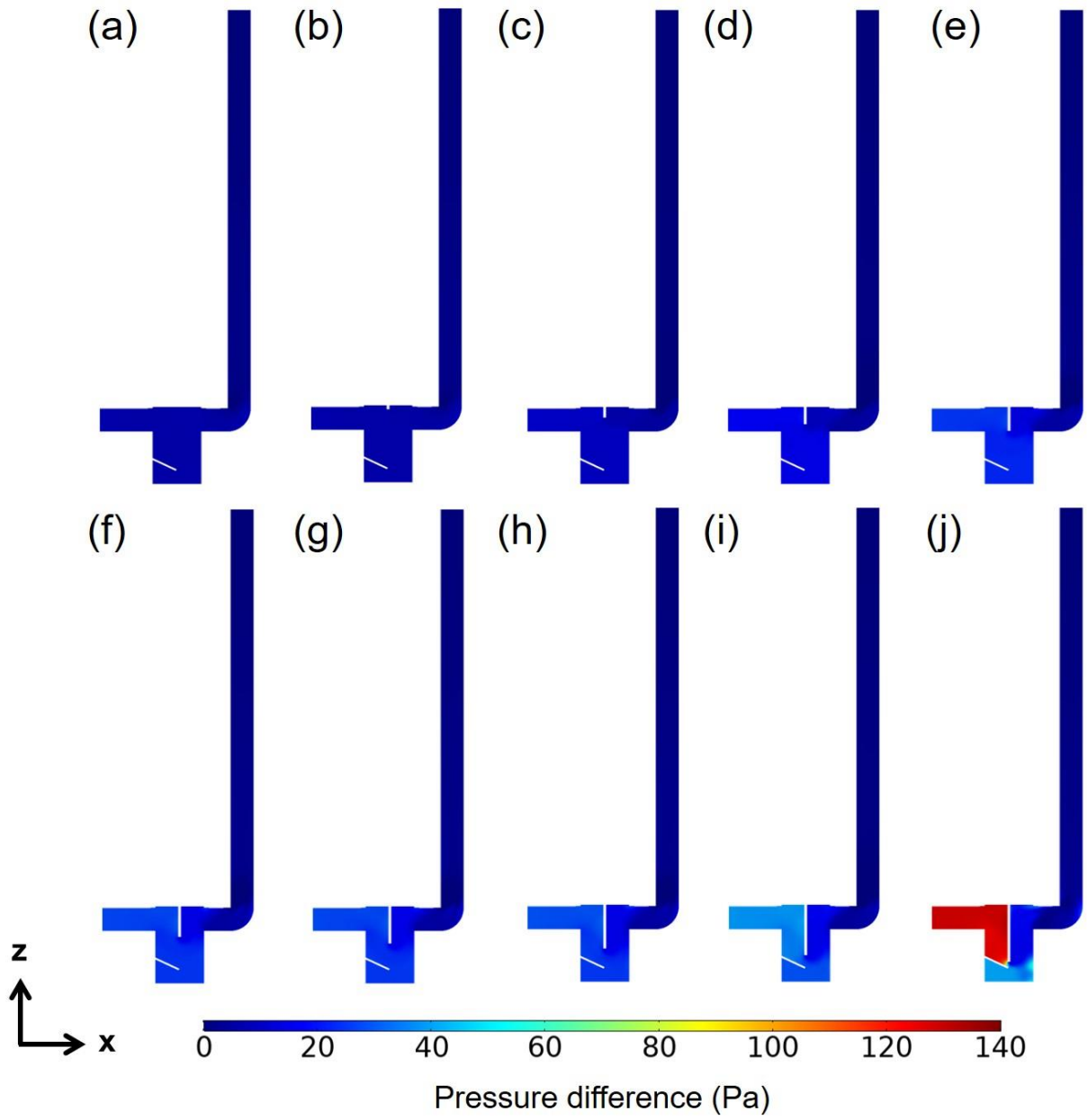

Supplemental Figure S7. Steady state pressure profiles of the exhaled breath condensate sampling device using COMSOL Multiphysics® simulation software. Ten filter lengths were simulated: **(a)** 0 mm **(b)** 3 mm **(c)** 8 mm **(d)** 13 mm **(e)** 18 mm **(f)** 23 mm **(g)** 28 mm **(h)** 33 mm **(i)** 38 mm **(j)** 43 mm.

Chapter 4: Stable Electrospray Signal on a Microfabricated Glass Chip with Three-Dimensional Open Edge and Tiered Depth Geometries

Alexander J. Schmidt, Konstantin O. Zamuruyev, Michael K. LeVasseur, Stephanie Fung, Ilya M. Anishchenko, Nicholas J. Kenyon, Cristina E. Davis

Authorship contributions

Alexander J. Schmidt: Conceptualization, device and electronics design and testing, experiment planning, experimental data, review of data and results, writing original draft, writing review, and editing. **Konstantin O. Zamuruyev**: Conceptualization, microfabrication, device design and testing, review of data and results, writing review, and editing. **Michael K. LeVasseur:** electronics design and fabrication, writing review, and editing. **Stephanie Fung:** electronics design and fabrication, writing review, and editing. **Ilya M. Anishchenko:** device testing. **Nicholas J. Kenyon:** Conceptualization, funding, mentoring, supervision, writing review and editing. **Cristina E. Davis:** Conceptualization, experiment planning, review of data and results, funding, mentoring, supervision, writing original draft, writing review and editing.

Abstract

This paper presents the microfabrication and performance of a three-dimensional electrospray ionization (ESI) emitter tip made from glass. Our fabrication process relies on standard microfabrication techniques (i.e., deposition, photolithography, and wet etching). This fabrication method involves the novel application of two layers of positive and negative photoresists in addition to Parafilm® wax tape. Open edge and tiered depth details were successfully created from a multilayer planar mask. This is a benefit for integrated miniaturized and microfluidic systems that often require micro features for their functionality but relatively large millimeter size features for their physical periphery. We demonstrate the fundamental performance of electrospray with this microfluidic chip. The emitter tip was fixed on a linear axis stage with high resolution (10 µm) to finely control the tip distance from a metal counter electrode plate. A custom printed circuit board system was built to safely control four voltages applied to the

microchip ports from a single high voltage power supply. To readily form the electrospray, non-aqueous solvents were used for their low viscosity and a constant voltage of +2.7 kV was applied to the sheath electrospray microchannel. The liquid being sprayed was 80/20 (v/v) methanol/acetonitrile with 0.1% acetic acid in the sheath microchannel and with ammonium acetate (10-40 mM) in its remaining microchannels. The electrospray signal was measured in response to varying the distance (1.4 to 1.6 mm) between the electrospray emitter tip and a metal counter electrode plate in addition to the varying concentration of the background electrolyte, ammonium acetate. Stable and repeatable electrospray signal showed linear relationships with emitter tip distance and concentration ($r^2 \geq 0.95$).

Definitions of Abbreviations:

buffer inlet (BI); computer aided design (CAD); chromium (Cr); deionized water (DI water); light emitting diode (LED); printed circuit board (PCB); polydimethylsiloxane (PDMS); mixture of H_2SO_4:H_2O_2 at 4:1 ratio (Piranha); polylactic acid (PLA); polymethylmethacrylate (PMMA); platinum (Pt); standard cubic centimeters per minute (sccm); scanning electron microscope (SEM); sample inlet (SI); sheath liquid inlet (SLI); sample outlet (SO); single pole triple throw (SP3T)

Introduction

Electrospray Ionization (ESI) is a prevalent technique for liquid chemical detection in analytical chemistry.[4] ESI generates a fine liquid aerosol through electrostatic charging. A high electric potential (typically ± 2–5 kV) is applied between the end of a capillary and a counter electrode installed in proximity (typically 1–2 mm). Tiny micro–droplets tear away from the surface of a liquid Taylor cone searching for a surface to land. Due to liquid solvent evaporation and charge preservation, an emitted droplet undergoes a series of Coulomb explosions to reduce its electric repulsion between charges and achieves a charge limit corresponding to that of an ion.[60] In this way, ions contained in a liquid phase sample are transferred into a gas phase. These ions land

on a counter electrode plate which can then be detected amperometrically. ESI operations are best performed in the stable cone jet mode when ESI current is most reproducible. The ability to achieve stable and effective spray depends on the applied voltage, the distance between the spray tip to the counter electrode, and the viscosity.[61] Electrospray is stable when a cone can be observed with a steady stream of droplets issued from it and when there is steady current in the external electrical circuit.

This paper presents the microfabrication and performance of a novel three-dimensional electrospray ionization (ESI) emitter tip made from glass. Only recently have three approaches been proposed for the fabrication of monolithically integrated ESI microfluidic chips from glass.[62–64] Hoffmann et al. integrated a manually pulled ESI tip onto a commercial microchip. Another approach, by Mellors et al., created an ESI tip by sawing a corner at the end of a microchannel with a dicing saw. These two methods either rely on low-throughput manual-pulling or harsh mechanical machining to make their glass ESI tips. Sainiemi et al. present parallel microfabrication of three-dimensional ESI glass emitters that are also monolithically integrated with microfluidic channels. This approach can replace commercial electrospray needles by providing equally robust emitter tip performance. Further studies have since implemented these three techniques.[65–72] In addition to the work presented by Sainiemi et al., our fabrication process only relies on standard microfabrication techniques (i.e., deposition, photolithography, and wet etching). We address the needs of integration of an electrospray emitter tip by considering the combination of meso- and micro-features, open edged features, and the possibility of microfabrication on a wafer scale. Our fabrication method involves the novel application of two layers of positive and negative photoresists in addition to Parafilm® wax tape. We also use isotropic wet etching of glass in hydrofluoric acid (HF) solution and chromium (Cr) deposition. This approach creates a three-dimensional ESI tip with accurate and high quality small-scaled geometric features. This allows for higher charge densities leading to increased ionization efficiency for better signal stability and repeatability. Open edge and tiered

depth details were successfully created from a multilayer planar mask. This is a benefit for integrated microfluidic systems that often require micro features for their functionality but large millimeter size features for their physical periphery. Dimensional control during isotropic etching is susceptible to undercutting although the etching process is beneficial when fabricating three-dimensional structures. As glass under the emitter tip is removed, a sharpened curved profile is formed.

Glass is an important material of choice for analytical and medical field applications due to its excellent material and chemical properties (i.e., mechanical strength, chemical inertness, optical transparency, and native hydrophilicity). ESI tips can be easily realized with well-established silicon microfabrication protocols, although silicon is electrically conductive and thus prevents its integration with chemical separation methods (e.g., chromatography or capillary electrophoresis) which require high voltages for operation. Polymer microfabrication also offers monolithic integration of ESI tips (SU-8 photolithography[73,74], PMMA[75], PDMS[76], polyimide[77], and thiol-ene.[78,79] However, polymers can suffer from swelling or degradation by organic solvents.[80,81]

We demonstrate the fundamental performance of electrospray with our glass microfluidic chip. This device allows efficient ionization without the use of external pressure sources. The emitter tip was fixed on a linear axis stage with high resolution (10 μm) to finely control the tip's distance from a metal counter electrode plate. A printed circuit board system was custom built to safely control four voltages applied to the microchip's four ports from a single high voltage power supply. To readily form the electrospray, non-aqueous solvents were used for their low viscosity and a constant voltage of +2.7 kV was applied to the sheath electrospray microchannel. The liquid being sprayed was 80/20 (v/v) methanol/acetonitrile with 0.1% acetic acid in the sheath microchannel and with ammonium acetate (10-40 mM) in its remaining straight cross microchannels. The electrospray signal was measured in response to varying the distance (1.4 to 1.6 mm) between the electrospray emitter tip and a metal counter electrode

plate in addition to the varying concentration of the background electrolyte, ammonium acetate. Stable and repeatable electrospray signal showed linear relationships with emitter tip distance and concentration ($r^2 \geq 0.95$).

Chemicals and Reagents

Acetic acid, ammonium acetate, and methanol were purchased from Sigma-Aldrich (Steinheim, Germany). Acetonitrile was purchased from Fisher Scientific (Pittsburg, PA). All chemicals and reagents were of analytical or HPLC grade. Water was purified with a Elga Purelab Classic DI Water System (Woodridge, IL). Before use, all sample and buffer solutions were filtered (0.22 µm) and degassed by sonication for 5 min.

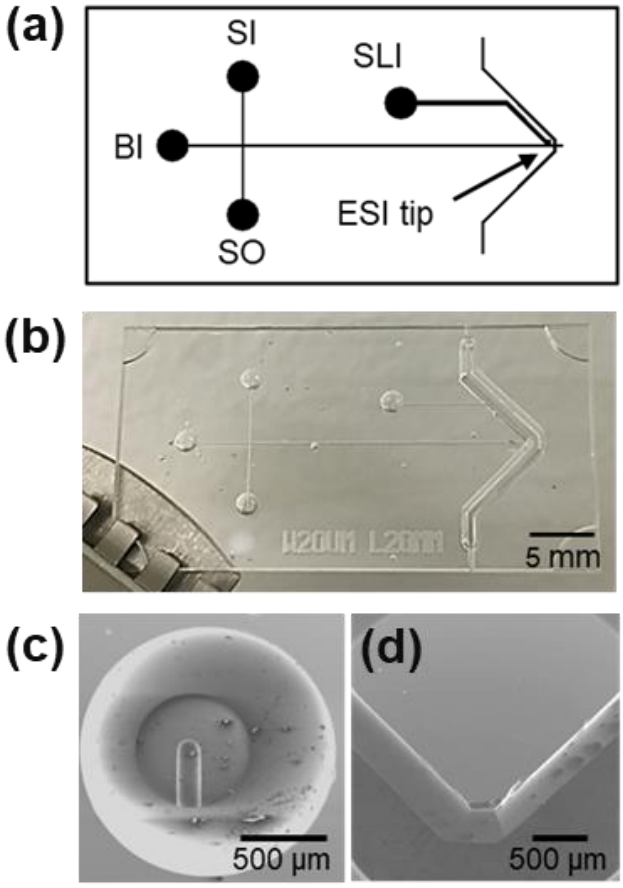

Figure 8. (a) Schematic of the microfluidic chip layout. SI: sample inlet, SO: sample outlet, BI: buffer inlet, SLI: sheath liquid inlet. **(b)** Photograph of the microfluidic chip with an integrated electrospray emitter tip, held by a tweezer. **(c)** Scanning electron microscope (SEM) image of drill-free reservoir port. **(d)** SEM image of the ESI emitter tip.

Materials and Methods

The microfluidic glass chip has a monolithically integrated three-dimensional ESI emitter tip. A schematic and a photograph of the microfluidic chip are presented (**Figures 8a, b**). The overall length and width of the microfluidic chip are 34 and 18 mm, respectively. The buffer microchannel (buffer inlet to ESI tip) has a length of 25 mm, a depth of 100 µm, and a width of 20 µm. The sample loading microchannel (sample inlet to sample outlet) has a length of 10 mm, a depth of 100 µm, and a width of 20 µm. The sheath liquid inlet microchannel has a length of 10.8 mm, a depth of 100 µm, and a width of 200 µm. The sheath liquid microchannel offers the possibility to apply a voltage for ESI and functions as a buffer zone, which means the buffer inlet microchannel is not affected by the nebulized flow. The access ports have a diameter of 1.5 mm, one of which is shown in a scanning electron microscope (SEM, FEI Scios DualBeam) image (**Figure 8c**). The bottom side cavities were etched to a depth of 560 µm which set the tip thickness and to form an open edge. The top side etch cavities were etched to a depth of 110 µm to further define the tip edge. An SEM image of the ESI emitter tip is shown (**Figure 8d**).

The microfluidic chip was fabricated in a class-100 cleanroom facility (Center for Nano and Micro Manufacturing, UC Davis, CA). Standard microfabrication procedures (i.e., photolithography, wet etching, and deposition) were used with Borofloat® glass, purchased from S.I. Howard Glass Co., Inc. (Worchester, MA, USA). In summary, the microchip consists of two halves: access ports and microchannels; both halves contain a part of the ESI tip. The top side of a wafer is defined to be the side that looks up when holding by the orientation of physical placement of the microchip. The bottom side of the wafer is defined to be its opposite side. The prepared glass halves were etched in 49% HF acid from both sides sequentially in order to create three-dimensional features. The chips were cleaned, and the two halves were bonded in thermal fusion. The wafers were then diced into individual chips after thermal fusion bonding. The manufacturer recommended and standard recipes were followed for microfabrication. A summarized illustration of the microfabrication process is presented (**Figure 9).**

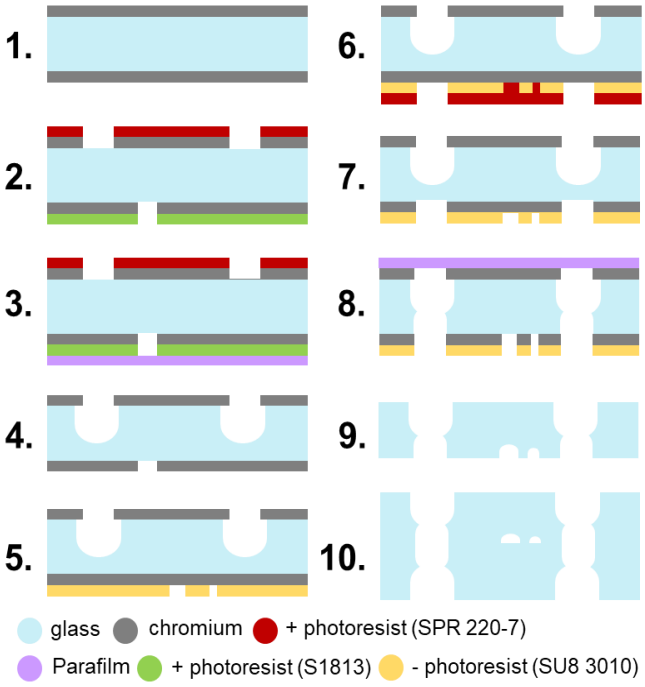

Figure 9. Summary and illustration of the microfabrication process. **1.** Start with new glass wafer and sputter chromium (Cr) both sides. **2.** Apply SPR 220-7 on top side, S1813 on bottom side. UV exposure to define ESI tip edge on top side. UV exposure to define alignment marks on bottom side. Develop both sides. Etch Cr both sides. **3.** Apply Parafilm® tape on bottom side. **4.** Etch glass in HF and remove both photoresists and Parafilm® tape. **5.** Apply SU8 3010 on bottom side. UV exposure to define microchannels on bottom side. Develop SU8 3010 on bottom side. **6.** Apply SPR 220-7 on bottom side. UV exposure to define ESI tip and alignment marks (not shown) on bottom side. Develop SPR 220-7. **7.** Etch Cr and etch glass in HF. Remove SPR 220-7. **8.** Etch Cr and etch glass in HF with Parafilm® applied on bottom side. **9.** Remove SU8 3010 and Parafilm®. Etch Cr both sides. **10.** Surface plasma activation and thermal fusion bonding of the access ports wafer and the microchannels wafer.

The microfabrication process started with two clean wafers that were sputtered with 200 nm of chromium each on both sides (CHA Industries AutoTech II, Fremont, CA)**.** The following steps apply to the access port wafer's top side and the microchannel wafer's bottom side. Images of the wafers during the fabrication process are provided (**Supplemental Figure S8**). Adhesion promoter hexamethyldisilazane (HMDS, Avantor Performance Materials, Inc., Center Valley, PA) was spin-coated and then with SPR 220-7.0 photoresist (Dow Electronic Materials MEGAPOSIT, Malborough, MA) to have a thickness of approximately 10 µm. The following steps apply to the access port wafer's bottom side and the microchannel wafer's top side. S1813 photoresist (Shipley, Malborough, MA) was spin-coated to have a thickness of

approximately 2 μm. The access port wafer's top side and the microchannel wafer's bottom side were exposed to ultraviolet (UV) light at 250 mJ/cm^2 in hard contact mode (Karl Suss, MA4, Garching, Germany). The access port wafer's bottom side and the microchannel wafer top side were exposed to UV light at 150 mJ/cm^2 in hard contact mode. Both wafers were then developed in Microposit MF CD-26 aqueous developer (Dow Electronic Materials, Malborough, MA). The wafers were then hard baked in a vacuum oven at 155 ºC for 90 min. Afterwards, both wafers were placed into a chromium etch bath (Transene Chromium Etchant 1020, Danvers, MA) for 1 min. Parafilm® tape (Bemis, Sheboygan Falls, WI) was applied to the access port wafer's bottom side and the microchannel wafer's top side. With separate wafers, etching rates and resulting cavity depths were determined with profilometry measurements (Dektak XT 2D, Bruker, Germany) and are shown (**Supplemental Figure S9**). Then, both wafers were wet etched in 49% hydrofluoric (HF) acid. The access port wafer was etched for 90 min with a etch depth of 560 μm and the microchannel wafer was etched for 85 min with an etch depth of 530 μm. Both wafers were placed in a Piranha bath to remove all photoresist.

The following steps were then applied to the microchannel wafer's top side. HMDS was spin-coated and then with SU8 3010 photoresist to have a thickness of approximately 12 μm. The wafer was exposed to UV at 130 mJ/cm^2 in hard contact mode. The wafer was then developed in SU8 developer (MicroChem Corp., Westborough, MA). SPR 220-7.0 was spin-coated to have a thickness of approximately 10 μm. The photoresist was exposed to UV at 250 mJ/cm^2 for 2 cycles, 30 seconds apart in hard contact mode. The wafer was then developed in CD-26 aqueous developer. The wafer was then hard baked in a vacuum oven at 120 ºC for 90 min. The wafer was placed in a chromium etch bath for 1 min. Parafilm® tape was applied on the bottom side of the wafer. The wafer was then wet etched in 49% HF acid for 17 min for an etch depth of 110 μm. The Parafilm® tape was then carefully removed. The SPR 220-7.0 layer was removed with an O_2 reactive ion etch (RIE) plasma cleaning (Plasma Equipment Technical Services, Brentwood, CA). Parafilm® tape was applied again on the bottom side of the wafer.

The wafer was wet etched in 49% HF acid for 15 min to have an etch depth of 100 µm. The Parafilm® tape was then carefully removed. The remaining photoresist was stripped off with a Piranha bath.

The following steps were then applied to the access port wafer's bottom side. HMDS was spin-coated and then with SPR 220-7.0 to have a thickness of approximately 10 µm. The photoresist was exposed to UV at 250 mJ/cm^2 for 2 cycles, 30 seconds apart in hard contact mode. The wafer was then developed in CD-26 aqueous developer. The wafer was then hard baked in a vacuum oven at 155 ºC for 90 min. Parafilm® tape was applied on the top side of the wafer. The wafer was placed in a chromium etch bath for 1 min. The wafer was then wet etched in 49% HF acid for 27 min for an etch depth of 175 µm. The Parafilm® tape was then carefully removed. Remaining photoresist was stripped off with a Piranha bath.

The following steps were then applied to both wafers. The wafers were placed in a chromium etch bath for 1 min. Both wafers were then placed in a Piranha bath. Both cleaned wafer halves were loaded into a plasma activation system (EVG 810, EVGroup, Austria) and the substrates were exposed to two separate capacitive coupled plasmas in sequence for a temporary bond, with a process previously described.[82] The two wafers were aligned onto each other with a mask aligner (EVG 620, EVGroup, Austria) to form the temporary bond. The wafers were then permanently bonded together using thermal fusion (EVG 501, EVGroup, Austria) for 9 hours with 19 kN pressure at 450 ºC. To dice the bonded wafers into individual microfluidic chips, the wafers were loaded into a dicing saw (Disco DAD 321, Japan) with the fluid ports downwards and Kapton® tape over the ESI tips to prevent water entrance into the channels.

Experimental

An expanded CAD model of the microfluidic chip fixture assembly is shown (**Figure 10a**). The microfluidic chip is housed in a custom machined white Delrin top and bottom fixtures that are attached to PEEK™ reservoir wells (P/N: C360-405R, LabSmith, Livermore, CA) which contain

the electrospray solutions. The electrode fixture contains platinum wires (23 gauge, LabSmith, Livermore, CA) that are located within the microchannel reservoir wells. The electrode fixture was 3D-printed with an Ender-3 Pro 3D Printer (Creality 3D Technology Co. Ltd, China) with polylactic acid (PLA) material. The microchip fixture subassembly was fixed onto a linear stage (ULTRAlign™ 561D-XYZ, Newport, USA) to precisely control the distance between the emitter tip and an aluminum counter electrode plate. The linear stage was mounted on top of a grey Delrin base plate. The counter electrode plate was also mounted onto a grey Delrin base and was set at a height to be adjacent to the microchip's emitter tip. The electrospray signal from the counter electrode plate was digitized by a data acquisition system, later described. The distance between the ESI emitter tip and the counter electrode plate was determined by calibrating the known movement of the emitter tip on the linear stage with the distance travelled as displayed on the digital microscope.

The custom voltage control and signal conditioning electronics are packaged on a printed circuit board (PCB) miniaturized system. The high voltage control electronics (**Figure 10b**) were designed for safe use and supply of four high voltage outputs from a single high voltage power supply. High voltage supplied to the system is fed into a series of resistors which provide three intermediate voltage values. These intermediate voltages can be adjusted with potentiometers mounted on the resistor tree board. Each of the outputs to the reservoirs are controlled by custom solid-state relays, which act as single pole triple throw (SP3T) switches. Each solid-state relay board corresponds to an output for each reservoir on the microfluidic chip. On the solid-state relay board that corresponds to the electrospray reservoir, the excess current from the buffer inlet microchannel (typically ~20 μA) was grounded through a 50 MΩ coupled in parallel with the electrospray voltage supply.[64] The controller board is connected to a custom LabVIEW© software program. The relays were constructed from high voltage transistors and photovoltaic optocouplers to allow high voltage operation. Solid state relays have advantages over mechanical relays such as high reliability, long lifespan, small form factor, low power

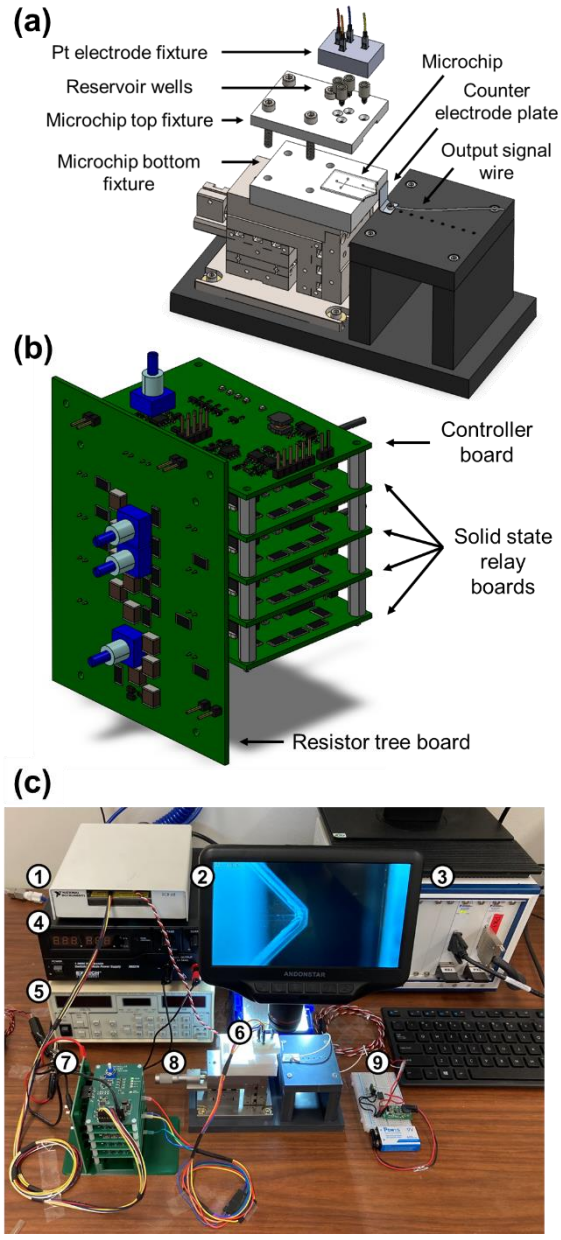

Figure 10. (a) Expanded microchip fixture assembly consisting of the linear stage, the microchip and its top and bottom fixtures, the Pt electrode fixture, and counter electrode plate. **(b)** Electronics for the control of four voltages from a single high voltage source. **(c)** Photograph of the experimental setup. **1.** National Instruments connector block. **2.** Digital microscope displaying a top-down view of the glass emitter tip. **3.** National Instruments Chassis. **4.** DC power supply for a vacuum pump (not shown). **5.** High voltage power supply. **6.** Microchip fixture and Pt electrode fixture. **7.** High voltage control electronics. **8.** Linear stage. **9.** Signal conditioning electronics.

consumption, no moving parts, and silent operation. The controller board includes several LEDs to indicate the state of the outputs, including one to warn of a live high voltage supply. The controller also features analog timing circuits to ensure that no high-voltage shoot-through can occur in the relays under any switching scenario. The spacing of the components on the PCBs in the subassembly was done per the guidelines for high voltage PCB design in IPC 2221B.

The PCBs for the high voltage control system were designed using KiCad 5.1.10 open-source software (http://kicad-pcb.org/). PCBs were manufactured by BasicPCB (Aurora, CO). The PCB circuits (**Supplemental Figure S10**) and parts list (**Supplemental Table S5**) are provided in the Supplemental Information. The manufacturer recommendations were followed for assembly. The controller board and the solid-state relay boards have dimensions of 2 × 3 in., and the resistor tree board has dimensions of 3 × 4 in. These PCBs were made with FR4 material and thickness of 0.62 in. Solder paste stencils were designed and purchased from Stencils Unlimited (Lake Oswego, OR) to solder on electrical surface mount components. Electrical surface mount components were placed onto the PCBs with solder paste under a digital microscope by using tweezers and a manual pick-and-place system (SMT Caddy, CA). Once components were placed on the PCB, re-flowing the solder was carried out with an automatic reflow oven (T-962 A, Shenzhen Bangqi Chuangyuan Technology Co., Ltd., Shenzhen, China). The boards were then mounted together with nylon hardware on a 3D-printed support structure made from green PLA.

A photograph of the benchtop experimental setup is shown (**Figure 10c**). A high-voltage power supply (Model PS350, Stanford Research Systems, Sunnyvale, CA) was used to supply a voltage to the high voltage control electronics which then provided four voltages to the microchannel reservoir wells. A digital microscope (Andonstar AD407, Shenzhen Andonstar Tech Co., Ltd., China) was used to display a top-down view of the electrospray at the glass emitter tip. The data acquisition was developed on National Instruments PXI hardware

comprised of: PXI-1031 Chassis, Module PXI-6281, and SCB-68 I/O connector block. The electrospray current signal is conditioned with a LMC662 (Texas Instruments, Dallas, TX) in a transimpedance (current-to-voltage) amplifier configuration. The circuit was designed using a common operational amplifier integrated circuit (IC) that was powered by a single 9 V battery. Electrical schematics for the power supply of the signal conditioning system are provided (**Supplemental Figure S11**) and the electrical schematic for the signal conditioning circuit is provided (**Supplemental Figure S12**). Data were recorded at 1000 samples/s using a National Instruments I/O card and a custom LabVIEW© software program (code provided via GitHub for non-commercial use, see details below).

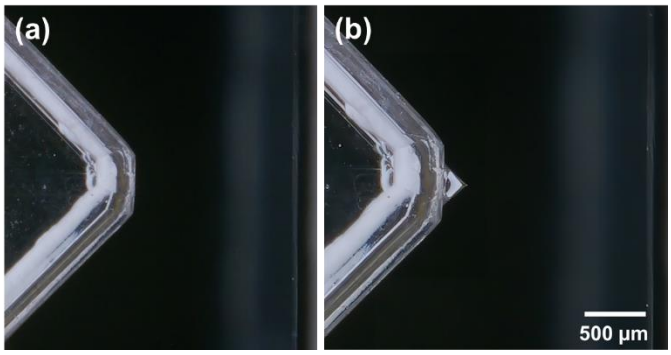

Figure 11. (a) Digital microscope image with a top-down view of the glass microfluidic chip emitter tip. **(b)** Digital microscope image with a top-down view of the electrospray Taylor cone generated at the glass emitter tip. The liquid being sprayed was 80/20 (v/v) methanol/acetonitrile with 0.1% acetic acid from the Sheath Liquid Interface (SLI) reservoir and 80/20 (v/v) methanol/acetonitrile with ammonium acetate at a concentration of 20 mM from the remaining three reservoirs.

Results and Discussion

In this study, electrospray was conducted using non-aqueous solutions in positive ionization mode. Aqueous content typically has higher surface tension and thus a higher voltage is required to access the cone jet mode. Unfortunately, higher voltages with aqueous solutions increases the risk of electrochemical discharge. A mixture of methanol and acetonitrile as used in this study are commonly applied solvents and ammonium acetate is a preferred choice as a background electrolyte.[64,65,73] Non-aqueous media may be suitable for electrochemical measurements and enable detection of compounds that are otherwise difficult to oxidize or

reduce under aqueous conditions.[83] For ESI, the formation of the electrospray favors lower surface tension and heat of vaporization of organic solvents.

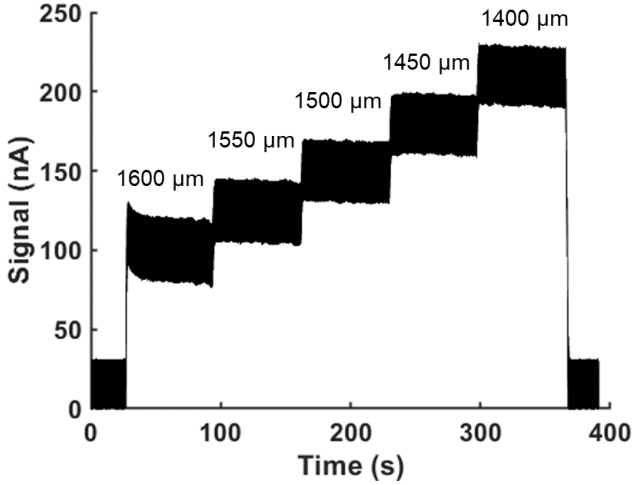

Figure 12. Signal response of electrospray ionization to the distance between the electrospray emitter tip and the metal counter electrode plate. The liquid being sprayed was 80/20 (v/v) methanol/acetonitrile with 0.1% acetic acid from the Sheath Liquid Inlet (SLI) reservoir and 80/20 (v/v) methanol/acetonitrile with ammonium acetate at a concentration of 20 mM from the remaining three reservoirs. A constant voltage of +2.7 kV was applied to the SLI reservoir to perform electrospray.

Voltages were applied through the platinum wires placed in the microchannel reservoir wells. In the electrospray experiments, a supply voltage of +3.0 kV was provided to the high voltage control electronics. For all experiments, a voltage of +2.9 kV was supplied to the buffer inlet (BI), +2.6 kV was applied to the sample inlet (SI) and sample outlet (SO), and +2.7 kV was applied to the sheath liquid inlet (SLI). These output voltages were measured and verified with an oscilloscope (MDO3012, Tektronix, Beaverton, OR). **Figure 11a** shows a digital microscope image with a top-down view of the glass microfluidic chip emitter tip and **Figure 11b** shows a digital microscope image with a top-down view of the electrospray Taylor cone generated at the glass emitter tip. Once the voltage was applied, no accumulation of droplets at the opening tip or liquid spreading occurred. The liquid being sprayed was 80/20 (v/v) methanol/acetonitrile with 0.1% acetic acid from the SLI reservoir and 80/20 (v/v) methanol/acetonitrile with ammonium acetate at a concentration of 20 mM from the remaining three reservoirs. While observing the ESI signal intensity, the linear stage adjusted the position of the integrated emitter tip with

respect to the counter electrode plate, and then the spray voltage initiated. **Figure 12** shows the signal response of electrospray to the distance between the emitter tip and the counter electrode plate. Distances from the emitter tip to the counter electrode plate from 1600 to 1400 µm with 50 µm intervals and 1 min durations. An initial spike in the signal is observed for the 1600 µm distance interval since the emitter tip was briefly brought to a distance of 1580 µm to help initialize electrospray onset and formation and then it was quickly brought back to 1600 µm. The PEEK™ reservoir wells have a volume of 85 µL, which is sufficient to providing solution for electrospray for at least 5 min. The signal demonstrates that the integrated emitter tip is efficient at generating a stable electrospray at varying emitter tip distances. The emitter tip geometry is sufficiently sharp to facilitate the formation of a Taylor cone immediately when the ESI voltage is applied and adjusting the emitter tip distance.

Replicated signal response data of electrospray ionization to the distance between the electrospray emitter tip and the metal counter electrode plate are shown (**Figure 13a**). The liquid being sprayed was 80/20 (v/v) methanol/acetonitrile with 0.1% acetic acid from the SLI reservoir and 80/20 (v/v) methanol/acetonitrile with ammonium acetate (20 mM) from the remaining three reservoirs. Data are averaged over 1 min durations for n=5 replicates. The ESI signal ranged from approximately 80 to 200 nA. These data obtained for the distance sweep resulted a correlation coefficient of r^2=0.99. **Figure 13b** shows replicate signal response data of electrospray ionization to the concentration of ammonium acetate at an emitter distance of 1600 µm. The liquid being sprayed was the same as was done in **Figure 13a** with varying concentrations of ammonium acetate. Data are averaged over 1 min durations for n=5 replicates. The ESI signal ranged from approximately 50 to 150 nA. These data obtained in the concentration sweep resulted a correlation coefficient r^2=0.95.

From the results shown, the system provides good electrospray stability and reproducibility. The emitter tip geometry is sufficiently sharp to avoid potential liquid-spreading and to decrease the required voltage for establishing a stable Taylor cone. High-resolution control of the emitter

tip distance from the counter electrode plate by using a high-resolution linear stage allows for precise measurements of electrospray signal dependency on distance. The solvents used in this study, methanol, and acetonitrile, have lower viscosities compared to water. This lower viscosity allows for a lower electrospray onset voltage thus avoiding electrical discharge. Ammonium acetate is used as a typical BGE at low concentrations (10-40 mM) due to its high volatility and compatibility with established separation and analysis methods (i.e., capillary electrophoresis,

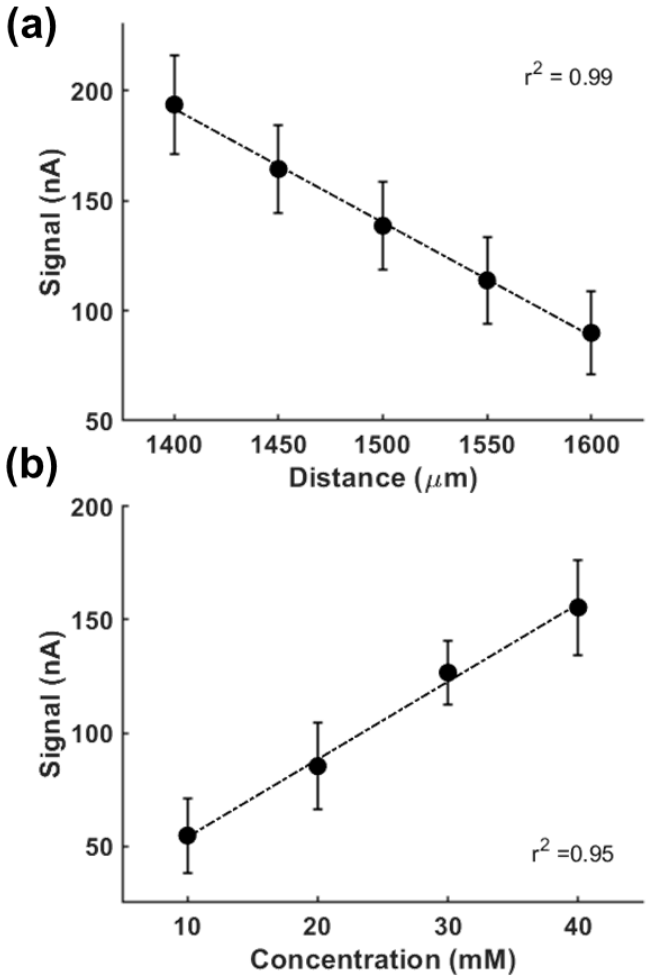

Figure 13. (a) Signal response of electrospray ionization to the distance between the electrospray emitter tip and the metal counter electrode plate. The liquid being sprayed was 80/20 (v/v) methanol/acetonitrile with 0.1% acetic acid from the Sheath Liquid Inlet (SLI) reservoir and 80/20 (v/v) methanol/acetonitrile with ammonium acetate at a concentration of 20 mM from the remaining three reservoirs. A constant voltage of +2.7 kV was applied to the SLI reservoir to perform electrospray. Data are averaged over 1 min durations for n=5 replicates. **(b)** Signal response of electrospray ionization to the concentration of ammonium acetate at an emitter distance of 1600 µm. The liquid being sprayed, and voltage applied to the SLI reservoir were the same as was done in caption (a) with varying concentrations. Data are averaged over 1 min durations for n=5 replicates.

mass spectrometry). Reproducible and stable data were shown for the dependence of the electrospray signal on the concentration of ammonium acetate. Live video feedback from a digital microscope used to display the electrospray emitter tip and formation of the Taylor cone was particularly useful to determine the experimental parameters (onset voltage and emitter tip distance) necessary for functional ESI.

Conclusion

In this work, we present the microfabrication and operation of a three-dimensional electrospray ionization (ESI) emitter tip made from glass. Our fabrication process relies on standard microfabrication techniques, yet it involves the novel application of two layers of positive and negative photoresists in addition to Parafilm® wax tape. Open edge and tiered depth details were successfully created from a multilayer planar mask. We demonstrate the fundamental performance of electrospray with this microfluidic chip. The emitter tip was fixed on a linear axis stage with high resolution to finely control the tip's distance from a metal counter electrode plate. High voltage control electronics were developed to safely supply four voltages applied to the microchip's four ports from a single high voltage power supply. To readily form the electrospray, non-aqueous solvents were used for their low viscosity and a constant voltage of +2.7 kV was applied to the sheath electrospray microchannel. The liquid being sprayed was 80/20 (v/v) methanol/acetonitrile with 0.1% acetic acid in the sheath microchannel and with ammonium acetate (10-40 mM) in its remaining microchannels. The electrospray signal was measured in response to varying the distance (1.4 to 1.6 mm) between the electrospray emitter tip and a metal counter electrode plate in addition to the varying concentration of the background electrolyte, ammonium acetate. Stable and repeatable electrospray signal showed linear relationships with emitter tip distance and concentration ($r^2 \geq 0.95$). Data were also shown for the dependence of the electrospray signal on the concentration of ammonium acetate. Live video feedback from a digital microscope used to display the electrospray emitter tip and formation of the Taylor cone was particularly useful to determine the experimental parameters

(onset voltage and emitter tip distance) necessary for functional ESI. Further work envisions the development and testing of the experimental design and setup with microfluidic chemical separation methods (e.g., capillary electrophoresis) and its integration with novel micro-scaled chemical sensors to allow further separation and detection of ionized molecules (e.g., high asymmetric longitudinal field ion mobility spectrometry).[84,85] Further work also envisions the use of the electronics for precise voltage switching times between sample injection and separation modes. These novel concepts may be applied to medical analyses and clinical diagnostics for enhanced portability, reliability, and throughput.[86]

Conflicts of Interest

The authors declare no competing financial interest. The electrical schematics and LabVIEW© code for data acquisition from the system is available on GitHub for non-commercial use. Please refer to Professor Cristina Davis' webpage for more information.

Acknowledgements

Partial support was provided by NIH awards: U01 EB0220003-01 (CED, NJK); UL1 TR001860 (CED, NJK); 1P30ES023513-01A1 (CED, NJK); UG3-OD023365 (CED, NJK); 1U18TR003795-01 (CED, NJK), 4U18TR003795-02 (CED, NJK); and 1U01TR004083-01 (CED, NJK). Partial support was also provided by: the Department of Veterans Affairs award I01 BX004965-01A1 (CED, NJK); the University of California Tobacco-Related Disease Research Program award T31IR1614 (CED, NJK); and University of California CITRIS and the Banatao Institute award

19-0092 (CED, NJK). Trainee support was provided by NIH TL1 TR001861 (AJS) and T32 HL07013 (KOZ). The contents of this manuscript are solely the responsibility of the authors and do not necessarily represent the official views of the funding agencies. The authors gratefully acknowledge access and use of the UC Davis Center for Nano and Micro Manufacturing (CNM2). The authors also gratefully acknowledge Mitchell McCartney, Patrick Gibson, Bradley Chew, and Jean-Pierre Delplanque (University of California, Davis) for technical discussions.

Supplemental Information

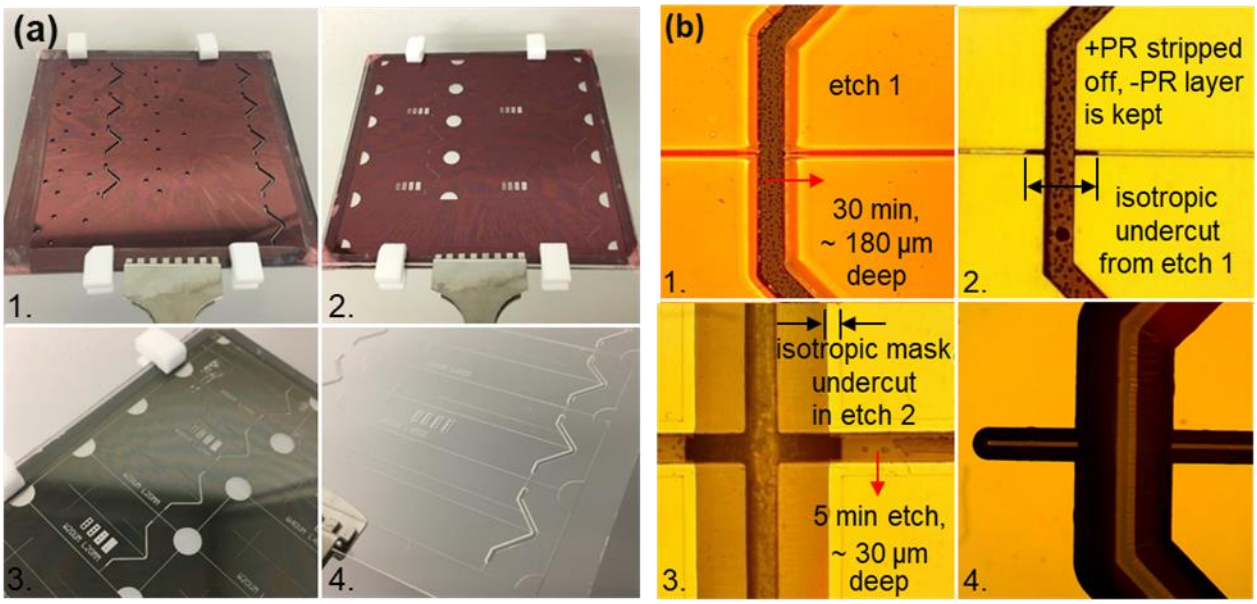

Supplemental Figure S8. Fabrication of open edge features with tiered depth geometries. **(a)** Wafer view of microchips after four main steps: 1. The back side etched cavities (560 µm) set the nozzle thickness and form an open edge. 2. The front side etch cavities for the two wafers (110 and 175 µm) define the nozzle edge. 3. 100 µm deep etch of microchannels and finish nozzle through wafer etch release. 4. Wafer with chips ready for dicing. Panel **(b)** shows the same four processes observed in a microscope.

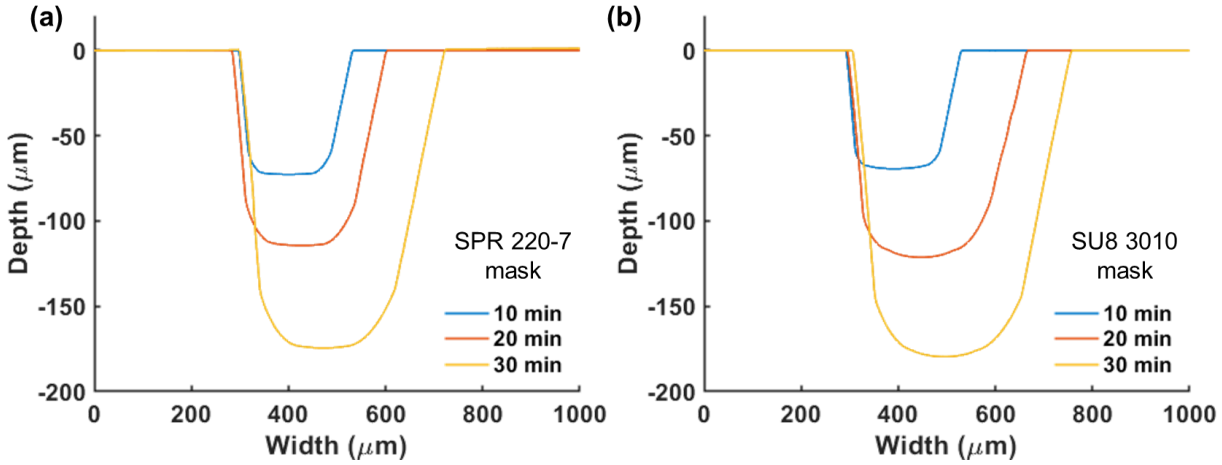

Supplemental Figure S9. Measured depth and width of the etched cavities with a profilometer. Schott Borofloat glass with 100 nm sputtered Chromium layer and spin-coated photoresist mask, etched in 49% HF acid, no agitation for 10, 20, and 30 min. **(a)** SPR 220-7, 10 µm thick mask. **(b)** SU-8 3010, 10 µm thick mask.

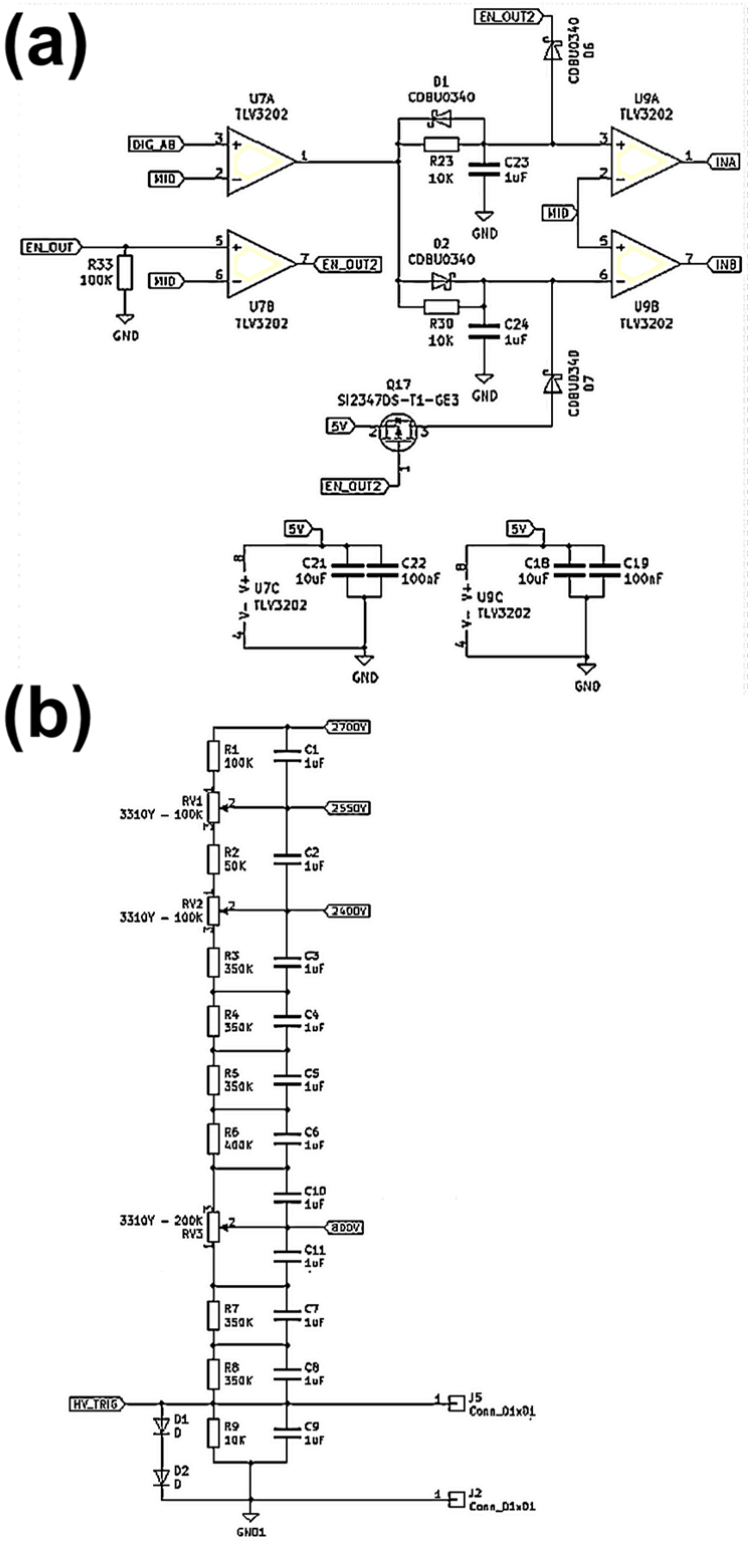

Supplemental Figure S10. Electrical circuit schematics of the voltage divider system. **(a)** Controller circuit board. **(b)** Resistor tree board. **(c)** (Next page) Solid-state relay board for the Buffer Inlet (BI) reservoir, Sample Inlet (SI) reservoir, and Sample Outlet (SO) reservoir. **(d)** Solid-state relay board for the Sheath Liquid Inlet (SLI) reservoir.

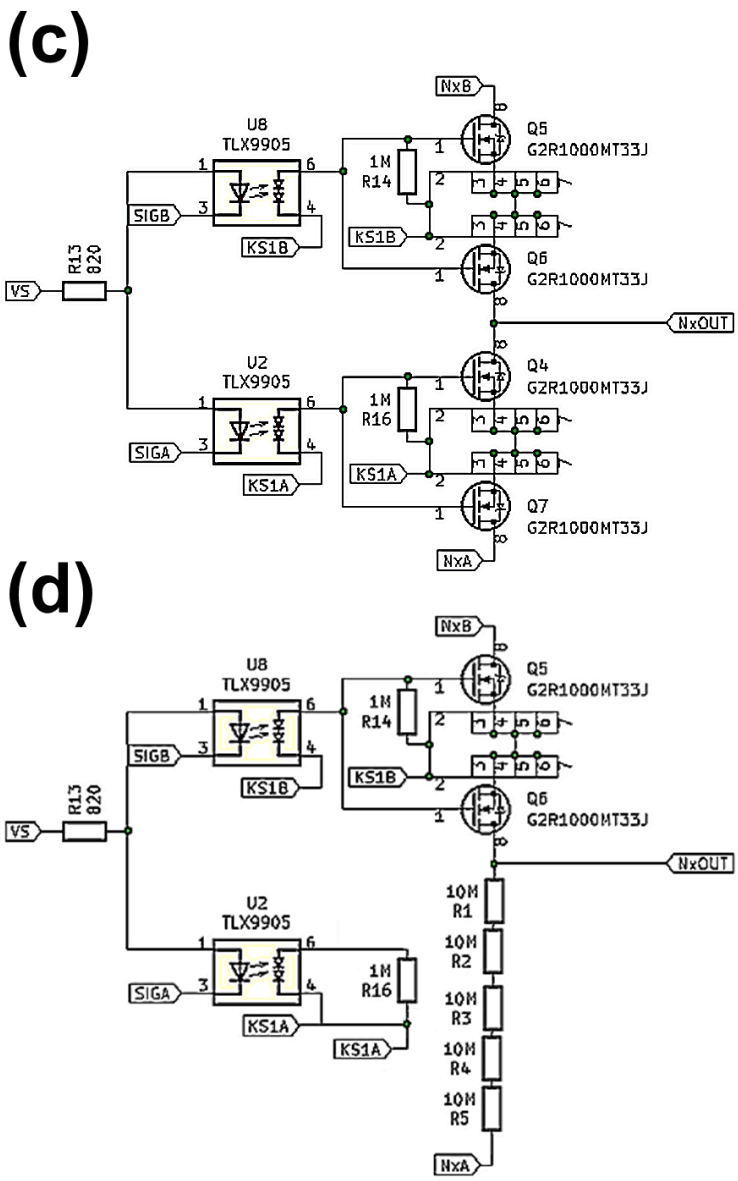

Supplemental Figure S10. (Continued) Electrical circuit schematics of the voltage divider system. **(a)** Controller circuit board. **(b)** Resistor tree board. **(c)** Solid-state relay board for the Buffer Inlet (BI) reservoir, Sample Inlet (SI) reservoir, and Sample Outlet (SO) reservoir. **(d)** Solid-state relay board for the Sheath Liquid Inlet (SLI) reservoir.

Supplemental Table S5: A list of surface mount electrical components for the voltage control and signal conditioning electronics.

Description	Manufacturer	Manufacturer Part #	Value	Quantity per PCB	Footprint
Solid state relays					
Pin header	Molex	50-29-1620	Conn_01x04	2	Connector_PinHeader_2.54mm:PinHeader_1x04_P2.54mm_Vertical
Pin header	Molex	22-28-8151	Conn_01x02	4	Connector_PinHeader_2.54mm:PinHeader_1x02_P2.54mm_Horizontal
MOSFET	GeneSiC Semiconductor	G2R1000MT33J	-	4	MKL:TO-263-7_G2R1000MT33J
Resistor	Bourns	CHV2512-FX-1005ELF	10M	5	Resistor_SMD:R_2512_6332Metric
Resistor	Vishay / Dale	CRCW0603820RFKEAHP	820	1	Resistor_SMD:R_0603_1608Metric
Resistor	Bourns	CHV0603AFX-1004ELF	1M	2	Resistor_SMD:R_0603_1608Metric
Photovoltaic coupler	Toshiba	TLX9905(TPL,F	-	2	Package_SO:MFSOP6-4_4.4x3.6mm_P1.27mm
Controller					
Capacitor	Samsung Electro-Mechanics	CL10A105KA8NNNL	1uF	4	Capacitor_SMD:C_0603_1608Metric
Capacitor	Samsung Electro-Mechanics	CL10A106KO8NQNC	10uF	7	Capacitor_SMD:C_0603_1608Metric
Capacitor	Samsung Electro-Mechanics	CL10B104KA8NNWC	100nF	6	Capacitor_SMD:C_0603_1608Metric
Capacitor	Samsung Electro-Mechanics	CL10B222KB8NNNC	2.2nF	1	Capacitor_SMD:C_0603_1608Metric
Diode	Comchip Technology	CDBU0340	-	8	Diode_SMD:D_0603_1608Metric
Diode	ROHM Semiconductor	RSX101MM-30TR	-	1	Diode_SMD:D_SOD-123
LED	ROHM Semiconductor	SMLMN2ECTT86C	-	5	LED_SMD:LED_0805_2012Metric
Diode	onsemi	MMSD4148T1G	-	1	Diode_SMD:D_SOD-123F
Pin header	Molex	50-29-1620	Conn_01x04	2	Connector_PinHeader_2.54mm:PinHeader_1x04_P2.54mm_Vertical
Pin header	Molex	22-28-8151	Conn_01x02	2	Connector_PinHeader_2.54mm:PinHeader_1x02_P2.54mm_Horizontal
Pin header	Molex	50-29-1620	Conn_01x06	1	Connector_PinHeader_2.54mm:PinHeader_1x06_P2.54mm_Vertical
Pin header	Molex	50-29-1620	Conn_01x02	1	Connector_PinHeader_2.54mm:PinHeader_1x02_P2.54mm_Vertical
Inductor	Bourns	SRN6045TA-680M	68uH	1	MKL:BOURNS_SRN6045TA
MOSFET	Nexperia	NX7002AKVL	-	8	Package_TO_SOT_SMD:SOT-23
MOSFET	Vishay Semiconductors	SI2347DS-T1-GE3	-	3	Package_TO_SOT_SMD:SOT-23
Resistor	Bourns	CR0603-JW-512ELF	5.1K	1	Resistor_SMD:R_0603_1608Metric
Resistor	Bourns	CHP0603AFX-1002ELF	10K	6	Resistor_SMD:R_0603_1608Metric
Resistor	Bourns	CHV0603AFX-1003ELF	100K	6	Resistor_SMD:R_0603_1608Metric
Resistor	Bourns	CHP0603AFX-1000ELF	100	2	Resistor_SMD:R_0603_1608Metric
Resistor	Bourns	CMP0603-FX-3300ELF	330	5	Resistor_SMD:R_0603_1608Metric
Resistor	Bourns	CHP0603AFX-1001ELF	1K	1	Resistor_SMD:R_0603_1608Metric
Potentiometer	Bourns	3310Y-001-104L	100K	1	MKL:Potentiometer_Bourns_3310Y_Vertical
MOSFET	Microchip Technology	TC4427VOA	-	1	Package_SO:SOIC-8_3.9x4.9mm_P1.27mm
Dual push-pull comparator	Texas Instruments	TLV3202AID	-	3	Package_SO:SOIC-8_3.9x4.9mm_P1.27mm
Voltage reference	Texas Instruments	LM4120IM5-2.5/NOPB	-	1	Package_TO_SOT_SMD:SOT-23-5
Switching voltage regulator	Microchip Technology / Micrel	MIC4680-5.0YM	-	1	Package_SO:SOIC-8_3.9x4.9mm_P1.27mm
Resistor Tree					
Capacitor	TDK	CGA9P4X7T2W105K250KE	1uF	10	Capacitor_SMD:C_2220_5650Metric
Capacitor	Samsung Electro-Mechanics	187-CL10A105KA8NNNL	1uF	1	Capacitor_SMD:C_0603_1608Metric
Diode	onsemi	863-MMSD4148T1G	-	2	Diode_SMD:D_SOD-123F
Pin header	Molex	50-29-1620	Conn_01x01	2	Connector_PinHeader_2.54mm:PinHeader_1x01_P2.54mm_Vertical
Pin header	Molex	50-29-1620	Conn_01x02	2	Connector_PinHeader_2.54mm:PinHeader_1x02_P2.54mm_Vertical
Pin header	Molex	50-29-1620	Conn_01x02	10	Connector_PinSocket_2.54mm:PinSocket_1x02_P2.54mm_Vertical
Resistor	Bourns	CMP2512-FX-1003ELF	100K	1	Resistor_SMD:R_2512_6332Metric
Resistor	Stackpole Electronics Inc	HVCB2512FDD50K0	50K	1	Resistor_SMD:R_2512_6332Metric
Resistor	Vishay / Dale	CRCW2512348KFKEG	350K	5	Resistor_SMD:R_2512_6332Metric
Resistor	Vishay / Dale	CRCW2512402KFKEG	400K	1	Resistor_SMD:R_2512_6332Metric
Resistor	Bourns	CHP0603AFX-1002ELF	10K	1	Resistor_SMD:R_0603_1608Metric
Resistor	Bourns	CMP2512-FX-1001ELF	1K	6	Resistor_SMD:R_2512_6332Metric
Potentiometer	Bourns	3310Y-001-204L	200K	3	MKL:Potentiometer_Bourns_3310Y_Vertical

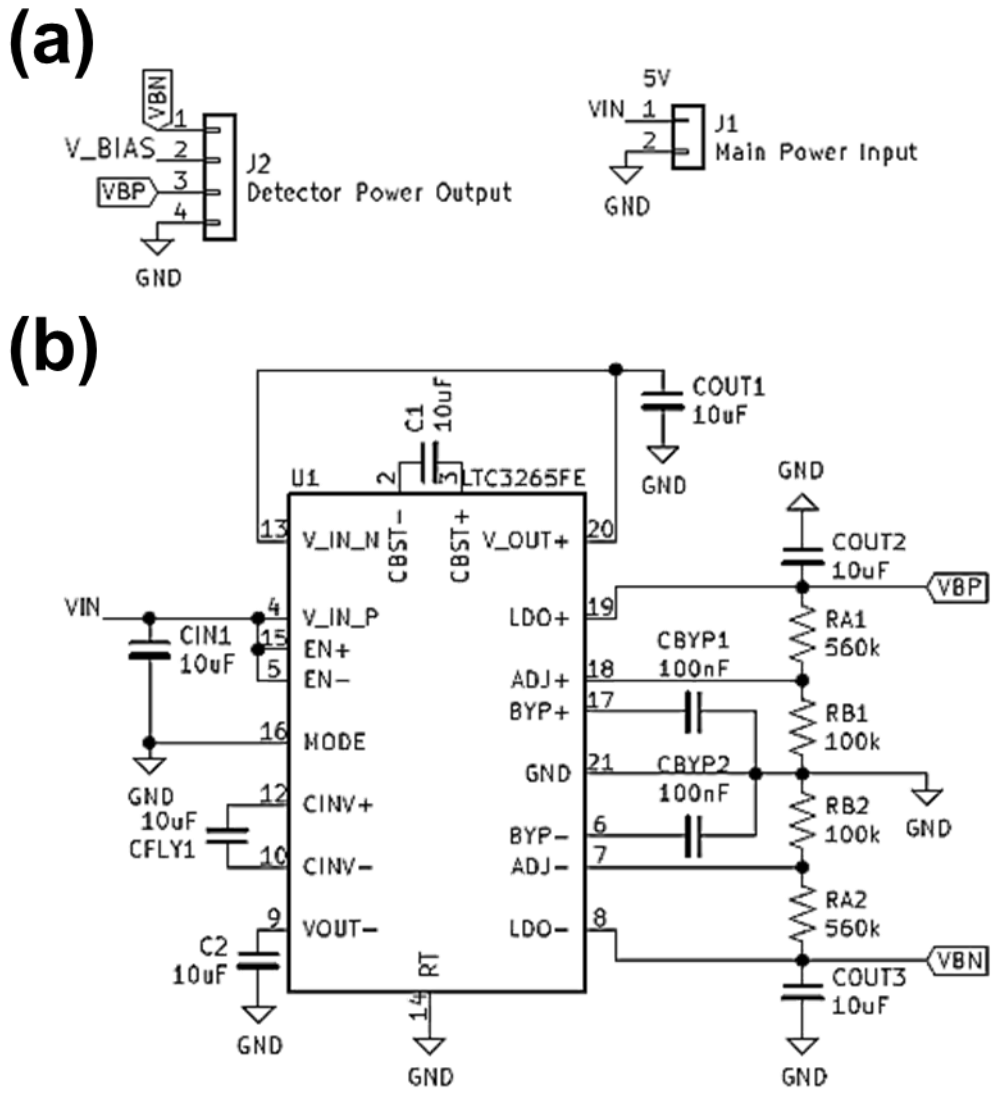

Supplemental Figure S11. Electrical schematic of the printed circuit board (PCB) that provides the power for the signal conditioning system. **(a)** The output and input connections to the PCB. **(b)** Charge pump based integrated circuit that provides the positive and negative voltage rails for the system. **(c)** (Next page) Low-noise regulators supply the voltage bias that can be set to negative or positive configuration according to the polarity of analytes under investigation.

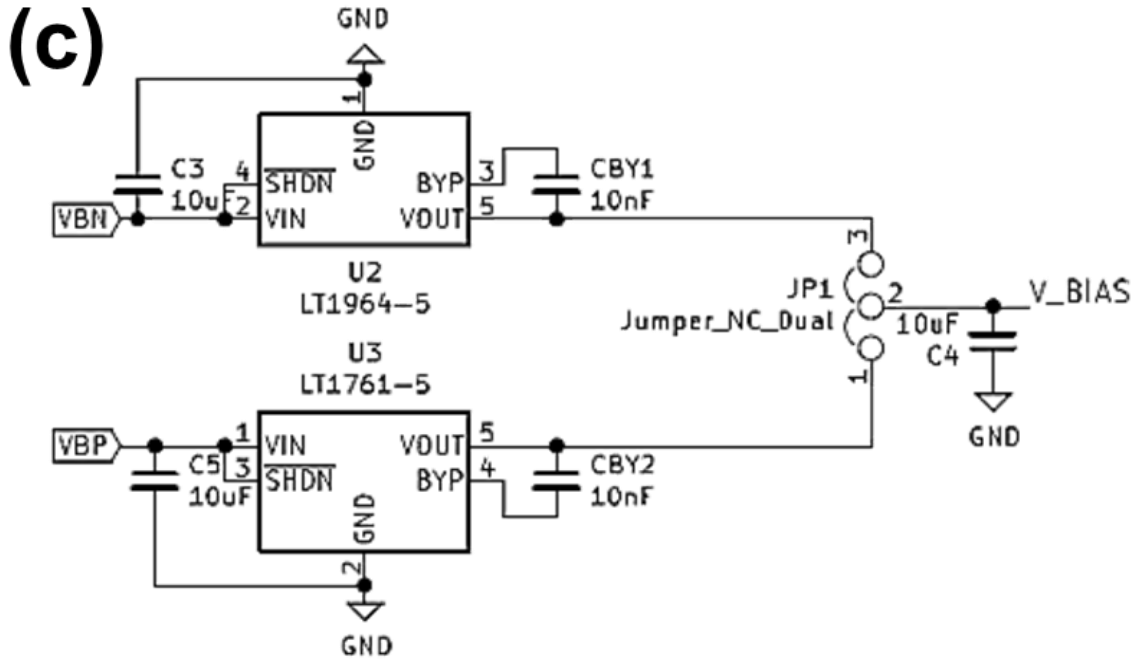

Supplemental Figure S11. (Continued) Electrical schematic of the printed circuit board (PCB) that provides the power for the signal conditioning system. **(a)** The output and input connections to the PCB. **(b)** Charge pump based integrated circuit that provides the positive and negative voltage rails for the system. **(c)** Low-noise regulators supply the voltage bias that can be set to negative or positive configuration according to the polarity of analytes under investigation.

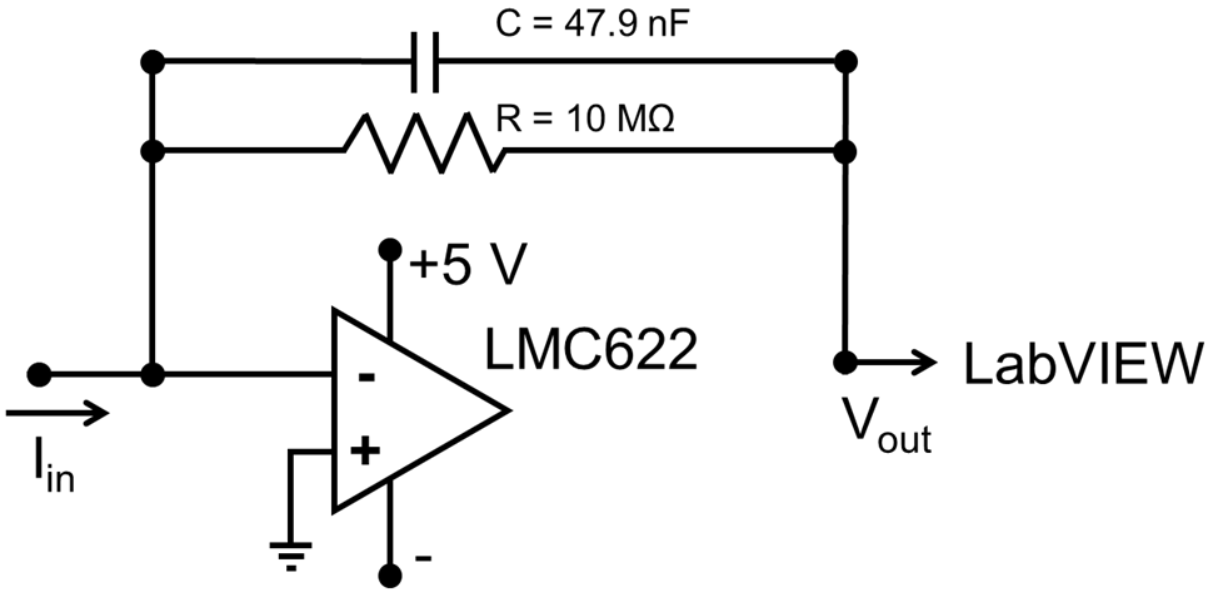

Supplemental Figure S12. Electrical schematic of the signal conditioning circuit which amplifies the input electrospray current signal and converts it to a voltage that can be digitized by the LabVIEW© system.

Chapter 5: Conclusions and Future Directions

The miniaturized EBC collection device described in Chapter 2 allows for minimal sample volumes needed for representative studies. This opens a non-invasive way to study metabolic effects of environmental exposure and medical interventions using measurable targets in many health conditions including asthma. Untargeted analysis measures all endogenous metabolic signals in a biological sample, which allows for the discovery of novel biomarkers that can explain differences in health conditions. Targeted analysis allows for quantifying a predefined set of selected metabolites, which are related to certain diseases and medical conditions. In future applications, this miniature breath collector may transport the collected sample from its collection surface unit into an interfaced analytical or storage unit with minimal power input. The amount of sample collection could be reduced to a few microliters and sampling time to a few minutes when collection and analysis are possible with novel microfluidic platforms. Further untargeted metabolite analysis may be explored, similarly done for targeted metabolites. This device is able to finely resolve time data sequence on the order of hours and can lead to a substantial amount of potential data to be collected for increasing the power of various studies. Currently, there are no other reports of EBC studies that allow for monitoring individuals longitudinally instead of cross-sectionally at study visits which can be a major advantage in personal health monitoring. Additionally, its portability is advantageous because it enables breath samples to be collected in multiple environments, including intensive care units (ICUs), outpatient clinics, workplaces, and at home. The addition of alternative separation and detection platforms would present further opportunities to discover more metabolites correlated with other respiratory diseases including asthma.

The EBC sampler device described in Chapter 3 was modified with varying notch filter lengths to determine if breath aerosol size affects EBC metabolite content. This device features a saliva trap to allow selective filtering of breath aerosols by capturing heavy droplets ($\gtrsim$ 100

μm) and allowing small aerosols (≲ 20 μm) which originate in the deep lungs to pass through. Ten notch filter lengths were simulated with the device to calculate the effect of filter length on the breath aerosol size distribution and the proportion of aerosols which make their way through to the EBC collection tube. Additionally, three notch filter lengths were experimentally tested with the device to determine if there are variations of breath metabolomic profiles. From simulation results, particles typically larger than 10 μm were filtered out for notches longer than 18 mm. This indicates that a longer notch filter in this device prevents larger particles from reaching the collection tube thus altering the aerosol particle size distribution. We did not see strong statistical evidence of systematic metabolite differences between breath aerosol size distributions. If there are differences in metabolomic content based on breath aerosol size, it is possible that they are not significant for practical sampling if the sampling device design has already been optimized for proper saliva filtering, cooling temperature, and air flow rates.

The work in Chapter 4 presents the microfabrication and operation of a three-dimensional electrospray ionization (ESI) emitter tip made from glass. Glass is an important material of choice for analytical and medical field applications due to its excellent material and chemical properties (i.e., mechanical strength, chemical inertness, optical transparency, and native hydrophilicity). ESI tips can be easily realized with well-established silicon microfabrication protocols, although silicon is electrically conductive and thus prevents its integration with chemical separation methods (e.g., chromatography or capillary electrophoresis) which require high voltages for operation. We demonstrate the fundamental performance of electrospray with this microfluidic chip. The emitter tip was fixed on a linear axis stage with high resolution to finely control the tip's distance from a metal counter electrode plate. High voltage control electronics were developed to safely supply four voltages applied to the microchip's four ports from a single high voltage power supply. Stable and repeatable electrospray signal showed linear relationships with emitter tip distance and concentration ($r^2 \geq 0.95$). Data were also shown for the dependence of the electrospray signal on the concentration of ammonium acetate.

Further work envisions the development and testing of the experimental design and setup with microfluidic chemical separation methods (e.g., capillary electrophoresis) and its integration with novel micro-scaled chemical sensors to allow further separation and detection of ionized molecules from for example, EBC. Further work also envisions the use of the electronics for precise voltage switching times between sample injection and separation modes. These novel concepts may be applied to medical analyses and clinical diagnostics for enhanced portability, reliability, and throughput.

References

1. Horváth, I, Hunt, J and Barnes, PJ. (2005) Exhaled breath condensate: methodological recommendations and unresolved questions. *European Respiratory Journal* 26: 523–548. DOI:10.1183/09031936.05.00029705.
2. Zamuruyev, KO, Aksenov, AA, Pasamontes, A, Brown, JF, Pettit, DR, Foutouhi, S, Weimer, BC, Schivo, M, Kenyon, NJ, Delplanque, JP and Davis, CE. (2017) Human breath metabolomics using an optimized non-invasive exhaled breath condensate sampler. *Journal of Breath Research* 11: DOI:10.1088/1752-7163/11/1/016001.
3. Aksenov, AA, Zamuruyev, KO, Pasamontes, A, Brown, JF, Schivo, M, Foutouhi, S, Weimer, BC, Kenyon, NJ and Davis, CE. (2017) Analytical methodologies for broad metabolite coverage of exhaled breath condensate. *Journal of Chromatography B* 1061–1062: 17–25. DOI:10.1016/j.jchromb.2017.06.038.
4. Prudent, M and Girault, HH. (2009) Functional electrospray emitters. *Analyst* 134: 2189–2203. DOI:10.1039/b910917j.
5. Peralbo-Molina, A, Calderón-Santiago, M, Priego-Capote, F, Jurado-Gámez, B and Luque de Castro, MD. (2015) Development of a method for metabolomic analysis of human exhaled breath condensate by gas chromatography-mass spectrometry in high resolution mode. *Analytica Chimica Acta* 887: 118–126. DOI:10.1016/j.aca.2015.07.008.
6. Winters, BR, Pleil, JD, Angrish, MM, Stiegel, MA, Risby, TH and Madden, MC. (2017) Standardization of the collection of exhaled breath condensate and exhaled breath aerosol using a feedback regulated sampling device. *Journal of Breath Research* 11: DOI:10.1088/1752-7163/aa8bbc.
7. Pleil, JD and Stiegel, MA. (2013) Evolution of environmental exposure science: Using breath-borne biomarkers for ‘discovery’ of the human exposome. *Analytical Chemistry* 85: 9984–9990. DOI:10.1021/ac402306f.
8. Kazani, S, Planaguma, A, Ono, E, Bonini, M, Zahid, M, Marigowda, G, Wechsler, ME, Levy, BD and Israel, E. (2013) Exhaled breath condensate eicosanoid levels associate with asthma and its severity. *Journal of Allergy and Clinical Immunology* 132: 547–553. DOI:10.1016/j.jaci.2013.01.058.
9. Fritscher, LG, Post, M, Rodrigues, MT, Silverman, F, Balter, M, Chapman, KR and Zamel, N. (2012) Profile of eicosanoids in breath condensate in asthma and COPD. *Journal of Breath Research* 6: 26001. DOI:10.1088/1752-7155/6/2/026001.
10. Pelclová, D, Fenclová, Z, Vlcková, S, Lebedová, J, Syslová, K, Pecha, O, Belácek, J, Navrátil, T, Kuzma, M and Kacer, P. (2012) Leukotrienes B4, C4, D4 and E4 in the exhaled breath condensate (EBC), blood and urine in patients with pneumoconiosis. *Industrial health* 50: 299–306. DOI:10.2486/indhealth.MS1274.
11. Esther, CR, Olsen, BM, Lin, F-C, Fine, J and Boucher, RC. (2013) Exhaled breath condensate adenosine tracks lung function changes in cystic fibrosis. *AJP: Lung Cellular and Molecular Physiology* 304: L504–L509. DOI:10.1152/ajplung.00344.2012.
12. Antczak, A, Montuschi, P, Kharitonov, S, Gorski, P and Barnes, PJ. (2002) Increased exhaled cysteinyl-leukotrienes and 8-isoprostane in aspirin-induced asthma. *American Journal of Respiratory and Critical Care Medicine* 166: 301–306. DOI:10.1164/rccm.2101021.
13. Baraldi, E. (2003) Cysteinyl leukotrienes and 8-isoprostane in exhaled breath condensate of children with asthma exacerbations. *Thorax* 58: 505–509. DOI:10.1136/thorax.58.6.505.
14. Zanconato, S, Carraro, S, Corradi, M, Alinovi, R, Pasquale, MF, Piacentini, G, Zacchello, F and Baraldi, E. (2004) Leukotrienes and 8-isoprostane in exhaled breath condensate of children with stable and unstable asthma. *Journal of Allergy and Clinical Immunology*

113: 257–263. DOI:10.1016/j.jaci.2003.10.046.
15. Montuschi, P and Barnes, PJ. (2002) Exhaled leukotrienes and prostaglandins in asthma. *The Journal of allergy and clinical immunology* 109: 615–20. DOI:10.1067/mai.2002.122461.
16. Montuschi, P. (2008) Leukotrienes, Antileukotrienes and Asthma. *Mini-Reviews in Medicinal Chemistry* 8: 647–656. DOI:10.2174/138955708784567395.
17. Montuschi, P, Martello, S, Felli, M, Mondino, C, Barnes, PJ and Chiarotti, M. (2005) Liquid chromatography/mass spectrometry analysis of exhaled leukotriene B4 in asthmatic children. *Respiratory Research* 6: DOI:10.1186/1465-9921-6-119.
18. Montuschi, P, Martello, S, Felli, M, Mondino, C and Chiarotti, M. (2004) Ion trap liquid chromatography/tandem mass spectrometry analysis of leukotriene B4 in exhaled breath condensate. *Rapid Communications in Mass Spectrometry* 18: 2723–2729. DOI:10.1002/rcm.1682.
19. Montuschi, P. (2009) LC/MS/MS analysis of leukotriene B4 and other eicosanoids in exhaled breath condensate for assessing lung inflammation☆. *Journal of Chromatography B* 877: 1272–1280. DOI:10.1016/j.jchromb.2009.01.036.
20. Syslová, K, Kačer, P, Vilhanová, B, Kuzma, M, Lipovová, P, Fenclová, Z, Lebedová, J and Pelclová, D. (2011) Determination of cysteinyl leukotrienes in exhaled breath condensate: Method combining immunoseparation with LC-ESI-MS/MS. *Journal of Chromatography B: Analytical Technologies in the Biomedical and Life Sciences* 879: 2220–2228. DOI:10.1016/j.jchromb.2011.06.004.
21. Sanak, M, Gielicz, A, Nagraba, K, Kaszuba, M, Kumik, J and Szczeklik, A. (2010) Targeted eicosanoids lipidomics of exhaled breath condensate in healthy subjects. *Journal of Chromatography B* 878: 1796–1800. DOI:10.1016/j.jchromb.2010.05.012.
22. Glowacka, E, Jedynak-Wasowicz, U, Sanak, M and Lis, G. (2013) Exhaled eicosanoid profiles in children with atopic asthma and healthy controls. *Pediatric Pulmonology* 48: 324–335. DOI:10.1002/ppul.22615.
23. Sachs-Olsen, C, Sanak, M, Lang, AM, Gielicz, A, Mowinckel, P, Lødrup Carlsen, KC, Carlsen, K-H and Szczeklik, A. (2010) Eoxins: A new inflammatory pathway in childhood asthma. *Journal of Allergy and Clinical Immunology* 126: 859-867.e9. DOI:10.1016/j.jaci.2010.07.015.
24. Ono, E *et al.* (2014) Lipoxin generation is related to soluble epoxide hydrolase activity in severe asthma. *American Journal of Respiratory and Critical Care Medicine* 190: 886–897. DOI:10.1164/rccm.201403-0544OC.
25. Levy, BD. (2012) Resolvin D1 and Resolvin E1 Promote the Resolution of Allergic Airway Inflammation via Shared and Distinct Molecular Counter-Regulatory Pathways. *Frontiers in Immunology* 3: DOI:10.3389/fimmu.2012.00390.
26. Dutta, K, Prasad, P and Sinha, D. (2015) Chronic low level arsenic exposure evokes inflammatory responses and DNA damage. *International Journal of Hygiene and Environmental Health* 218: 564–574. DOI:10.1016/j.ijheh.2015.06.003.
27. Syslová, K, Kačer, P, Kuzma, M, Pankrácová, A, Fenclová, Z, Vlčková, Š, Lebedová, J and Pelclová, D. (2010) LC-ESI-MS/MS method for oxidative stress multimarker screening in the exhaled breath condensate of asbestosis/silicosis patients. *Journal of Breath Research* 4: 17104. DOI:10.1088/1752-7155/4/1/017104.
28. Janicka, M, Kubica, P, Kot-Wasik, A, Kot, J and Namieśnik, J. (2012) Sensitive determination of isoprostanes in exhaled breath condensate samples with use of liquid chromatography–tandem mass spectrometry. *Journal of Chromatography B* 893–894: 144–149. DOI:10.1016/j.jchromb.2012.03.005.
29. Sinha, D, Biswas, J and Bishayee, A. (2013) Nrf2-mediated redox signaling in arsenic carcinogenesis: A review. *Archives of Toxicology* 87: 383–396. DOI:10.1007/s00204-012-0920-5.

30. Zamuruyev, KO, Schmidt, AJ, Borras, E, McCartney, MM, Schivo, M, Kenyon, NJ, Delplanque, J-P and Davis, CE. (2018) Power-efficient self-cleaning hydrophilic condenser surface for portable exhaled breath condensate (EBC) metabolomic sampling. *Journal of Breath Research* 12: DOI:10.1088/1752-7163/aac5a5.
31. Willis, PA, Creamer, JS and Mora, MF. (2015) Implementation of microchip electrophoresis instrumentation for future spaceflight missions. *Analytical and Bioanalytical Chemistry* 407: 6939–6963. DOI:10.1007/s00216-015-8903-z.
32. Wulff, JE and Mitchell, MW. (2018) A Comparison of Various Normalization Methods for LC/MS Metabolomics Data. *Advances in Bioscience and Biotechnology* 09: 339–351. DOI:10.4236/abb.2018.98022.
33. Pearson, K. (1901) LIII. On lines and planes of closest fit to systems of points in space. *The London, Edinburgh, and Dublin Philosophical Magazine and Journal of Science* 2: 559–572. DOI:10.1080/14786440109462720.
34. Lee, LC, Liong, CY and Jemain, AA. (2018) Partial least squares-discriminant analysis (PLS-DA) for classification of high-dimensional (HD) data: A review of contemporary practice strategies and knowledge gaps. *Analyst* 143: 3526–3539. DOI:10.1039/c8an00599k.
35. Borish, L and Culp, JA. (2008) Asthma: A syndrome composed of heterogeneous diseases. *Annals of Allergy, Asthma and Immunology* 101: 1–9. DOI:10.1016/S1081-1206(10)60826-5.
36. Oldham, MJ and Moss, OR. (2019) Pores of Kohn: Forgotten alveolar structures and potential source of aerosols in exhaled breath. *Journal of Breath Research* 13: DOI:10.1088/1752-7163/ab0524.
37. Davis, MD. (Elsevier, 2020). Chapter 7 - Exhaled breath condensate and aerosol. in (eds. Beauchamp, J., Davis, C. & Pleil, J. B. T.-B. B. and the H. V. (Second E.) 109–119. DOI:https://doi.org/10.1016/B978-0-12-819967-1.00007-4.
38. Pleil, JD, Wallace, MAG and Madden, MC. (2018) Exhaled breath aerosol (EBA): The simplest non-invasive medium for public health and occupational exposure biomonitoring. *Journal of Breath Research* 12: 8–12. DOI:10.1088/1752-7163/aa9855.
39. Gould, O, Ratcliffe, N, Król, E and De Lacy Costello, B. (2020) Breath analysis for detection of viral infection, the current position of the field. *Journal of Breath Research* 14: DOI:10.1088/1752-7163/ab9c32.
40. Scheuch, G. (2020) Breathing Is Enough: For the Spread of Influenza Virus and SARS-CoV-2 by Breathing Only. *Journal of Aerosol Medicine and Pulmonary Drug Delivery* 33: 1–5. DOI:10.1089/jamp.2020.1616.
41. Stadnytskyi, V, Bax, CE, Bax, A and Anfinrud, P. (2020) The airborne lifetime of small speech droplets and their potential importance in SARS-CoV-2 transmission. *Proceedings of the National Academy of Sciences* 117: 11875–11877. DOI:10.1073/pnas.2006874117.
42. Pleil, JD, Beauchamp, JD, Risby, TH and Dweik, RA. (2020) The scientific rationale for the use of simple masks or improvised facial coverings to trap exhaled aerosols and possibly reduce the breathborne spread of COVID-19. *Journal of Breath Research* 14: 8–10. DOI:10.1088/1752-7163/ab8a55.
43. Duguid, JP. (1946) The size and the duration of air-carriage of respiratory droplets and droplet-nuclei. *Journal of Hygiene* 44: 471–479. DOI:10.1017/S0022172400019288.
44. Loudon, RG and Roberts, RM. (1967) Droplet Expulsion from the Respiratory TRACT. *American Review of Respiratory Disease* 95: 435–442. DOI:10.1164/arrd.1967.95.3.435.
45. Fairchild, CI and Stampfer, JF. (1987) Particle Concentration in Exhaled Breath. *American Industrial Hygiene Association Journal* 48: 948–949. DOI:10.1080/15298668791385868.
46. Papineni, RS and Rosenthal, FS. (2009) The Size Distribution of Droplets in the Exhaled

Breath of Healthy Human Subjects. *Journal of Aerosol Medicine* 10: 105–116. DOI:10.1089/jam.1997.10.105.
47. Holmgren, H, Ljungström, E, Almstrand, AC, Bake, B and Olin, AC. (2010) Size distribution of exhaled particles in the range from 0.01 to 2.0μm. *Journal of Aerosol Science* 41: 439–446. DOI:10.1016/j.jaerosci.2010.02.011.
48. Schwarz, K, Biller, H, Windt, H, Koch, W and Hohlfeld, JM. (2014) Characterization of Exhaled Particles from the Human Lungs in Airway Obstruction. *Journal of Aerosol Medicine and Pulmonary Drug Delivery* 28: 52–58. DOI:10.1089/jamp.2013.1104.
49. Tinglev, ÅD, Ullah, S, Ljungkvist, G, Viklund, E, Olin, AC and Beck, O. (2016) Characterization of exhaled breath particles collected by an electret filter technique. *Journal of Breath Research* 10: DOI:10.1088/1752-7155/10/2/026001.
50. Bake, B, Larsson, P, Ljungkvist, G, Ljungström, E and Olin, AC. (2019) Exhaled particles and small airways. *Respiratory Research* 20: 1–14. DOI:10.1186/s12931-019-0970-9.
51. Seferaj, S, Ullah, S, Tinglev, A, Carlsson, S, Winberg, J, Stambeck, P and Beck, O. (2018) Evaluation of a new simple collection device for sampling of microparticles in exhaled breath. *Journal of Breath Research* 12: DOI:10.1088/1752-7163/aaaf24.
52. Kietzmann, D, Kahl, R, Müller, M, Burchardi, H and Kettler, D. (1993) Hydrogen peroxide in expired breath condensate of patients with acute respiratory failure and with ARDS. *Intensive Care Medicine* 19: 78–81. DOI:10.1007/BF01708366.
53. EFFROS, RM, HOAGLAND, KW, BOSBOUS, M, CASTILLO, D, FOSS, B, DUNNING, M, GARE, M, LIN, W and SUN, F. (2002) Dilution of Respiratory Solutes in Exhaled Condensates. *American Journal of Respiratory and Critical Care Medicine* 165: 663–669. DOI:10.1164/ajrccm.165.5.2101018.
54. Lindh, WQ. (Delmar Cengage Learning, 2010). *Delmar's Comprehensive Medical Assisting: Administrative and clinical competencies*.
55. Boulpaep, EL. (2003). *Medical Physiology: A Cellular and Molecular Approach*.
56. Tang, JW, Nicolle, AD, Klettner, CA, Pantelic, J, Wang, L, Suhaimi, A Bin, Tan, AYL, Ong, GWX, Su, R, Sekhar, C, Cheong, DDW and Tham, KW. (2013) Airflow Dynamics of Human Jets: Sneezing and Breathing - Potential Sources of Infectious Aerosols. *PLoS ONE* 8: 1–7. DOI:10.1371/journal.pone.0059970.
57. Mhetre, MR and Abhyankar, HK. (2017) Human exhaled air energy harvesting with specific reference to PVDF film. *Engineering Science and Technology, an International Journal* 20: 332–339. DOI:10.1016/j.jestch.2016.06.012.
58. Elcner, J, Lizal, F, Jedelsky, J and Jicha, M. (2015) Study of airflow in the trachea of idealized model of human tracheobronchial airways during breathing cycle. *EPJ Web of Conferences* 92: DOI:10.1051/epjconf/20159202016.
59. Mols, G, Rohr, E, Benzing, A, Haberthur, C, Geiger, K and Guttmann, J. (2000) Breathing pattern associated with respiratory comfort during automatic tube compensation and pressure support ventilation in normal subjects. *Acta Anaesthesiologica Scandinavica* 44: 223–230. DOI:10.1034/j.1399-6576.2000.440302.x.
60. Wilm, M. (2011) Principles of Electrospray Ionization. *Molecular & Cellular Proteomics* 10: M111.009407. DOI:10.1074/mcp.m111.009407.
61. Cech, NB and Enke, CG. (2001) Practical implications of some recent studies in electrospray ionization fundamentals. *Mass Spectrometry Reviews* 20: 362–387. DOI:10.1002/mas.10008.
62. Hoffmann, P, Häusig, U, Schulze, P and Belder, D. (2007) Microfluidic glass chips with an integrated nanospray emitter for coupling to a mass spectrometer. *Angewandte Chemie - International Edition* 46: 4913–4916. DOI:10.1002/anie.200605152.
63. Mellors, JS, Gorbounov, V, Ramsey, RS and Ramsey, JM. (2008) Fully integrated glass microfluidic device for performing high-efficiency capillary electrophoresis and electrospray ionization mass spectrometry. *Analytical Chemistry* 80: 6881–6887.

DOI:10.1021/ac800428w.
64. Sainiemi, L, Sikanen, T and Kostiainen, R. (2012) Integration of fully microfabricated, three-dimensionally sharp electrospray ionization tips with microfluidic glass chips. *Analytical Chemistry* 84: 8973–8979. DOI:10.1021/ac301602b.
65. Fritzsche, S, Hoffmann, P and Belder, D. (2010) Chip electrophoresis with mass spectrometric detection in record speed. *Lab on a Chip* 10: 1227–1230. DOI:10.1039/c000349b.
66. Fritzsche, S, Ohla, S, Glaser, P, Giera, DS, Sickert, M, Schneider, C and Belder, D. (2011) Asymmetric organocatalysis and analysis on a single microfluidic nanospray chip. *Angewandte Chemie - International Edition* 50: 9467–9470. DOI:10.1002/anie.201102331.
67. Mellors, JS, Jorabchi, K, Smith, LM and Ramsey, JM. (2010) Integrated microfluidic device for automated single cell analysis using electrophoretic separation and electrospray ionization mass spectrometry. *Analytical Chemistry* 82: 967–973. DOI:10.1021/ac902218y.
68. Batz, NG, Mellors, JS, Alarie, JP and Ramsey, JM. (2014) Chemical vapor deposition of aminopropyl silanes in microfluidic channels for highly efficient microchip capillary electrophoresis-electrospray ionization-mass spectrometry. *Analytical Chemistry* 86: 3493–3500. DOI:10.1021/ac404106u.
69. Black, WA, Stocks, BB, Mellors, JS, Engen, JR and Ramsey, JM. (2015) Utilizing Microchip Capillary Electrophoresis Electrospray Ionization for Hydrogen Exchange Mass Spectrometry. *Analytical Chemistry* 87: 6286–6287. DOI:10.1021/acs.analchem.5b01179.
70. Redman, EA, Batz, NG, Mellors, JS and Ramsey, JM. (2015) Integrated microfluidic capillary electrophoresis-electrospray ionization devices with online ms detection for the separation and characterization of intact monoclonal antibody variants. *Analytical Chemistry* 87: 2264–2272. DOI:10.1021/ac503964j.
71. Chambers, AG, Mellors, JS, Henley, WH and Ramsey, JM. (2011) Monolithic integration of two-dimensional liquid chromatography-capillary electrophoresis and electrospray ionization on a microfluidic device. *Analytical Chemistry* 83: 842–849. DOI:10.1021/ac102437z.
72. Chambers, AG and Ramsey, JM. (2012) Microfluidic dual emitter electrospray ionization source for accurate mass measurements. *Analytical Chemistry* 84: 1446–1451. DOI:10.1021/ac202603s.
73. Sikanen, T, Tuomikoski, S, Ketola, RA, Kostiainen, R, Franssila, S and Kotiaho, T. (2007) Fully microfabricated and integrated SU-8-based capillary electrophoresis-electrospray ionization microchips for mass spectrometry. *Analytical Chemistry* 79: 9135–9144. DOI:10.1021/ac071531+.
74. Nordman, N, Sikanen, T, Aura, S, Tuomikoski, S, Vuorensola, K, Kotiaho, T, Franssila, S and Kostiainen, R. (2010) Feasibility of SU-8-based capillary electrophoresis-electrospray ionization mass spectrometry microfluidic chips for the analysis of human cell lysates. *Electrophoresis* 31: 3745–3753. DOI:10.1002/elps.201000373.
75. Li, FA, Huang, JL and Her, GR. (2008) Chip-CE/MS using a flat low-sheath-flow interface. *Electrophoresis* 29: 4938–4943. DOI:10.1002/elps.200800271.
76. Sikanen, T, Aura, S, Franssila, S, Kotiaho, T and Kostiainen, R. (2012) Microchip capillary electrophoresis-electrospray ionization-mass spectrometry of intact proteins using uncoated Ormocomp microchips. *Analytica Chimica Acta* 711: 69–76. DOI:10.1016/j.aca.2011.10.059.
77. Yin, H, Killeen, K, Brennen, R, Sobek, D, Werlich, M and Van De Goor, T. (2005) Microfluidic chip for peptide analysis with an integrated HPLC column, sample enrichment column, and nanoelectrospray tip. *Analytical Chemistry* 77: 527–533. DOI:10.1021/ac049068d.

78. Tähkä, SM, Bonabi, A, Jokinen, VP and Sikanen, TM. (2017) Aqueous and non-aqueous microchip electrophoresis with on-chip electrospray ionization mass spectrometry on replica-molded thiol-ene microfluidic devices. *Journal of Chromatography A* 1496: 150–156. DOI:10.1016/j.chroma.2017.03.018.
79. Lu, N, Petersen, NJ, Kretschmann, AC and Kutter, JP. (2021) Non-aqueous electrophoresis integrated with electrospray ionization mass spectrometry on a thiol-ene polymer–based microchip device. *Analytical and Bioanalytical Chemistry* DOI:10.1007/s00216-021-03374-9.
80. Sun, X, Kelly, RT, Tang, K and Smith, RD. (2010) Ultrasensitive nanoelectrospray ionization-mass spectrometry using poly(dimethylsiloxane) microchips with monolithically integrated emitters. *The Analyst* 135: 2296. DOI:10.1039/c0an00253d.
81. Geczy, R, Sticker, D, Bovet, N, Häfeli, UO and Kutter, JP. (2019) Chloroform compatible, thiol-ene based replica molded micro chemical devices as an alternative to glass microfluidic chips. *Lab on a Chip* 19: 798–806. DOI:10.1039/c8lc01260a.
82. Boden, S, Karam, P, Schmidt, A and Pennathur, S. (2017) A process to fabricate fused silica nanofluidic devices with embedded electrodes using an optimized room temperature bonding technique. *Applied Physics Letters* 110: DOI:10.1063/1.4982968.
83. Cassidy, J, Khoo, SB, Pons, S and Fleischmann, M. (1985) Electrochemistry at very high potentials: The use of ultramicroelectrodes in the anodic oxidation of short-chain alkanes. *Journal of Physical Chemistry* 89: 3933–3935. DOI:10.1021/j100264a034.
84. Zrodnikov, Y, Rajapakse, MY, Peirano, DJ, Aksenov, AA, Kenyon, NJ and Davis, CE. (2019) High Asymmetric Longitudinal Field Ion Mobility Spectrometry Device for Low Power Mobile Chemical Separation and Detection. *Analytical Chemistry* 91: 5523–5529. DOI:10.1021/acs.analchem.8b05577.
85. Fung, S, Levasseur, MK, Rajapakse, MY, Chew, BS, Fung, AG, Mccartney, MM, Kenyon, NJ and Davis, E. (2022) Sensors and Actuators : A . Physical Battery powered dual-polarity ion detector for trace chemical sensing. *Sensors and Actuators: A. Physical* 338: 113442. DOI:10.1016/j.sna.2022.113442.
86. Davis, CE, Frank, M, Mizaikoff, B and Oser, H. (2010) Editorial The Future of Sensors and Instrumentation for Human Breath Analysis. *IEEE Sensors Journal* 10: 3–6. DOI:10.1109/JSEN.2009.2035675.